

**STUDY ON THE PREPARATION OF NANO-TiB₂ REINFORCED AL
MATRIX COMPOSITES**

by
Yanfei Liu

A Dissertation

*Submitted to the Faculty of Purdue University
In Partial Fulfillment of the Requirements for the degree of*

Doctor of Philosophy



Department of Technology
West Lafayette, Indiana
December 2018

THE PURDUE UNIVERSITY GRADUATE SCHOOL
STATEMENT OF COMMITTEE APPROVAL

Dr. Xiaoming Wang

School of Engineering Technology

Dr. Milan Rakita

School of Engineering Technology

Dr. Haiyan Zhang

School of Engineering Technology

Dr. Joshua Huang

Ryobi Die Casting

Approved by:

Dr. Kathryn A. Newton.

Head of the Graduate Program

TO MY BELOVED GRANDFATHER

Mr. Hanqi Hu

ACKNOWLEDGMENTS

First and foremost, I would like to show my deepest gratitude to my supervisor, Dr. Qingyou Han, who has provided me with a valuable opportunity while studying at Purdue University and walk me through all the stages of my research. I do appreciate his patience, encouragement, and professional instructions during my dissertation writing. The four years as a student of Dr. Han is the most precious time in my life.

Secondly, I am grateful to my committee members, Dr. Xiaoming Wang, Dr. Haiyan Zhang, Dr. Joshua Huang, and Dr. Millan Rakita. Their selfless guidance, assistance, comments and criticism pushing me ahead, without their support, the completion of this dissertation would not have been possible.

I want to thank all the graduate students who have helped me during my studies and experiment. This friendship will be with me for life.

I should finally like to express my gratitude to my beloved parents who have always been helping me out of difficulties and supporting without a word of complaint. Also my thanks would go to my wife, Ms. Tengfei Shui and my daughter Muran Liu. Their love and support is the driving force and motivation for my doctoral study in the USA.

TABLE OF CONTENTS

LIST OF TABLES	8
LIST OF FIGURES	9
ABSTRACT	11
CHAPTER 1. INTRODUCTION	1
1.1 Introduction	1
CHAPTER 2. REVIEW OF LITERATURE	6
2.1 Outline	6
2.2 Review of TiB ₂ Particulates Synthesized in Molten Al	6
2.2.1 Characteristics of TiB ₂	6
2.2.2 Synthesis of TiB ₂ /Al-MMCs	7
2.3 Fabrication Route	8
2.3.1 Typical In-situ Method of Fabricating Al-MMCs	8
2.3.1.1 Self-Propagating High Temperature Synthesis (SHS)	9
2.3.1.2 Reaction Mechanical Alloying (RMA)	11
2.3.1.3 Reaction Hot Pressing (RHP)	13
2.3.1.4 Combustion Assisted Casting (CAC)	14
2.3.1.5 Contact Reaction Process (CRP)	15
2.3.1.6 Mixed Salt Reaction (MSR)	16
2.3.1.7 Direct Melt Reaction (DMR)	18
2.3.1.8 Direct Metal Oxidation (DIMOX TM)	19
2.3.1.9 Vapor Liquid Synthesis (VLS)	20
2.3.2 Typical Ex-situ Method of Fabricating Al-MMCs	22
2.3.2.1 Powder Metallurgy Method	23
2.3.2.2 High Energy Ball Milling Method	24
2.3.2.3 Stirring Techniques	25
2.3.3 High-Intensity Ultrasound in Liquids	26
2.3.4 Application of High-intensity Ultrasound in Particulate Reinforced Al-MMCs	29
2.4 Effect of Particulate Size on the Preparation of Al-MMCs	30
2.5 Nano particulate Reinforced Metal Matrix Composite	31

2.6	Particle Pushing	33
2.7	Surface Energy Models	35
2.8	Limitations of Surface Energy Model	39
CHAPTER 3. RESEARCH METHODOLOGY		40
3.1	Outline	40
3.2	MSR for Synthesizing Al-4.5wt.%Cu Composite	40
3.2.1	Raw Materials and Preparation	40
3.2.1.1	Preparation of TiB_2/Al -4.5wt.%Cu Alloy	42
3.2.1.2	Preparation of $\text{Al}_3\text{Ti}/\text{Al}$ -4.5wt.%Cu Alloy	42
3.2.2	Samples Analysis	43
3.2.2.1	Grinding and Polishing Processes	43
3.2.2.2	Microstructure Analysis	43
3.3	Fabrication of Stirring Process of TiB_2/Al with the Assistance of Ultrasound Vibration	44
3.3.1	Raw Materials and Experimental Process	44
3.3.2	Forging	45
3.3.3	Sample Analysis	47
3.3.3.1	Grinding and Polishing Process	47
3.3.3.2	Tensile Strength Test	47
3.3.3.3	Hardness Test	48
3.3.3.4	Microstructure Analysis	49
CHAPTER 4. RESULTS		50
4.1	Outline	50
4.2	Evaluation Experiment	51
4.2.1	Wedge-shaped Casting	51
4.2.2	$\text{TiB}_2/\text{Al}_3\text{Ti}$ Particles	52
4.2.3	Al-4.5wt.%Cu Alloy	53
4.2.4	TiB_2/Al -4.5wt.%Cu Alloy	55
4.2.5	$\text{Al}_3\text{Ti}/\text{Al}$ -4.5wt.%Cu alloy	56
4.2.6	Analysis and Calculation	58
4.3	Results of MSR Experiment	62
4.3.1	Particle Pushing Analysis	62

4.3.2	Diffusion Convection Model	64
4.3.3	TiB ₂ /Al-4.5wt.% Cu-MMCs in Diffusion Convection Model	67
4.3.4	Temperature Gradients Effect.....	74
4.4	Results of Stirring Experiment.....	77
4.4.1	Influence of High Energy Ball Milling on Nano-TiB ₂ Particles.....	77
4.4.2	Original Sample Morphology Analysis	79
4.4.3	Forging Treatment Analysis	82
4.4.4	Hardness Test.....	83
4.4.5	Tensile Strength Test	84
4.4.6	Elongation test	85
CHAPTER 5. SUMMARY, CONCLUSIONS, AND RECOMMENDATIONS.....		87
5.1	Main Conclusions	87
5.2	Outlook	89
REFERENCES		91

LIST OF TABLES

Table 2.1 The Advantages and Disadvantages of DIMOX™ Process	20
Table 3.1 Chemical Composition of Al-4.5wt% Cu.....	41
Table 3.2 Particulate & Matrix of the Wedge Castings	43
Table 3.3 Main Parameters of Continuous Forging Equipment	45
Table 3.4 Continuous Forging Process Parameters	46
Table 3.5 Samples Fabricated Under Different Experimental Parameters	46
Table 4.1 Coupon Used in the Research.....	52
Table 4.2 SDAS of Al-4.5wt.% Cu.....	55
Table 4.3 Physical Properties of Al-4.5wt.%Cu Alloy and Calculation Parameters.....	59
Table 4.4 Average Growth Rate in Al-4.5wt.%Cu with Different Cooling Conditions.....	59
Table 4.5 Physical Properties of Al-4.5wt.%Cu Alloy	61
Table 4.6 Critical Growth Rates for Particles of Different Sizes	62
Table 4.7 Parameters Required in the Calculation.....	67
Table 4.8 Critical Velocity Corresponding to Particle Size.....	72
Table 4.9 Critical Velocity Corresponding to Different Temperature Gradient ($\theta = \pi/2$).....	75
Table 4.10 Critical Velocity Corresponding to Different Temperature Gradient ($\theta \rightarrow 0$).....	76
Table 4.11 Average Vickers Hardness of TiB ₂ /Al composites prepared in varies parameters. ...	84
Table 4.12 Average Tensile strength of TiB ₂ /Al Composites	84
Table 4.13 Average elongation of TiB ₂ /Al composites prepared using various parameters	85

LIST OF FIGURES

Figure 1.1 Classification of the Reinforcement Types of Al-MMCs.	2
Figure 2.1 Crystal Structure of TiB_2	7
Figure 2.2 Classification of Preparation Methods of In-situ Al-MMCs.	9
Figure 2.3 Schematic Diagram of Process of SHS	10
Figure 2.4 Process of RMA Method.	12
Figure 2.5 Process of RHP Method.	13
Figure 2.6 Process of CAC Method.....	14
Figure 2.7 The Process of Preparing Composite Materials by CRP Method.	15
Figure 2.8 Schematic of Process of MSR Method.....	16
Figure 2.9 Process of Fabrication of MMCs by DIMOX™	20
Figure 2.10 Schematic of Fabrication of In-situ PRMMCs Using VLS.....	21
Figure 2.11 Classification of Ex-situ Al-MMC Preparation Processes.	23
Figure 2.12 Process Flow Schematic of Powder Metallurgy Method.	23
Figure 2.13 Stir Casting Technique for Fabrication MMCs.	25
Figure 2.14 Schematic Diagram of Acoustic Streaming	28
Figure 2.15 Microstructure of (a) 20% SiC/Al and (b) 50% SiC/Al Composites.	31
Figure 2.16 Particle Concentration in Solid–liquid System (Han, & Hunt, 1995).	34
Figure 2.17 Variation of Interface Energy.	36
Figure 3.1 Sketch of Mechanical Stirring Process.....	41
Figure 3.2 Schematic Diagram of Ultrasonic Vibration Assisted Method.	45
Figure 3.3 Schematic Diagram of Tensile Strength Sample and Sampling Method.	48
Figure 4.1 Sketch of a Wedge-shaped Casting Used in Experiment.	51
Figure 4.2 Diagram for Analysis of Nucleation Process	52
Figure 4.3 SEM Image of Al-4.5wt.%Cu Alloy	54
Figure 4.4 Distribution Condition of TiB_2 /Al-4.5wt.%Cu Alloy of A-3.....	56
Figure 4.5 TiB_2 Particle Diameter Distribution in TiB_2 /Al-4.5wt.%Cu Coupon	56
Figure 4.6 Particle Distribution in the Al_3Ti /Al-4.5wt.%Cu Alloy	57
Figure 4.7 Particle Diameter Distribution in Al_3Ti /Al-4.5wt.%Cu Alloy	57
Figure 4.8 Morphology of Al-4.5wt.%Cu Alloy at Various Cooling Rates	58

Figure 4.9 Morphology of TiB_2/Al -4.5wt.%Cu Alloy at Various Cooling Rates	60
Figure 4.10 Morphology of $\text{Al}_3\text{Ti}/\text{Al}$ -4.5wt.%Cu Alloy at Various Cooling Rates	61
Figure 4.11 Critical Velocity versus Particle Diameter	63
Figure 4.12 Equilibrium Between the Particle and Solids	64
Figure 4.13 Sketch Diagram of Particle Pushing Process.....	65
Figure 4.14 Schematic Illustration of Engulfment.....	67
Figure 4.15 Schematic of Contact Area between Freezing Front and Particle.....	69
Figure 4.16 Three Possible State Between Particle and the Interface	71
Figure 4.17 Critical Velocity versus Particle Diameter	73
Figure 4.18 Critical Velocity Prediction Comparison	74
Figure 4.19 Critical Velocity versus Temperature Gradient ($\theta = \pi/2$).....	75
Figure 4.20 Critical Velocity versus Temperature Gradient ($\theta \rightarrow 0$).....	76
Figure 4.21 Comparison Diagram.....	78
Figure 4.22 Comparison Diagram.....	79
Figure 4.23 Microstructure of O-5 Sample.....	80
Figure 4.24 SEM Images of O-5 Sample.....	81
Figure 4.25 EDS Patterns of the Reinforcements in Original Sample.....	82
Figure 4.26 Metallographic Microstructure of Nano-5%.wt TiB_2/Al Composites.....	83

ABSTRACT

Author: Liu, Yanfei. PhD

Institution: Purdue University

Degree Received: December 2018

Title: Study on the Preparation of Nano-TiB₂ Reinforced Al Matrix Composites.

Committee Chair: Xiaoming Wang

TiB₂ particulate reinforced aluminum matrix composites (TiB₂/Al-MMCs) have received extensive attention due to a great potential in a wide variety of applications. Nano-TiB₂/Al-MMCs have also received attention from scholars with the development of nanotechnology in recent years. However, obstacles like agglomeration of nanoparticles in the matrix, and the difficulty of preparation of nanoparticulate reinforced metal matrix composites (PRMMNCs) still need to be resolved. This study summarizes the research progress of Al-matrix composites (Al-MMCs) in recent years and exemplifies the common preparation methods. Experiments were designed to study the common problems in the preparation of composite materials.

Two experiments were designed and completed in this study. First, TiB₂/Al-4.5Cu composites were synthesized through a mixed salt reaction method. The distribution of reinforcing particle in the aluminum matrix was observed. The predictive model of particle behavior in Al-4.5wt. %Cu matrix based on thermodynamic laws was re-examined. The experiment results are inconsistent with the prediction from a classic prediction model. Regardless of the rate of solidification and critical velocity (V_C), the most of the particles are rejected by advancing solid-liquid interface. Through review of classic particle pushing theory, this study attempts to derive a new boundary condition used to predict the behavior of reinforcing particles in a metal matrix during solidification based on the diffusion convection equations.

Second, nano-TiB₂/Al composites with a variety of volume fractions were synthesized by ultrasound assistance in a stirring method. The research has focused on optimization and improvement of preparation methods. High-energy ball milling (HEBM) and high-intensity ultrasound (HIU) were introduced into the fabrication process. Furthermore, a forging post-treatment process is used to process as-cast samples prepared by the experiment, so that the reinforcing particles in the composite material can be redistributed. The experiment results show that HEBM facilitates the mixing of nano-TiB₂ particles with salts. HIU helps distribute particles evenly throughout the matrix. The Vickers hardness and tensile strength of the composites were tested. The results indicated that the forging treatment has great influence on the mechanical properties of composite materials.

CHAPTER 1. INTRODUCTION

1.1 Introduction

The design concept of composite materials stems from combining two or more different types of materials together by physical or chemical methods to synthesis a new type of material. The research history of composite materials can be traced back to the building materials of houses. With the development of technology, modern composites can be prepared by combining different materials to reach the desired overall performance. Usually, Composite materials consist of a matrix, reinforcement, and the interface (Shah, 2016). Their properties are affected by the type of the original materials and the structure of composite materials. For example, ceramic/metal composites prepared from ceramics and metals, which retain the main properties of the matrix materials, and obtain new properties through the composite effect. In general, the matrix used for composite materials is mainly polymers, metals, and ceramics. Therefore, composites are classified into polymer-based, metal-based, and ceramic-based that depending on the type of matrix. This article mainly discusses the current status of Al-matrix nanocomposites (Guo, Q, & Ghadiri, R, 2014; He, F, & Han, Q, 2008).

Among the modern composite materials, the development of Al-matrix composite materials is the most mature and their applications are also the most extensive. Typically, aluminum or aluminum alloys are used in combination with a high performance second phase to make new composite materials. Basically, the desirable mechanical properties such as excellent fatigue and wear resistance, fracture toughness, shear and compression deformation strength, high stability, and thermal conductivity can be achieved depending on the properties of the reinforcements and the fabrication method of MMCs. (Ibrahim, Mohamed, & Lavernia, 1991). Therefore Al-MMCs show great application potential and are easy to promote in many areas such as aviation, aerospace, and manufacturing. In the 1980's, Lockheed Martin used SiC particle reinforced (15% ~ 20%) Al-matrix composites as non-primary load-bearing structural material for airborne electronic equipment. At the end of the 1990's, composite materials were officially applied on large passenger aircraft. SiC/Al-MMCs were used as a material for guide vanes in engine exhausts on Boeing 777 aircraft. Hewlett-Packard Company's research and development results

show that Al-MMCs have better impact resistance than resin-based composites, and that any damage on the part is more visible (Casati, & Vedani, 2014).

Today, a variety of materials have been used as reinforcing phases for the preparation of aluminum matrix composites. Depending on the characteristics of these reinforcing materials, Al-MMCs mainly divided into two major categories (Shah, 2016): continuous and non-continuous reinforced composites, as shown in Figure 1.1. Among them, Al-MMCs in the discontinuous composite material have the advantages of low manufacturing cost, simple production process, and material isotropy. Often the particle-reinforced material can be made using the casting process, making it one of the most promising varieties in the composite field (Koczak, & Premkumar, 1993).

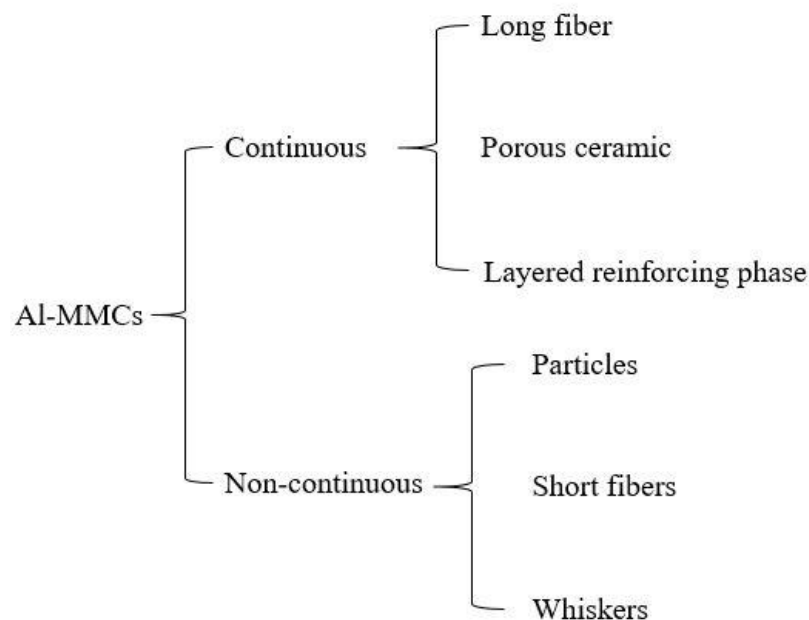


Figure 1.1 Classification of the Reinforcement Types of Al-MMCs.

According to the manufacturing processes, Al-MMCs are generally classified into ex-situ method and in-situ method (Gao, Wu, Lü, Xiong, Du, & An, 2017). The ex-situ method refers to a method of preparing a composite material by adding reinforcing particles to a molten aluminum melt. The advantages of the ex-situ method is that the preparation process is highly controllable and does not easily generate impurities. However, the ex-situ preparation has poor

compatibility due to poor wettability between matrix and reinforcing. For the in-situ method, the reinforcing phase is formed directly from the matrix by a chemical reaction during the fabrication process, resulting in better compatibility between the reinforcing phase and the matrix (Reddy, Das, & Das, 2007).

The advantages of metallic materials are that their melts can be cast to produce complex castings. For example, by using a mechanical stirring method with custom mold, the complex shaped MMCs product can be cast. Besides, Metal-based composite materials facilitate secondary processing, which make it has wide applicability and flexible application. Furthermore, the preparation process directly determines the production cost of the composite material, and careful selection of preparation methods is important for large-scale production.

Among the many composite materials, particulate reinforced metal matrix composites (PRMMCs) have many advantages. Although their mechanical properties are difficult to compete with fiber-reinforced composite materials, they are significantly lower in cost, have a simpler fabrication process with flexible preparation methods, and are convenient for secondary processing, suiting mass production.

The size of the reinforcing particle has always been an important parameter for the performance of the PRMMCs. With the advancement of nanotechnology, the scale of the reinforcing particle of the composites has changed from microns to nanometers. It has been reported that compared to micron particulate reinforced composites, PRMMNCs have better mechanical properties and machinability. Until now, however, as a promising composite, the research on the preparation of PRMMNCs is still limited. Many problems encountered during the preparation process have yet to be resolved. For example, uneven particle distribution, agglomeration of nanoparticles in a matrix, and the excessive production cost of nanocomposites are all issues that need to be remedied (Tjong, & Ma, 2000).

Generally, the agglomeration phenomenon of nanoparticles is considered to be difficult to avoid due to the large specific surface area (SSA) of nanoparticles. If the agglomeration is significant, the toughness and plasticity of the composite are reduced and the cracks are easily formed on the

surface of the composite (Hemanth, 2009; He, Han, Q., & Jackson, 2008; Yi, Du, & Zhang, 2017).

In general, the solidification process in the preparation of MMCs determines the distribution of the reinforcing particles in the matrix. During solidification, when particles in the liquid phase encounter a growing solid-liquid interface, the particles can theoretically be rejected by the freezing front or trapped in, which macroscopically determines the particle distribution in the matrix. Therefore, the mechanism of the reinforcing particles behaviors during solidification are main research direction.

A water-ice system experiment is developed by Uhlmann *et al.* (1964), which can examine the distribution of tiny particles in liquids. A predictive model of particle behavior based on the surface free energy is established to study whether particulates in liquid are trapped or rejected by growing front. This model has been studied by scholars and improved over times and has been used as a classic method to predict particle behavior during solidification. However, reports indicate that in the practical solidification process, the distribution conditions of nano or micro particles in metal matrix in experiments that performed by some scholars is inconsistent with the predictions come from the surface free energy models (Han, & Hunt, 1995; Wang, & Han, 2014). This study examined the classic prediction model by designing the $\text{TiB}_2/\text{Al-4.5Cu}$ -MMCs preparation experiment to better understand the behavior mechanism of particulate during solidification.

Compared with other preparation methods, the ex-situ stirring method for preparing Al-MMCs is suitable for nanoparticle reinforcement and cost effective. In this study, HEBM and HIU assisted technology and forging treatment were introduced systematically to optimize the particle distribution in the matrix in the early, middle, and late stages of the preparation process (Liu, Li, & Chen, 2013).

This study aims to systematically summarize and review the preparation methods of Al-MMCs and the redistribution of the particles in the solidification process of solution. $\text{TiB}_2/\text{Al-4.5Cu}$ -MMCs and TiB_2/Al -MMCs were prepared by using a mixed salt reaction method to study the

behavior of reinforcing particles in the matrix and optimize the preparation of PRMMNCs. Two experiments with their own practical research purpose were designed:

Experiment one is a verification experiment aimed at verifying and improving the classic prediction model by examining the distribution condition of $\text{TiB}_2/\text{Al}_3\text{Ti}$ particles in Al-4.5Cu matrix;

Experiment two fabricated TiB_2/Al -MMCs with different volume fraction of reinforcements by using stirring method with HIU technique assistance, HEBM technique was introduced to help mix powder as well. Besides, the as-cast sample is subjected to forging treatment to study the effect of post-treatment on particle distribution in the matrix. The purpose of experiment is to improve the distribution of nano- TiB_2 particles in Al matrix.

CHAPTER 2. REVIEW OF LITERATURE

2.1 Outline

According to the research focuses of this dissertation, three main topics are covered in this chapter. First is an overview of the basics of TiB_2/Al composites, such as the characteristics of the TiB_2 phase as a reinforcement in the Al matrix and the methods (in-situ and ex-situ) for the synthesis of TiB_2 particles in molten Al. This section also covers the preparation of Al-MMCs by MSR and mechanical stirring. In the preparation of TiB_2/Al -MMCs, the problem of particle agglomeration caused by the nanometer size is of primary focus. Second, the knowledge of HIU technology is introduced. In the final section, the particle pushing theory is systematically introduced and discussed, including the origin of the theory, current problems, and the role of particle pushing in the preparation of composite materials. The discussion of the mechanism of particle pushing also examines the behavior of reinforcing particles in the solidification process.

2.2 Review of TiB_2 Particulates Synthesized in Molten Al

2.2.1 Characteristics of TiB_2

TiB_2 is an anisotropic polycrystalline material that has been broadly studied in many areas of material science in recent years due to its high modulus, high erosion resistance, excellent refractory properties, and chemical inertness. TiB_2 has an Hexagonal Close Packed Crystal (HCP) structure with lattice parameters of $a=3.03034$, $c=3.22953$, and $c/a=1.066$, meaning TiB_2 is much more stable and refractory than TiB , while the latter is a stable compound in equilibrium only with a titanium-rich alloy. The crystal structure is illustrated in Figure 2.1 (Spoor, Maynard, Pan, Green, Hellmann, & Tanaka, 1997).

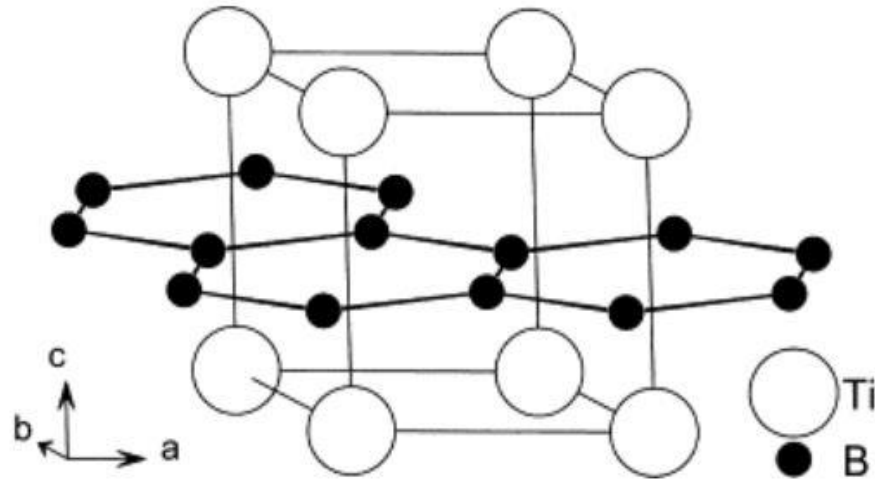


Figure 2.1 Crystal Structure of TiB_2

Due to its unique characteristics, scholars generally consider TiB_2 an ideal reinforcement material. It has received increased attention as a reinforcing particle for composite materials. The chemical properties of TiB_2 are stable, which means it is unlikely to react with an Al solution even at a high temperature, and the low production cost is also an important advantage, laying a foundation for the large-scale production of TiB_2 -reinforced MMCs in the future (Anandkumar, Almeida, & Vilar, 2011).

2.2.2 Synthesis of TiB_2/Al -MMCs

There are currently various methods for synthesizing TiB_2/Al -MMCs. They are roughly divided into two categories, in-situ and ex-situ methods, according to the method of adding the reinforcing particles.

For TiB_2/Al -MMCs, the in-situ method generally refers to the chemical reaction of TiB_2 particles in an Al solution. In contrast, the ex-situ method involves preparing the composite directly by adding pre-formed TiB_2 particles. Typically, Al-MMC is primarily prepared by metallurgy, thermal spraying, casting and preform casting. However, traditional methods of preparation face many insurmountable deficiencies. For example, the wettability between the ceramic particles and the matrix is poor, and the matrix easily reacts with the particles to form an intermediate

product with in-situ preparation method, thereby affecting the strength of the material. High production costs are also an urgent problem to be solved (Wang, Li, Chen, & Xue, 2012).

From a technical and economic point of view, new manufacturing processes have been developed that are superior to conventional manufacturing processes. Some of these techniques have been widely used, such as exothermic dispersion, directional melting, self-propagating high temperature synthesis (SHS), vapor-liquid-solids and reactive mechanical alloying (RMA). Lakshmi *et al.* (1998) applied an exothermic reaction process fabricated TiB_2/Al -MMCs by using mixed salt which can enhance the wettability of ceramic particles. The mixed salt including K_2TiF_6 and KBF_4 , during fabrication process, the Ti and B element transferred from the salts to form TiB_2 in molten Al, resulting desired composite. Mechanical stirring technology is an important method for preparing Al-MMCs which classified in ex-situ method. It has lot of advantages such as simple process, low cost and convenient for customization however, it is easy to produce impure inclusions due to chemical reaction during stirring, Thus the mechanical properties of the composite are impaired. Basically, ex-situ method is more used for ceramic particles which are chemically stable and are not easily reacted at high temperatures. (Akbari, Baharvandi, & Shirvanimoghaddam, 2015).

With the continuation of the research, the preparation of nano- TiB_2/Al -MMCs has gradually attracted the attention of scholars. The ex-situ method is a common method for preparing nanoparticle-reinforced metal matrix composite materials (PRMMNCs), because the method can directly use prefabricated nano-sized particles. However, the problems of the agglomeration of the particles and the dispersion of the reinforcements in the molten Al melt remain to be resolved, which will be discussed later (Abbasipour, Niroumand, & Vaghefi, 2010).

2.3 Fabrication Route

2.3.1 Typical In-situ Method of Fabricating Al-MMCs

For decades, materials scientists have explored a variety of preparation processes in order to prepare Al-MMCs with better properties and microstructures. In-situ preparation methods can be roughly classified into four types according to the reaction process at the time of preparation:

solid–liquid reaction, vapor–liquid–solid reaction, solid–solid reaction, and liquid–liquid reaction. According to the molding process of composite materials, Liu *et al.* (2012) roughly divided the in-situ preparation methods of Al-MMCs into two types, unstirred cast synthesis process and stirred cast synthesis process, shown in Figure 2.2.

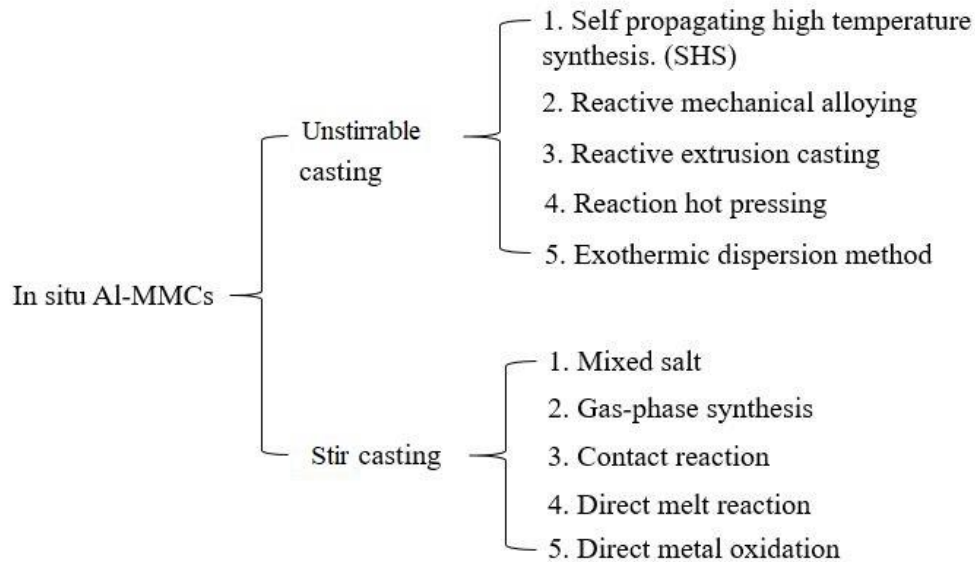


Figure 2.2 Classification of Preparation Methods of In-situ Al-MMCs.

2.3.1.1 Self-Propagating High Temperature Synthesis (SHS)

SHS is a typical process to synthesize ceramics or intermetallic materials. It is based on the use of a highly exothermic reaction to form a composite. It is the most popular method classified as an unstirred cast synthesis process. SHS was proposed by scientists of the former Soviet Union, Merzhanov *et al.* (1990), while studying the sintering of Ti and B mixed powders. The SHS method, based on the basic principle of an exothermic chemical reaction, utilizes external energy to induce a localized chemical reaction in a highly exothermic system to form a chemical reaction product. When the combustion wave propagates through the entire body, the desired material is synthesized. A schematic diagram of a SHS reaction process is illustrated in Figure 2.3 (Merzhanov, 1995; Cui, Shen, Meng, & Kang, 2000).

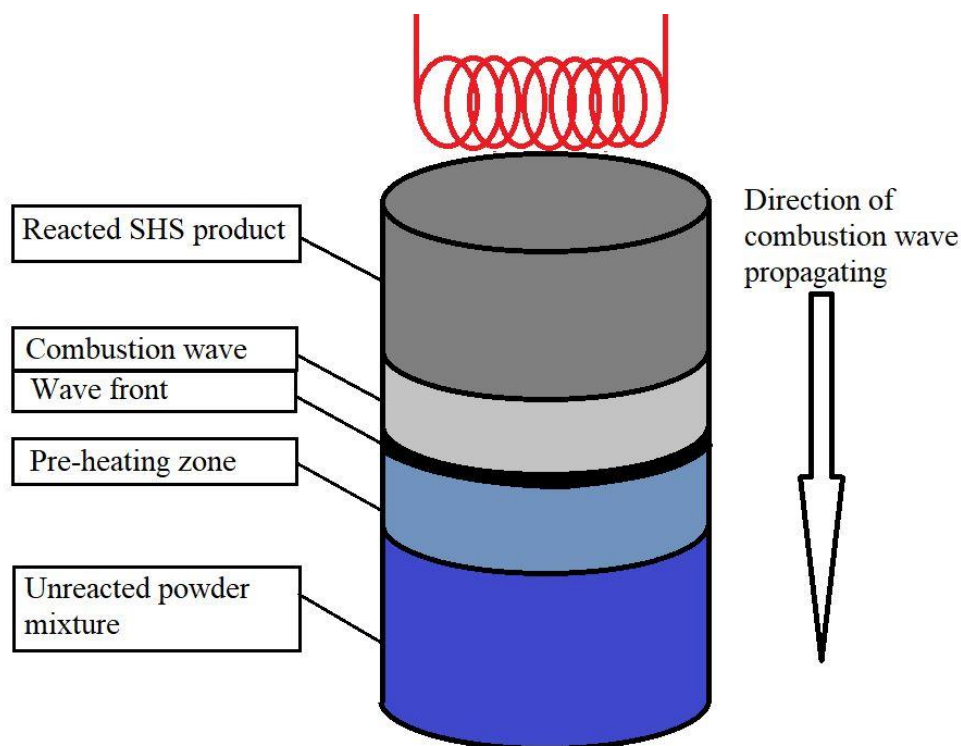


Figure 2.3 Schematic Diagram of Process of SHS

The self-sustaining reaction combustion wave during the reaction is the most important feature of the SHS method. Three conditions must be met to achieve this self-driven reaction combustion wave. First, the chemical reaction between the reaction components must be highly exothermic. Second, a portion of the reactants should form a liquid or gas during the reaction so that the reactants can continue to diffuse forward and allow the reaction to proceed. Third, the heat loss in the reaction needs to be less than the increase in the exothermic portion of the reaction (Tjong & Ma, 2000). In addition to the above, the particle size of the original ancestor, preheating temperature, and preheating rate can also affect the self-propagation process.

The main advantages of the SHS process are the efficient utilization of the reaction energy and the high speed of synthesis and purification due to the volatilization of impurities. For several decades, the SHS method has made considerable progress in the preparation of composite material, mainly reflected in the following aspects. 1) The SHS method was combined with an applied electric field to form a “SHS-outfield” process, which utilized an applied electric field to enhance the SHS process to achieve a reaction that was difficult to perform under normal

conditions (Hu, Luo, & Yan, 2007). 2) The SHS method was combined with conventional pressure processing methods (e.g., extrusion, rolling, stamping) to form the “SHS-pressure processing” process, enabling simultaneous material synthesis and densification (Horvitz & Gotman, 2002). 3) Porous materials were prepared by the SHS method (Yeh & Wang, 2009). 4) Ceramic matrix composites were prepared by the SHS method (Zhang & Wang, 2008). 5) Intermetallic matrix composite material was prepared by the SHS method (Mishra, Das, & Sherbacov, 2007). Nevertheless, it remains difficult to prepare PRMMCs using the SHS method, because the metal matrix powder usually acts as a diluent, causing the combustion wave to be extinguished and the reaction to be prevented. Therefore, SHS is more suitable for systems with large amounts of heat release.

The use of the SHS method to prepare particle-reinforced Al-MMCs has some disadvantages. The resulting product has high porosity and low density. It is also difficult to prepare Al-MMCs with a lower mass fraction. Although a highly exothermic reaction can effectively reduce the porosity of the product, the ideal high heat release system is difficult to find. For these reasons, the development of Al-MMCs prepared by the SHS method is slow, and the authors believe that this is not the most suitable method for preparing Al-MMC materials.

2.3.1.2 Reaction Mechanical Alloying (RMA)

The RMA method generally uses a HEBM to treat the mixed reaction powder. In the ball milling process, the reactive powder induces a chemical reaction to form a composite powder, which is subjected to secondary treatment and then made into the desired composite material. The RMA method is shown in Figure 2.4 (Suryanarayana, 2001).

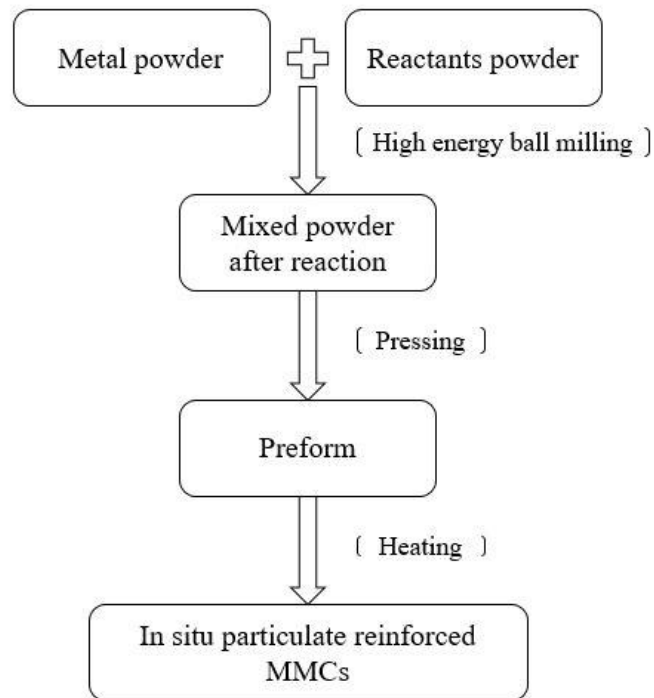


Figure 2.4 Process of RMA Method.

Today, the RMA process is widely used to prepare intermetallic compounds and nanocrystal-line materials. In the RMA process, reinforcing particles can be uniformly dispersed in a metal matrix powder by ball milling treatment. The MMCs prepared by the RMA method have three advantages. First, a solid solution is formed during the powder alloying process, which generates dispersed metal compound particles in the subsequent thermal processing. Second, the powder system has high energy storage, which helps to reduce the temperature at which the MMCs are densified. Third, the reinforcing particles produced by the RMA method are clean, small, and evenly dispersed.

The RMA method for preparing MMCs also has disadvantages. Since the RMA can only be directly made into a powder material, the resulting composite powder needs to be subjected to secondary processing, and the production process is complicated. In addition, the ball milling process duration is long and the efficiency is low, which increases the preparation cost, and therefore, the RMA method is unsuitable for mass production.

2.3.1.3 Reaction Hot Pressing (RHP)

The process of the RHP method involves uniformly mixing the metal matrix powder with the reinforcing powder, forming the billet by cold pressing, and finally forming the in-situ PRMMCs by hot pressing. The process of the RHP method is shown in Figure 2.5.

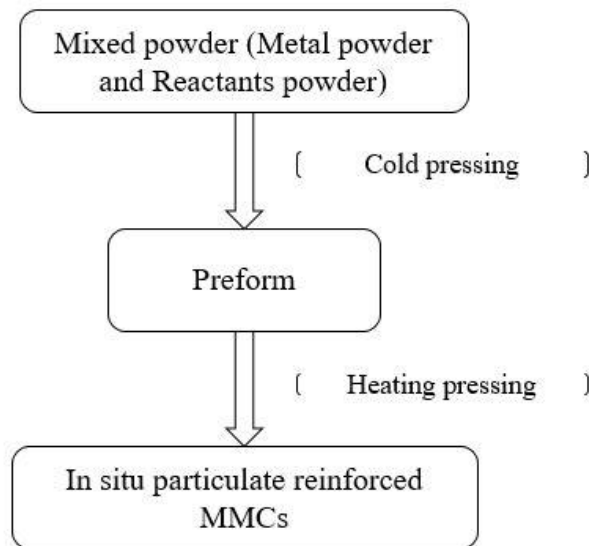


Figure 2.5 Process of RHP Method.

Guisong *et al.* (2004) used an ordinary ball mill to mix Al_2O_3 and TiB_2 powder and Al powder to successfully fabricate in-situ $(\text{TiB}_2+\text{Al}_2\text{O}_3)/\text{Al}$ composites by the RHP method (Tjong, Tam, & Wu, 2003). During the experiment, the uniformly mixed powder was cold-formed in a dry graphite grinder, and then the powder and the graphite abrasive tool were placed in a vacuum hot pressing furnace for heat treatment pressing and sintering to remove pores in the preform. After that, the mixed powder was heated to 600°C , maintained for 25 minutes. Finally, an in-situ metal-based particle-reinforced composite material with a tensile strength close to 500 MPa was obtained.

Unlike the RMA method, the RHP method does not use HEBM equipment; therefore, the powder mixing is relatively inconsistent. However, in the subsequent hot pressing process, the low-melting-point metal can be filled into the porous area of the reinforcing phase to increase the

density of materials. In summary, the RHP method is low in cost, simple in operation, and suitable for mass production.

2.3.1.4 Combustion Assisted Casting (CAC)

The basic principle of the CAC method is to cast a high-temperature metal melt into a mold in which a reactant powder has been previously placed, and after an in-situ reaction, the local PRMMCs are prepared. Since the mixed reactant powder is previously placed in the specific position of the mold, this is an ideal method for the preparation of composite materials that require special properties for localized locations. The fabrication process is shown in Figure

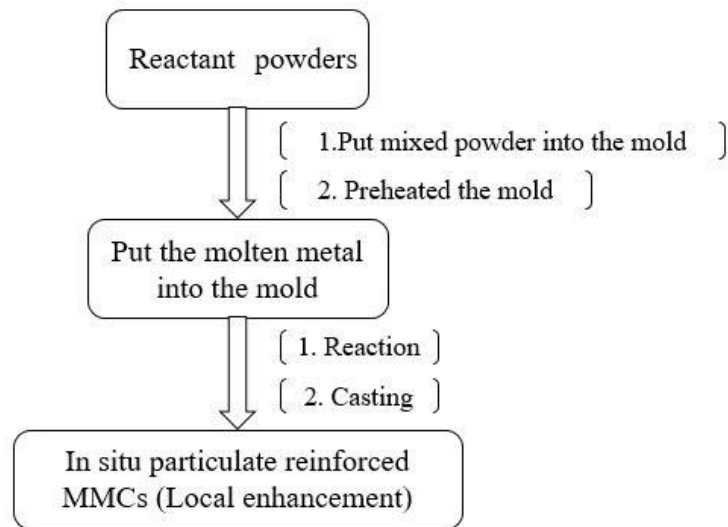


Figure 2.6 Process of CAC Method

For the CAC method, the preheating temperature of the mold play a key role in inducing the combustion chamber reaction.

The above in-situ synthesis processes cannot be used for direct casting, and various types of high-performance and complex particle-reinforced composite materials are currently required in various fields. Therefore, the direct in-situ synthesis process, which is directly castable, is attracting more and more interest as a research topic.

2.3.1.5 Contact Reaction Process (CRP)

The CRP method was developed from the SHS method. In this method, the reinforced powder particles are cold pressed into a uniformly mixed preform. After the preform is placed in the molten metal matrix, chemical reactions between the mixed reactants are initiated by the high-temperature melt. The reinforcing particles are then synthesized in the melt. The process flow diagram of in-situ particle-reinforced Al-MMCs prepared by the CRP method is shown in Figure 2.7.

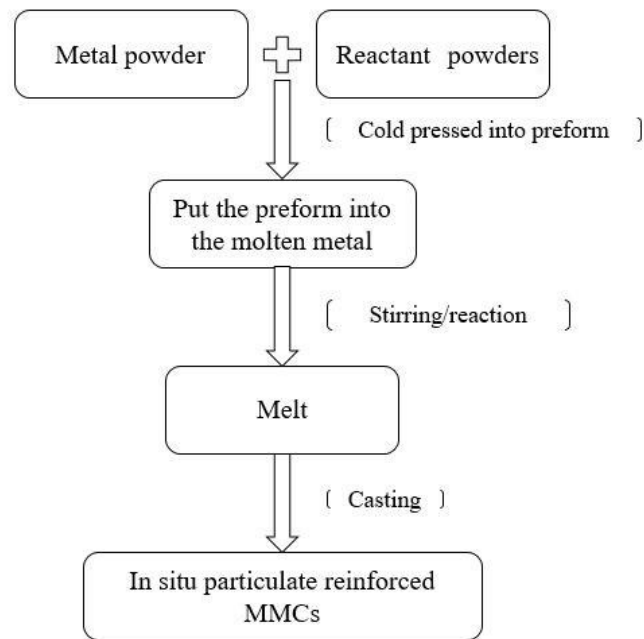


Figure 2.7 The Process of Preparing Composite Materials by CRP Method.

In the process of the CRP method, the molten metal solution needs to be continuously stirred so that the reinforcements can be uniformly dispersed in the melt and the in-situ reaction can be accelerated. Until now, the preparation of Al-MMCs by the CRP method has received more and more attention from scholars. Liang *et al.* (2010) prepared an in-situ TiC/Al-4.5wt.%Cu composite by preheating the mixed powder body of Al-Ti-C at 180°C for 60 minutes and then adding it to a 1000°C Al-4.5wt.%Cu alloy melt. Tee, Lu, and Lai (1999) added a 200°C-preheated Ti-B mixed powder preform to a 1040°C Al-4.5wt.%Cu melt and held it at 1080°C for 20 minutes. Then, an in-situ TiB₂/Al-4.5wt.%Cu composite was fabricated. These experiences showed that the key to the CRP method is the preparation of the preform. For composite

materials, reinforced phase composites with low volume fractions are beneficial for achieving superior mechanical properties. On the other hand, the temperature of the molten metal is also a key parameter of the CRP process. For example, the high temperature of the Al solution during the preparation of Al-MMCs leads to high oxidation and the burning of alloying elements. Conversely, a low melt temperature results in coarse reinforcing particles. In summary, the CRP method is simple to operate and is suitable for the mass production of PRMMCs.

2.3.1.6 Mixed Salt Reaction (MSR)

The MSR method is one of the most popular for preparing Al-MMCs. Wood (1993) successfully fabricated A356/TiB₂ composites via an MSR technique by using K₂TiF₆ and KBF₄. This method has attracted the attention of many scholars because of its low cost and easy to improve production process. The basic principle of the MSR method is to mix the salts containing Ti and B elements in an atomic ratio of 1:2 and then add them to high-temperature molten Al. With high temperature and stirring, Ti and B in the mixed salt are reduced and further reacted to form TiB₂ particles. A schematic of the process of the MSR method is illustrated in Figure 2.8.

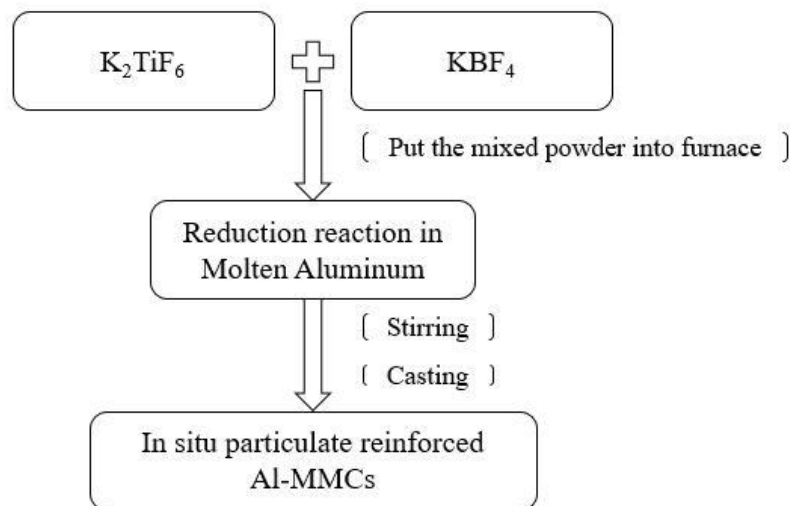
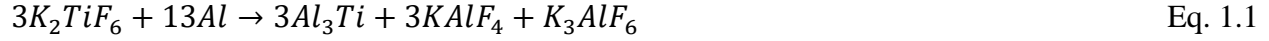
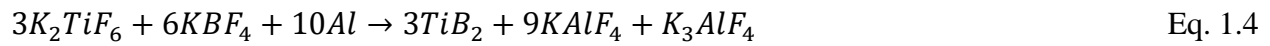


Figure 2.8 Schematic of Process of MSR Method.

Mahallawy, Taha, Jarfors, and Fredriksson (1999) successfully prepared Al-MMCs using the MSR method according to the following reaction equations:



According to Eq. 1.1 and 1.2, Al_3Ti and AlB_2 are formed through the reduction reaction. Then, the TiB_2 phase is generated in the molten Al, as shown in Eq. 1.3. The overall chemical formula is shown in Eq. 1.4, which was also noted in Mahallawy's research to describe the reaction process for synthesizing TiB_2 .



Kumar *et al.* (2008) used the MSR method successfully to prepare in-situ $TiB_{2p}/Al-7Si$ composites with greatly improved mechanical properties. Simultaneously, the mechanism of the TiB_2 formation process in the MSR method has also been extensively studied, as Moldovan *et al.* explained in their paper. The synthesis process of the TiB_2 phase can be split into three main parts as shown below:



First, according to Eq. 1.5 and Eq. 1.6, both K_2TiF_6 and KBF_4 are melted at high temperatures when in contact with the molten Al surface. KF is decomposed from these two salts.

Next, Ti and B atoms in TiF_4 and BF_3 gases react with liquid Al at the Al/gas interfaces. The chemical reaction is expressed from Eq. 1.7 to Eq. 1.8:



The generated Ti and B constantly diffuse into the molten Al, eventually reaching saturation. Al_3Ti , TiB_2 , and AlB_2 are produced in the Al solution according to the following reactions:



TiB₂ has the lowest free energy among the products (AlF₃, KAlF₄) and remains in the Al solution at the end of the chemical reaction. Other products are discharged from the surface of the solution because of their lower densities compared to that of the TiB₂ compound.

The final step of the MSR preparation process is to cast the Al liquid containing TiB₂ particles into the mold. During the solidification, some of the TiB₂ particles act as a nucleating agent, and the other TiB₂ particles are pushed to the grain boundaries by the interface between the grain and the Al liquid. This process is called particle pushing. According to research, particle pushing greatly affects the mechanical properties of MMCs, and this will be discussed later.

2.3.1.7 Direct Melt Reaction (DMR)

The DMR method, also called the melt reaction method, was developed from the MSR method. DMR technology is simple, low cost, suitable for mass production which can form a near net shape, and is considered a forward-looking technology for in-situ particle-reinforced Al-MMC preparation. The in-situ reaction method are mainly used to preparing Al-Ti, Al-Ti-B, and Al-Ti-O systems, and the reinforcements formed are TiC, TiB₂, and TiAl₃ (Zhao, Cheng, Dai, Cai, & Sun, 2003).

Unlike the MSR method, DMR involves directly mixing the solid powder containing the reinforcing phase-forming elements instead of the mixed salt. After the powder is added to the molten Al, the mixed powder directly reacts with the melt to form reinforcing particles, and then the in-situ particle-reinforced Al-MMCs are prepared (Huashun, Hongmei, Liming, & Guanghui, 2006).

Yu *et al.* (2005) added mixed powder of Al and Ti powder to an Al solution of 900–1000°C and successfully prepared an in-situ $\text{Al}_3\text{Ti}_p/\text{Al}$ composite by the DMR method. The chemical reaction equation is shown in Eq. 1.12.



Yu *et al.*'s research was significant, as they proposed a simple preparation process for in-situ $\text{Al}_3\text{Ti}_p/\text{Al}$ composites. However, the process preparation temperature was high (900–1000°C), which led to an increase in production cost. From another aspect, the Al_3Ti particles in the prepared composite were mostly rod-like structures, which affected the mechanical properties of the materials due to anisotropy. The average size of the reinforcing particles in the Al matrix was large (more than 50 μm), meaning they could easily cause cracks in composites due to internal stress. Together, these shortcomings limit the application of DMR in actual production to some extent.

2.3.1.8 Direct Metal Oxidation (DIMOX™)

The DIMOX™ method was invented by Lanxide in the United States in 1989. This fabrication method is based on the reactive melt infiltration (RMI) technique. The basic principle of DIMOX™ is to use metal oxides to prepare composites. Specifically, the preparation of this method is described in Figure 2.9.

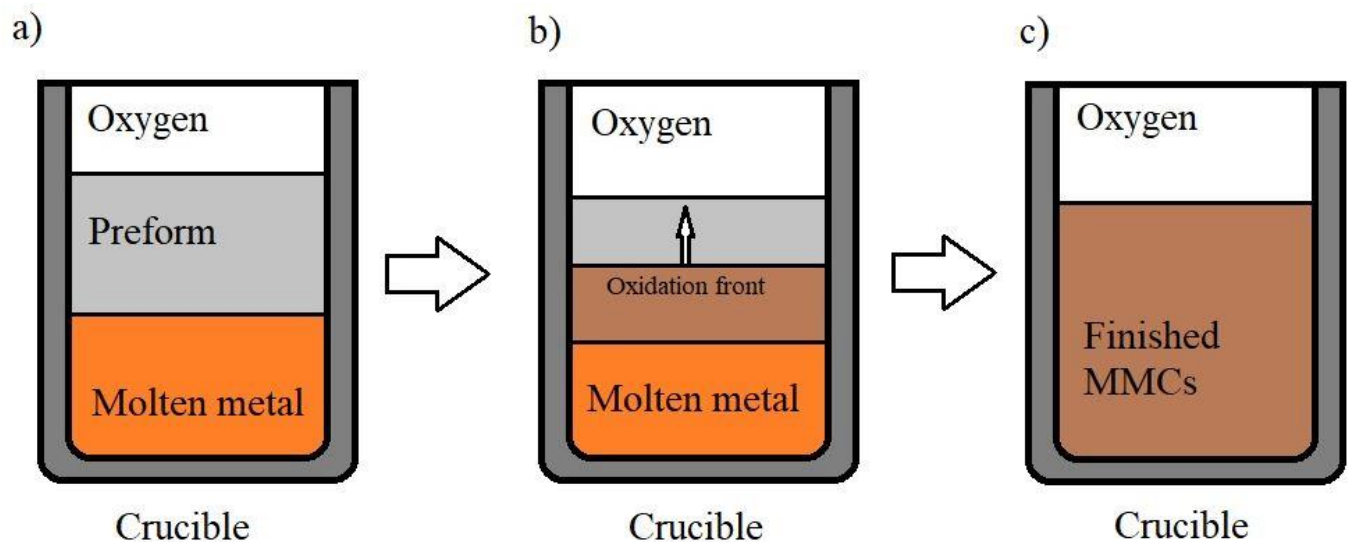


Figure 2.9 Process of Fabrication of MMCs by DIMOX™

First, the preform of dispersed particles is placed on the surface of the molten metal. The reaction process requires an oxidizing atmosphere. The DIMOX™ process requires two conditions: first, the dispersed particles must be wetted by the melt; second, when the liquid metal is exposed to oxygen, an oxide film is formed on the surface of the melt. The melt penetrates the porous ceramic layer through the capillary effect to the surface of molten metal where can directly contact with the gas, causing the metal to react with the gas, resulting in the growth of the ceramic matrix layer. Then in situ metal oxide enhanced MMCs are fabricated.

The DIMOX™ process is commonly used for the preparation of composites with the matrix from Al_2O_3 . The reinforcing preform is mostly made of Al_2O_3 or SiC particles. The molten Al is heated to 1000–1100°C. The advantages and disadvantages of the DIMOX™ process are summarized in Table 2.1.

Table 2.1 The Advantages and Disadvantages of DIMOX™ Process

Advantages:	Disadvantages:
Low shrinkage.	Low productivity
Low residual porosity	Residual Al may be present in the oxide matrix
Good mechanical properties	
Inexpensive and simple equipment	

2.3.1.9 Vapor Liquid Synthesis (VLS)

Koczak *et al.* (1993) developed the VLS process, and its basic preparation principles are described in Figure 2.10.

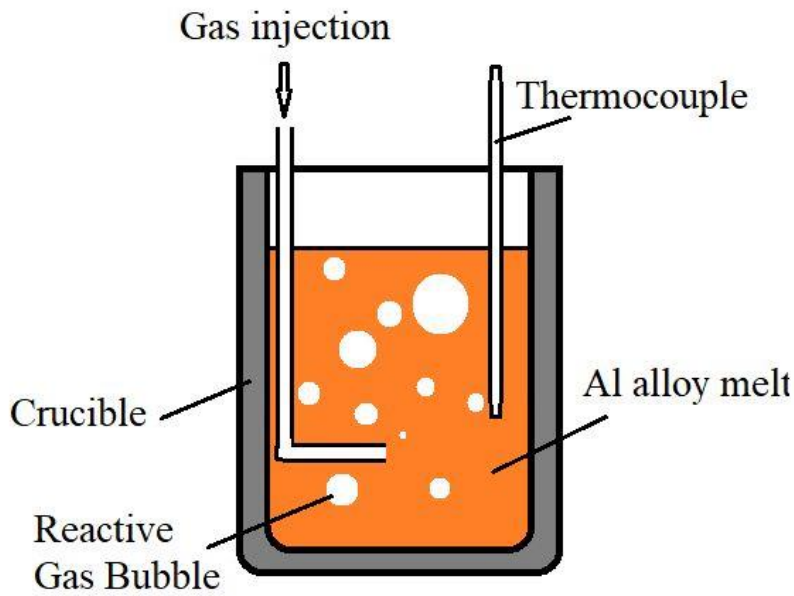


Figure 2.10 Schematic of Fabrication of In-situ PRMMCs Using VLS.

The basic principle of the process is to pass a carbon-containing inert gas into an Al alloy melt containing titanium. Carbon or nitrogen is decomposed from the gas that reacts with the titanium in the alloy, then tiny TiC or TiN particles are formed in the melt through reactions.

Argon is usually used as a carrier gas, and CH₄ or C₂H₂ is used as a carbon-containing gas. The above gas can be fully decomposed at 1100–1400°C. The formation of reinforced phases through gas–liquid reaction is illustrated from Eq. 1.13 to Eq. 1.15.

Gas decomposition:



Carbon reaction and carbide formation:



OR



The VLS method can produce micro-sized reinforcing particles with clean surfaces that are around 0.1–5µm. After the reaction, the melt can be prepared for composite materials that have complicated shapes through a casting process. However, the shortcomings of this method include the limited types of reinforcing phases, low volume fraction of reinforcements, and high melt-temperature, which all contribute to the poor adaptability of the VLS method.

2.3.2 Typical Ex-situ Method of Fabricating Al-MMCs

In addition to the in-situ process, PRMMCs can also be synthesized using an ex-situ method. It is widely applied on the preparation of Al-MMCs and attracted great attention from many scholars. Typically in the ex-situ method preparation process, the reinforcements are pre-synthesized and externally added to the matrix, such as by stirring or secondary processing. An ex-situ process usually has various characteristics such as precise control of the volume fraction of the reinforcing phase, simple preparation process, and various types of reinforcing phase. However, the ex-situ method usually causes the intimately bonded between the reinforcing phase and the matrix, and the phenomenon of particle agglomeration is difficult to avoid either. Ex-situ processes are mainly divided into three categories, as shown in Figure 2.11.

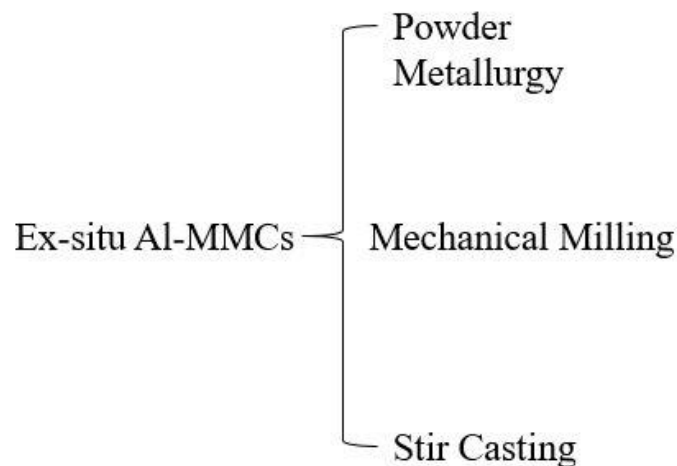


Figure 2.11 Classification of Ex-situ Al-MMC Preparation Processes.

2.3.2.1 Powder Metallurgy Method

The process of powder metallurgy method usually including three steps. First, fine powder of the primary material is produced. Second, the powder is put into a mold for compaction. Finally, the product is formed by hot pressure for long setting times. The manufacturing of reinforcing particles is the first step of the powder metallurgy process before mixing the ceramic reinforcements with the metal matrix powder. Afterward, hot isostatic pressing, extrusion, or sintering is introduced into the process to ensure the consolidation of the powder into a preform. Powder metallurgy is well suited for the fabrication of particle-reinforced Al-MMCs. Kang *et al.* (2004) successfully prepared nano-sized Al_2O_3 particle-reinforced Al-MMCs using powder metallurgy. The particle size of Al_2O_3 was around 50 nm, and the matrix material was commercial pure Al powder with an average size of about 28 μm . During the process, wet mixing was used, with Al powder mixed with varying volume fractions of Al_2O_3 powder in a pure ethanol slurry, followed by drying at 150°C and then cold isostatic pressing the mixed powders into a preform. Finally, the mixed powders were sintered in a vacuum furnace at 620°C to get the composites. Varieties of Al composites with different volume fractions of nano-sized reinforcement were developed. The fabrication process is illustrated in Figure 2.12.

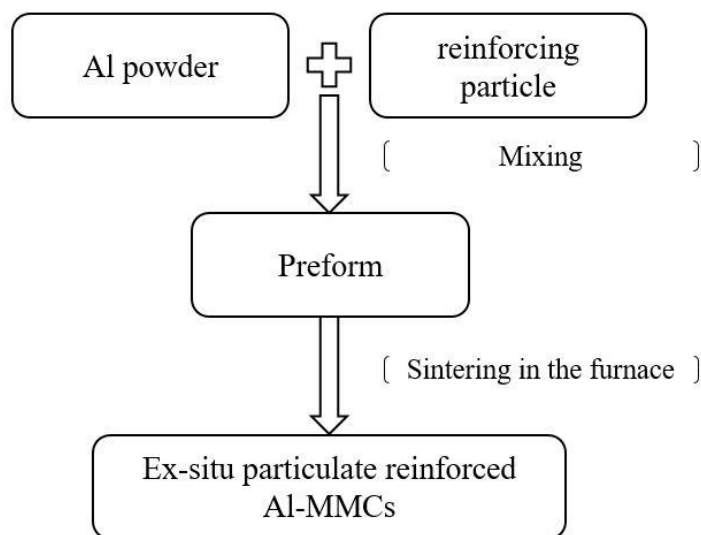


Figure 2.12 Process Flow Schematic of Powder Metallurgy Method.

The production of particle-reinforced Al-MMC by powder metallurgy has many advantages over conventional processes. Including reducing production costs, ingredient customization; stable quality, etc. However, due to the limitations of the process, the powder metallurgy method is not easy to prepare for large-volume composite materials, and the processing cost of sintered abrasives is higher than that of cast molds. The inability of direct casting can be considered a major drawback of powder metallurgy technology.

2.3.2.2 High Energy Ball Milling Method.

The oxide-dispersed alloy (ODS) method using HEBM was fabricated in the late 1960s by Benjamin *et al.*, who also developed the HEBM method (Zhang, 2004). The premise of the process is to utilize the rotation and vibration of ball milling to create a strong impaction between the grinding media and raw materials. With the raw materials being crushed and mixed by ball milling, the alloy or composite powder can be generated by optimizing and controlling the milling parameters. The bulk form of PRMMCs can then be fabricated by combining ball milling powder production with hot extrusion or hot isostatic pressing. Cost effectiveness, high productivity, ease of fabrication, and capability of producing nanoparticles or nanocomposites of high melting-temperature metal or alloy are the advantages of the HEBM processing technique that cannot be achieved by conventional methods. Yet, high energy consumption and inclusion may also increase production costs.

The report pointed out that a main difficulty in the preparation of MMCs is acquisition of ideal mixed powder between the matrix powder and the reinforcing particles. Therefore, HEBM has received significant attention from scholars due to the high efficiency of mixing powders. Hanada *et al.* (1997) produced Al-Li/SiCp composites by using this process. In their research, a mechanical milling method was used to disperse fine SiC particles in an Al-Li matrix powder. The results indicated that the application of the mechanical milling method to the mixing process gave a homogeneous distribution of reinforcements and finer grain structures to the Al-Li composites. This suggests that it would be beneficial to introduce HEBM technology to the preparation of composite materials.

2.3.2.3 Stirring Techniques

Due to its simplicity, flexibility and suitability for mass production of commercial components, stirring casting technology has been widely applied on MMCs preparation. The basically process of stirring method is simple: first, melting the matrix material in a crucible, adding the reinforcing agent to the melt while stirring and applying ultrasound to help dispersed reinforcements. Finally, casting in the mold. The stirring casting process is shown in Figure 2.13.

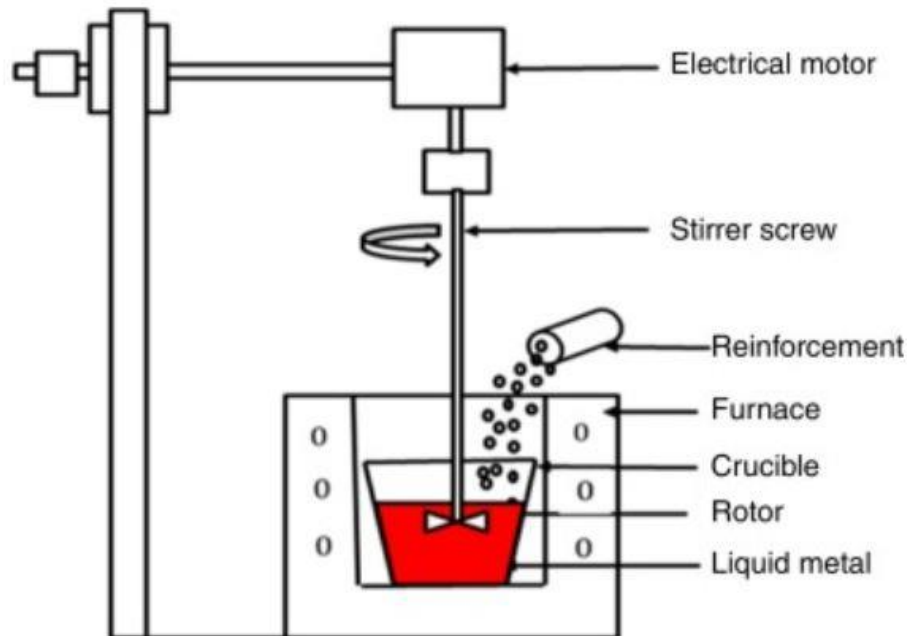


Figure 2.13 Stir Casting Technique for Fabrication MMCs.

Suresh *et al.* (2014) fabricated Al6061-TiB₂ composites. The research indicated that Al6061 was reinforced with various percentages of TiB₂ particles by using the high-energy stir casting method. Composites were prepared in an induction furnace by melting Al at around 800°C along with stirring and adding TiB₂ particles, which were preheated to 450°C. After stirring, the melts were cast using a die-casting machine under a pressure of 100 MPa. The stirring method is simple in process and can accurately control the volume fraction and the size of the reinforcing particles. It can be used for the manufacture of complex parts and for large-scale industrial production. In summary, the stirring process is a promising preparation of particle-reinforced Al-MMCs that is worthy of further study. However, the disadvantages are also obvious. For

example, the reinforcements are easily oxidized when exposed to air under high temperatures, and the nano-sized particles are easily agglomerated in the melt. With the introduction of ultrasonic treatment and ball milling, the above shortcomings have been improved, which will be further discussed later.

2.3.3 High-Intensity Ultrasound in Liquids

Generally, ultrasound refers to sound waves with a frequency of 2×10^4 – 10^9 Hz. Ultrasound can be used as a carrier or medium for the detection of low-intensity frequency (i.e., detecting ultrasound). When the intensity exceeds a certain value, it can interact with the medium through ultrasound to change the state, nature, and even structure. In this context, the ultrasound wave is referred to as HIU (Liu, Han, & Li, 2012; Li, Momono, Ying, Zheng, & Tayu, 2007).

HIU can produce cavitation in the melt. The change in the flow, pressure, and temperature fields in the melt caused by the mechanical mechanism produces a special effect in the metal melt.

As described by Neppiras, cavitation might occur “whenever a new surface, or cavity, is created within a liquid, a cavity being defined as any bounded volume, whether empty or containing gas or vapor, with at least part of the boundary being liquid” (Ramirez, Qian, Davis, Wilks, & St. John, 2008).

The definition covers such phenomena as boiling and effervescence, which involve underwater expansion of the gas phase before the contraction of existing cavities occurs. According to Neppiras, the term “acoustic cavitation” is, therefore, usually restricted to cases involving both expansion and contraction of cavities or bubble nuclei.

Cavitation bubble generation involves the following three processes: the formation, growth, and collapse of cavitation bubbles. As the ultrasonic waves propagate through the melt, the liquid molecules are subject to the effect of the surrounding alternating sound field. In the sonic sparse phase, the liquid receives tensile stress and is cracked to generate cavitation bubbles or voids when the sound pressure is sufficiently large (Noltingk & Neppiras, 1950; Neppiras, 1984). At this time, the tiny bubbles in the liquid are filled into the cavitation bubbles or cavities, inducing

the growth of the cavitation bubbles. In the subsequent positive pressure phase of the sound waves, these cavitation bubbles or voids are closed or collapsed at a very high speed, which leads to instantaneous localized high temperatures and pressures in the liquid.

It was indicated that the cavitation bubbles originate from tiny bubbles in the liquid, yet not all bubbles can be converted into cavitation as cavitation cores (Noltingk & Neppiras, 1950; Neppiras, 1984). The condition is that the sound pressure in the liquid must exceed a certain threshold. In other words, when the radius of the microbubbles in the liquid is R_0 , the ultrasonic cavitation threshold, P_c , can be expressed by the following formula:

$$P_c = P_0 - P_v + \frac{2}{3\sqrt{3}} \sqrt{\frac{(\frac{2\sigma_{LG}}{R_0})^3}{P_0 - P_v + \frac{2\sigma_{LG}}{R_0}}} \quad \text{Eq. 1. 16}$$

P_0 : Static pressure of liquid;

P_v : Saturated vapor pressure of liquid;

R_0 : Bubble radius;

σ_{LG} : Solution surface tension;

From the equation that the threshold value P_c of the ultrasonic cavitation varies with the type of liquid. In the same type of solution, the threshold value also changes as the temperature, pressure, and gas content changes. The smaller the bubble radius R_0 , the higher the value of the threshold.

In an ultrasonic field with a certain sound intensity, the relationship between the minimum bubble radius R_{min} and the amplitude of sound pressure P_A is as follows:

$$R_{min}^3 + \frac{2\sigma_{LG}}{(P_0 - P_v)} R_{min}^2 = \frac{32}{27} \times \frac{\sigma_{LG}^3}{(P_A + P_v - P_0)^2 \times (P_0 - P_v)} \quad \text{Eq. 1.17}$$

The above formula can be reduced to the following:

$$R_{min}^3 + \frac{2\sigma_{LG}}{(P_0 - P_v)} R_{min}^2 = \frac{32}{27} \times \frac{\sigma_{LG}^3}{(P_A - P_0)^2 \times P_0} \quad \text{Eq. 1.18}$$

It can be seen from Eq 1.18 that as P_A decreases, the minimum bubble radius (R_{min}) of the cavitation increases. If P_A in the liquid does not reach the threshold, cavitation will not occur.

In addition, a large number of experiments have shown that the ultrasonic cavitation threshold is also related to the acoustic frequency. There have been many calculations on the sound pressure value, the cavitation bubble critical radius, and other factors, but because they are not the focus of this study, they are not described in further detail here. The finite amplitude attenuation is produced by the interaction of sound waves and liquid viscous forces when the ultrasound propagates through the liquid. Thereby, a sound pressure gradient is formed in the liquid from an ultrasound wave, resulting in the flow of the liquid. In the case of HIU, when the sound pressure amplitude exceeds a certain value, a fluid injection is generated inside the liquid. After it exits the end of the ultrasonic hood, a circulation of flow is formed throughout the fluid, as shown in Figure 2.14, driving the high-velocity flow of the entire solution (Wan, Pan, & Yang, 1995).

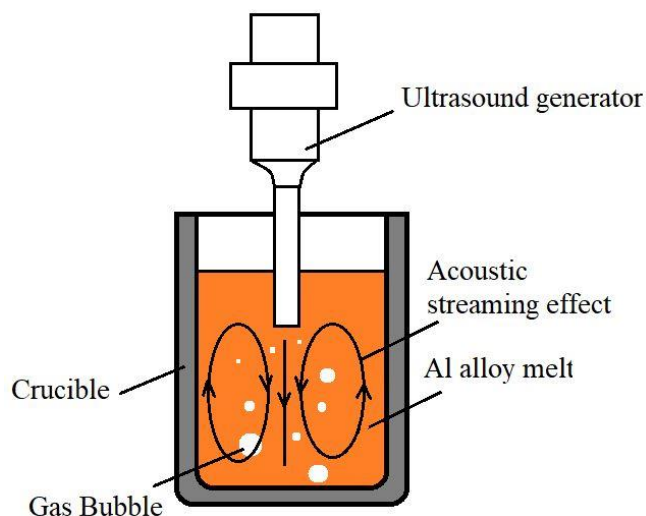


Figure 2.14 Schematic Diagram of Acoustic Streaming

As mentioned earlier, high-intensity ultrasound can create cavitation and acoustic streaming in the metal melt. These effects can significantly optimize material structure and improve product properties.

2.3.4 Application of High-intensity Ultrasound in Particulate Reinforced Al-MMCs

The high HIU technique is mostly used in the stirring preparation method of particle-reinforced Al-MMCs. In the classic stirring preparation method, problems such as particle agglomeration, high porosity, and oxide inclusion greatly affect the mechanical properties of the composite materials. Its main roles are as follows:

1. Dispersion effect:

The effect of ultrasound on the dispersion of particles in the melt is the result of a synergistic effect of cavitation and acoustic flow effects. The high-frequency shear force and local high pressure generated by the cavitation effect can effectively break up the agglomerated reinforcing particles, and the dispersed particles uniformly disperse the internal flow of the liquid generated by the acoustic flow effect in the matrix (Xu, Meek, & Han, 2007).

2. Degassing:

The gas dissolved in the metal melt, the gas entrained in the gas core, and the gas in the agglomerated particles can enter the cavitation bubble under the action of ultrasonic cavitation before growing continuously and finally rupturing on the surface of the melt. During the ascension of the bubble, the oxide inclusions in the melt can be brought to the surface of the melt to complete the slag removal (Xu, Jian, Meek, & Han, 2004).

3. Wetting:

Young (1984)'s equation is as follows:

$$\cos \theta = \frac{\sigma_{SV} - \sigma_{SL}}{\sigma_{LV}} \quad \text{Eq 1.19}$$

θ : Contact angle;

σ_{SV} : Solid/gas interface energy;

σ_{SL} : Solid/liquid interface energy;

σ_{LV} : Liquid/gas interface energy

During the HIU treatment, the impurities adsorbed on the surface of the reinforcing particles are discharged, and the surface energy SV of the particles increases.

Simultaneously, the high-frequency vibration generated by the ultrasonic wave, the high-

frequency pressure generated by the cavitation, and the agitation generated by the sound flow can significantly reduce the surface tension and friction of the liquid, reducing the surface energy LV of the melt. The contact angle of the particles and the metal melt then decreases, and the wettability of the particles and the melt is enhanced.

4. High temperature and high pressure:

The local high temperature and pressure caused by cavitation can change the physicochemical state of the melt so that the processes that cannot be performed or are difficult to perform under normal conditions can be carried out or accelerated.

In recent years, the preparation of particle-reinforced Al-MMCs with the HIU technique has been extensively studied. Ma *et al.* (2003) of Southeast University prepared SiC_p/Al and Si₃N_{4p}/Al composites with the high-strength ultrasonic method using SiC and SiN₄ particles. The research result indicated that micron-sized ceramic particles can be uniformly dispersed in the Al matrix through HIU. The cavitation effect improves the wettability between the ceramic particles and the Al melt, and the composite has fewer pores due to the degassing effect. Yang *et al.* (2004) used the stirring method to prepare nano-SiC_p/Al composites, while Su *et al.* prepared nano-Al₂O₃/Al composites.

2.4 Effect of Particulate Size on the Preparation of Al-MMCs

Since the 1980s, the world has been rapidly researching and developing micron-sized particle-reinforced Al-MMCs, and they have been successfully produced. The average size of the reinforcing particles is usually greater than 10 μm . Among them, the series of SiC particle-reinforced Al-MMCs (SiC_p/Al-MMCs) is representative. It has the advantages of high specific strength and stiffness, wear resistance, fatigue resistance, low thermal expansion coefficient, low density, high yield strength, and good dimensional stability. However, research on micro-sized particle-reinforced composites has stalled in recent years since large particle sizes and high volume fractions make it difficult to further improve the toughness and plasticity of the composite materials. Figure 2.15 shows the typical microstructure of micron-sized SiC/Al-MMCs (fabricated by Tiejun *et al.* (2008)).

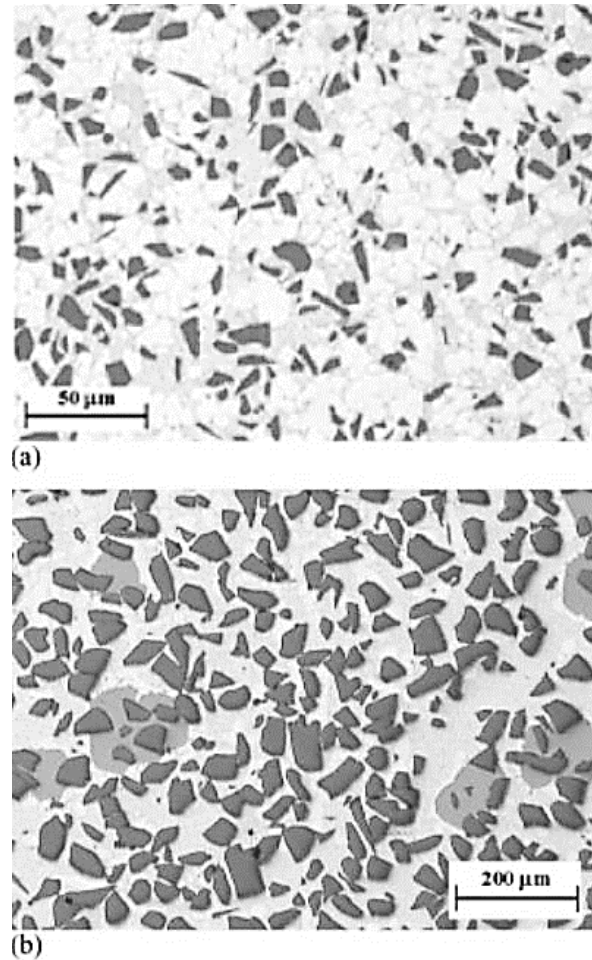


Figure 2.15 Microstructure of (a) 20% SiC/Al and (b) 50% SiC/Al Composites.

As expressed in the diagram, the average radius of SiC particles is about 20 μm, and they are evenly dispersed in the Al matrix. This structure results in the high hardness and low plasticity of the micro-sized SiC/Al composite.

2.5 Nano particulate Reinforced Metal Matrix Composite

With advances in nanotechnology, scholars have begun to pay attention to the application of nano-reinforcing particles and have achieved many results.

MMCs reinforced by nanoparticles, which called metal matrix nanocomposites (MMNCs), have been studied for recent decades. The basic ideal of MMNCs is that by adding a nano-scale

reinforcing material into a metal matrix. Classically, the reinforcement materials are embedded or dispersed into a matrix, which could be made of fibers or particles. During the development of MMNCs in recent years, it has been found that the reinforcement materials can play different role in composites such as improve wear resistance, mechanical properties, friction coefficient, thermal conductivity and structure improvement.

From the literature, several types of nanometric phases as reinforcements have been coupled with different kinds of matrix metals. Many scholars have used ceramic compounds such as SiC, Si₃N₄, TiB₂, Al₂O₃, etc., and intermetallic materials for strengthening Al, Mg, Cu. (Christy, Murugan, & Kumar, 2010). According to the morphological characteristics of the reinforcement, MMCs can be divided into discontinuous (particles, short fibers) and continuous (long fibers, porous ceramics, and lamellar reinforcements) reinforced MMCs. Among them, boron nitride-reinforced MMCs and titanium boride MMCs represent the new MMNC research areas.

TiB₂ have excellent strength and high corrosion resistance due to the thermodynamic stability. At present, research on TiB₂/Al-MMCs mostly focuses on preparation methods optimization and improve mechanical properties. Many researchers have studied the in-situ and ex-situ processes for the fabrication of nano-TiB₂-reinforced MMCs.

Chen *et al.* (2015) fabricated Al-TiB₂ nanocomposites using the flux-assisted melt stirring process. The results indicated that nano-reinforced composites have a low volume fraction (usually less than 5%) and that the micro-hardness of nanocomposites increases significantly with an increase in TiB₂ level.

It can be seen that nanoparticle-reinforced composite materials have great potential. However, when the average radius of the reinforcing particles reaches nano-scale, the preparation of the composite material also becomes more difficult, as summarized in the following three points: 1. The agglomeration of nano-reinforcing particles becomes more likely. 2. Adding nano-reinforcing particles into the metal matrix becomes difficult (poor wettability). 3. The most of reinforcing particles in the matrix are pushed by advancing solid-liquid interface to the grain boundary during the solidification of the metal solution, affecting the microstructure and properties of the material.

The third problem appears to have the greatest impact on the properties of composites, since the distribution of reinforcements in the matrix is the key factor to determine the microstructure of the composite, which in turn affects the mechanical properties of the composite. It is pointed out that in the process of preparing PRMMCs using the stirring method, the final distribution condition of the reinforcements mainly depends on the behavior of the particles in the molten Al during solidification. Therefore, elucidating the behavior of particles is important for improving the preparation of composites.

2.6 Particle Pushing

As a classic theory, Particle pushing has been studied since 1960s. It is the common phenomenon for PRMMCs that the reinforced particles dispersed in the matrix are redistribute in the solidification process. As the solidification continues, the particles in the molten matrix can be engulfed or rejected by advancing front. The prediction and simulation of particle behavior during the solidification has been widely concerned by scholars since the introduction of particle pushing theory.

Understanding the mechanism of particle redistribution in the matrix plays an important role in actual production and research. In recent decades, the research on particle pushing is based on thermodynamic and kinetic criteria. Many scholars establish a balance model by analyzing the forces on the individual particle under ideal conditions to predict the behavior of particles during solidification. However, the solidification process is very complicated, so there is great uncertainty in the behavior prediction of the particles, and the mechanism of particle pushing is still under discussion. The earliest experiments of particle pushing were based on water-ice system that claims there exists a critical velocity (V_C) as a criterion for predicting particle behavior. According to the classic theory developed by Uhlmann *et al.* (1964), the particles are pushed out by the advancing front when the growth rate of the grains is lower than V_C ; otherwise, particle engulfment (i.e., incorporation of a particle by a planar interface) occurs.

The main research work involving particle pushing is aimed at MMCs. Youssef *et al.* (2005) suggested many factors affecting the behavior of particles at a solid–liquid interface which include the size and shape of particle, viscosity of the molten melt, density of the matrix and the shape of liquid-solid interface. Also, Han *et al.* (1995) reported the gravity acting on the particles, the van der Waals forces between the particles and the interface, the temperature coefficient in the liquid, the concentration gradient, and the flow in the liquid also have a large effect on the behavior of the particles at the interface.

Since the actual situation is more complicated, the research mainly discusses PRMMCs, and the system composition mainly includes solids, liquids, and particles. The models are presented in the article, which, based on semi-quantitative foundations, refers to a particular particle with a specific size. Macroscopically, the equilibrium equation can be established by the change in particle concentration. Figure 2.16 illustrates the particle concentration in the solid–liquid system.

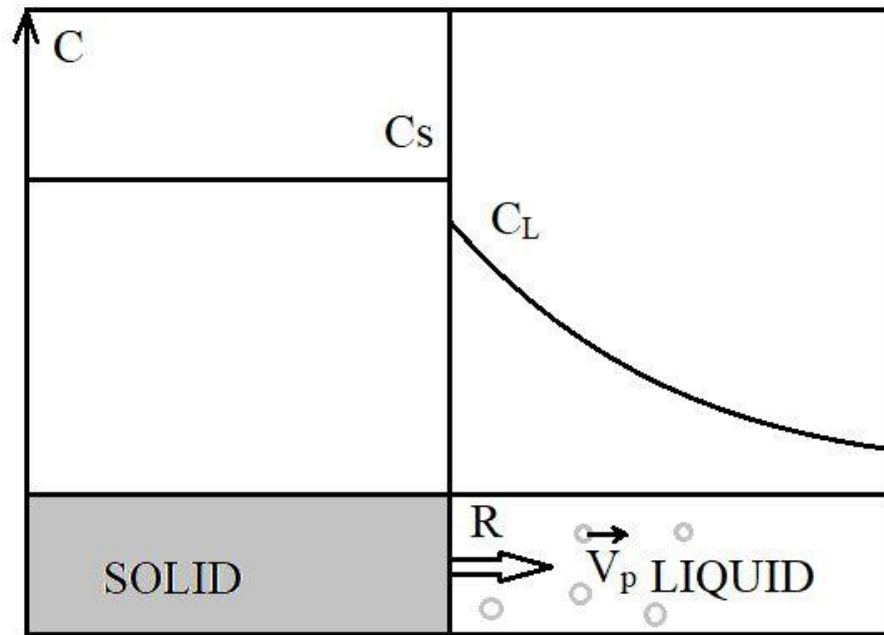


Figure 2.16 Particle Concentration in Solid–liquid System (Han, & Hunt, 1995).

Assuming R is the growth rate of the solid–liquid interface and the particle concentrations are represented by C_s and C_L (number of particles per unit volume in solid or liquid sections,

respectively), the total number of particles engulfed by the growing front is consistent with the total number of particles being pushed away from the liquid phase. That is (Han, & Hunt, 1995):

$$RC_S = C_L(R - V_p)P \quad \text{Eq. 2.20}$$

where V_p is the particle velocity that is normal to the interface. The left side of Eq. 2.20 is the total number of particles embedded in the growing interface, and the right side is the total number of particles leaving the liquid. P is a parameter ($P = 0$ or 1) that determines whether the particles are pushed or rejected by the freezing front. When the particle concentration in the solid (C_S) is zero, it means that all particles are rejected by the advancing interface, and that P must, therefore, be zero.

Extensive work has been carried out to predict the behavior of reinforced particles in the matrix. For many years, academics generally believed that particles are either trapped or rejected by the continuous interface during solidification. A prediction model based on surface energy considerations was established by Uhlmann *et al.* (1964) through a water–ice system experiment. As the foundation of particle pushing research, the surface energy model has been accepted and investigated by many scholars for many years.

2.7 Surface Energy Models

The criterion based on surface energy model can be applied to ideal conditions including a smooth flat surface and ideal spherical particle system. The model assumes that the free energy of the interface changes with the distance between the particle and interface. The basic ideal system is illustrated in Figure 2.17.

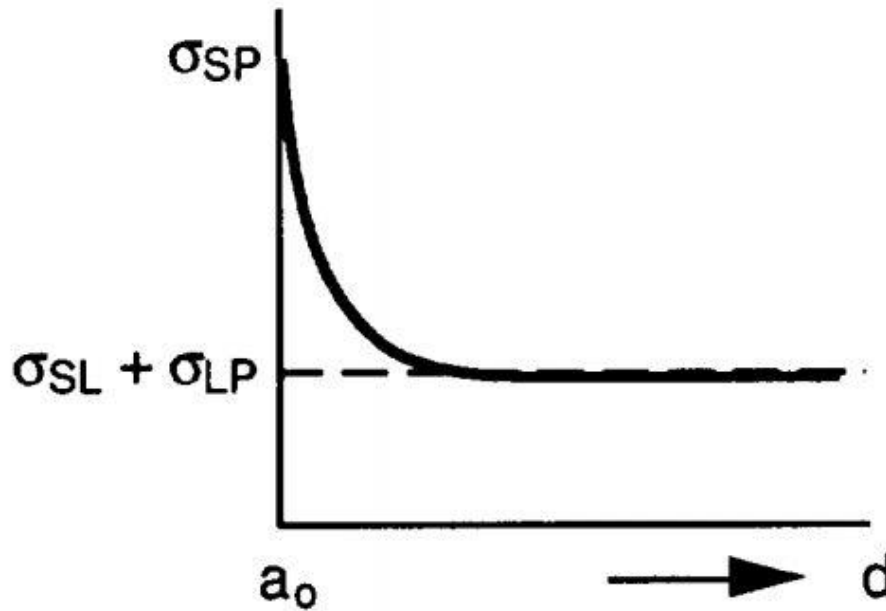


Figure 2.17 Variation of Interface Energy.

The subscripts S , L , and P correspond to the solid, liquid, and particle, respectively. Here, d is the distance between the particle and the interface. The criterion shows that a particle will be pushed when the interfacial energy between the particle and the solid phase, σ_{SP} , is larger than the sum of the solid–liquid free energy, σ_{SL} , and liquid–particle free energy, σ_{LP} , which can be explained by Eq. 2.21 (Uhlmann, 1964):

$$\Delta\sigma_0 = \sigma_{SP} - (\sigma_{SL} + \sigma_{LP}) \quad \text{Eq. 2.21}$$

The free energy generally tends to be the lowest, so ideally, the particles remain at a certain distance from the solid–liquid interface until the balance is broken (Wang & Han, 2014).

Scholars often use thermodynamic criteria as filter foundation to chose a second reinforcement phase or grain refiner in metal matrix.

Based on the equilibrium equation explained by Eq. 2.21, Uhlmann *et al.* (1964) developed a predictive model to determine whether the particle will be rejected or engulfed by the solidification front. The critical velocity (V_C) of the solidification front in the equation quantifies

the particle pushing/engulfment transition. Various forces acting on the particle are considered, yielding an expression for the critical velocity as shown in Eq. 2.22.

$$V_C = 2(n + 1) \frac{La_0v_0D}{kTd^2} \quad \text{Eq. 2.22}$$

where D is the diffusion coefficient of the liquid between the particle and solid, v_0 is the atomic volume, a_0 is the order of a molecular diameter, L is the latent heat, k is Boltzmann's constant, d is the particle diameter, T is the temperature, and n is a positive number.

In the predictive model based on the surface energy model, reinforcing particles should be rejected by freezing fronts only when the local solidification rate is less than the critical velocity.

Based on the thermodynamic equilibrium conditions of surface free energy, several authors later modified or refined the treatment of the particle pushing problem by considering the various geometries of the particle and interface as well as force-acting analysis of particles in more complicated environments.

Omenyi and Neumann presented a thermodynamic demonstration of a qualitative investigation (Omenyi & Neumann, 1976). They suggested that particle engulfment occurs when the change in the interface energy of a system is negative; otherwise, the particle is expected to be rejected by the freezing front. It is determined based on Eq. 2.23.

$$\Delta\gamma = \gamma_{PS} - \gamma_{PL} \quad \text{Eq. 2.23}$$

Engulfment when $\Delta\gamma < 0$.

Pushing when $\Delta\gamma > 0$.

The prediction based on surface thermodynamic criterion in the case that is ignoring forces on particle. The experimental results indicate that particles can be embedded in biphenyl or naphthalene organic solutions.

By considering the shape of the freezing front, Balling *et al.* modified the treatment of particle pushing. The drag and gravity forces are introduced in the body force balance equation. The critical velocity is described by the following:

$$V_C = \frac{\theta_2 \Delta \sigma_0}{\mu a} \left(2 - \frac{k_P}{k_L} \right) \quad \text{Eq. 2.24}$$

where k_P and k_L correspond to the thermal conductivities of the particle and the liquid, respectively.

Chernov *et al.* (1993) introduced the idea of positive disjoining pressure in the liquid films in their models, which separates particles from the advancing interface, leading to repulsive interfacial forces.

The model considers smooth spherical particles and introduces the effects of thermal conductivity differences between the particles and the melt to account for rough interfaces. The viscous drag is the driving force that causes the particles to be engulfed in the model. The presence of positive disjoining pressure results in particle rejection, while negative pressure results in engulfment.

There are two models have been established by using the idea that a repulsive force as a drive forces to push the particles away from the solidification front (Stefanescu, 1988; Shangguan, 1992). The attractive force between the interface and the particle was assumed to be the drag force of Stoke's equation that was also from Uhlmann's model. The surface free energy change shown in Eq. 2.25 has determined by the distance between the interface and the particle (Youssef, Dashwood, & Lee, 2005).

$$\Delta \gamma = \Delta \gamma_o \left(\frac{h_o}{h} \right)^n \quad \text{Eq. 2.25}$$

where

$$\Delta \gamma_o = \gamma_{PS} - (\gamma_{PS} + \gamma_{SL}) \quad \text{Eq. 2.26}$$

h_o : Minimum distance between the particle and the interface;
 γ : Surface free energy.

The exponent value has a range of 2 to 7 depending on the type of repulsive force. The thermal conductivity difference between the particle and the matrix is considered to correct the shape of the solid–liquid interface. For the accurate calculation of the surface free energy change and the type of repulsive force described in the exponent n , the model is not given.

2.8 Limitations of Surface Energy Model

As described in the previous section, the critical velocity is calculated by various methods depending on which factor is considered in the surface energy model. Commonly, the calculated V_C decreases as the particle size increases. If the rate of solidification of the matrix is sufficiently fast, the particle will be engulfed by the continuous interface according to the prediction. However, many experimental results indicate that the particles are rejected by the freezing front in the alloy at a growth rate that is thousands of times larger than the predicted critical velocity. Meng *et al.* (2014) prepared an Al-Ti-B master alloy and evaluated mechanisms acting on particle pushing. The results suggested that most of the particles were rejected by the dendritic solid–liquid interface under a growth rate larger than the critical velocity predicted by the surface energy model. Han *et al.* (1995) reported that, In Al alloy matrix system, SiC particles are pushed into the liquid region by Al dendrites for all growth conditions. The surface energy model prediction is inconsistent with these experimental results. Consideration should be given to building models that include flow and diffusion factors, which is also one of the research motivations of this study.

CHAPTER 3. RESEARCH METHODOLOGY

3.1 Outline

The research is mainly divided into two parts: The first part is involves preparing an Al-4.5%Cu composite material, and the reinforcing particle distribution in the prepared composite material is tested to verify the classic models for particle pushing. The second part of the research focuses on the preparation of TiB₂/Al-MMCs. The preparation technology for nanocomposites is explored through different parameter combinations. Based on the understanding of the influence of particle distribution on material properties, HIU and forging processes are introduced to prepare TiB₂/Al composites with excellent properties. The redistribution of particles in the Al matrix is of the most concern in the present research.

In order to clearly introduce the research methodology, the detailed experimental preparations and analyses for the two reactions are given below.

3.2 MSR for Synthesizing Al-4.5wt.%Cu Composite

3.2.1 Raw Materials and Preparation

Al-4.5wt% Cu alloy was chosen because there are a large amount of experimental data available on this alloy, especially at data on second dendrite arm spacing (SDAS) (Flemings, 2006). A clear image of second dendrite arms can be observed in Al-4.5wt.%Cu alloy from metallographic pictures. By measuring the average second dendrite arm spacing (SDAS) in the observation area, the local growth rate of the solid–liquid interface can be obtained through calculation, which leads to the local cooling area. Therefore, as the matrix in the MSR preparation experiment, the Al-4.5wt.%Cu alloy needs to be prepared under certain conditions.

Commercially pure Al (99.9%) and pure Cu (99.9%) were melt mixed at an appropriate ratio to prepare the Al-4.5wt.%Cu alloy. Results of the analysis of the alloy ingot casting are given in Table 4.1.

Table 3.1 Chemical Composition of Al-4.5wt%Cu.

Al	Cu	Si	Fe	Mg	Zn
0.013	0.002	0.25	0.36	4.47	94.87

Following the MSR method, two kinds of chemically pure salts, potassium fluotitanate (K_2TiF_6) and potassium fluoborate (KBF_4), were used to synthesize the TiB_2 reinforcement phase. A specific flux containing MgF_2 and Na_3AlF_6 was also used to help the reactions (Feng & Froyen, 2000; El-Mahallawy, 1999).

First, the Al ingot was melted using an electric resistance furnace and heated to $720^\circ C$. The temperature was maintained, and the weighed Cu chip was slowly added to the melt. The heating temperature is then raised to $85^\circ C$. The mixed powder of the K_2TiF_6 and KBF_4 salts was preheated for one hour, $300^\circ C$, then the weighed mixed salt was added in order to fabricated 5 wt.% TiB_2 particles, the melt temperature was controlled to be $820^\circ C$ or less to avoid unstable reaction, and the reaction time was 30 minutes. Mechanical stirring was introduced during the reaction to make the reaction more complete with a stirring speed of 120 rpm. After the reaction was completed, the residue was removed, and the material was cast into a wedge-shaped model.

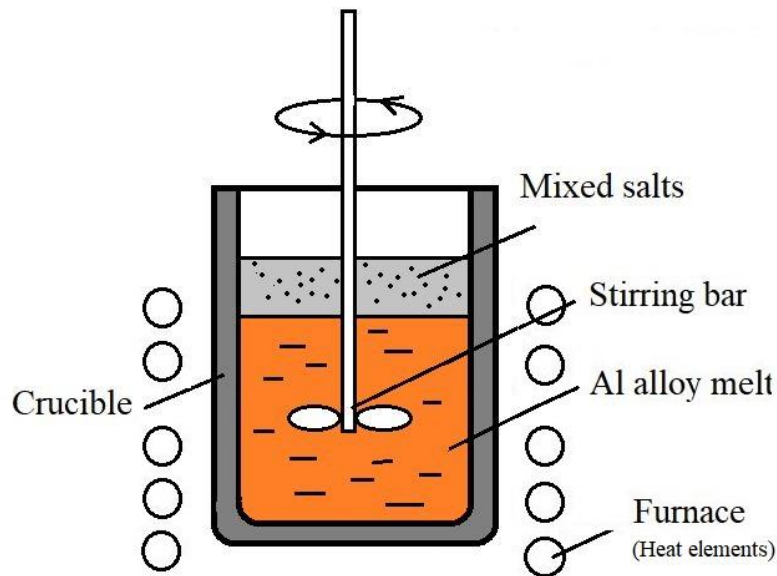
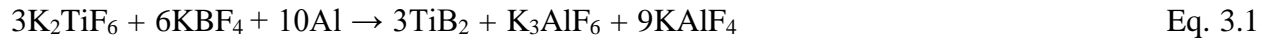


Figure 3.1 Sketch of Mechanical Stirring Process

3.2.1.1 Preparation of TiB₂/Al-4.5wt.%Cu Alloy

TiB₂ and Al₃Ti particles were chosen as reinforcements because both of them are supposed to be powerful nucleates in PRMMCs (Easton, & Stjohn, 1999; Tee, Lu, & Lai, 1999). In this work, TiB₂/Al-4.5wt.%Cu composites were prepared from potassium hexafluorotitanate (K₂TiF₆) and potassium tetrafluoroborate (KBF₄) by an in-situ reaction method. HIU vibration was introduced in the salt–metal reaction. Measured quantities of preheated salt were added to 500 g of molten Al-4.5wt.%Cu alloy at 700°C. Meanwhile, HIU vibration was applied on the melt for 10 minutes. The tip of the radiator was submerged into the melt at about a 1-cm depth. The power of the ultrasonic generator was 1.5 kW and the frequency was at 20 kHz frequency. The salt causes an exothermic chemical reaction and then the melt temperature was increased. Al₃Ti and AlB₂ phases were formed and then decomposed as TiB₂ during the reaction process. The chemical reaction is shown as Eq. 3.1. Then, the KAlF₄ and K₃AlF₆ as slag in the molten melt were removed. Afterward, the molten melt containing Al-Cu-Ti-B was poured into the wedge-shaped mold (Moldovan, Butu, Popescu, Buzatu, Usurelu, Soare, & Mitrica, 2010).



3.2.1.2 Preparation of Al₃Ti/Al-4.5wt%Cu Alloy

An Al-4.5wt.%Cu alloy and K₂TiF₆ salt powders were used in Al₃Ti/Al-4.5wt.%Cu alloy fabrication. In a graphite crucible, 500 g of Al-Cu ingot was melt at 750°C in an electrical resistance furnace. About 48 g of K₂TiF₆ salt was gradually added into the molten alloy after the temperature stabilized. Meanwhile, the salt quickly dissolved into the melt as the melt temperature around 830°C. Then exothermic reaction between the salt and alloy that produced plenty of heat during the reaction process. The reaction equation is shown below.



Mechanical stirring by using a graphite bar was then applied to the molten metal for 30 minutes to break down the Al₃Ti clusters which formed in the molten Al-4.5wt.%Cu. After the stirring, the slag on the melt surface was removed before pouring.

An evaluation experiment was developed in this study to verify the classic theory of particle pushing. The wedge casting of Al alloy ceramic particles uniformly dispersed in the matrix. Various cooling conditions were obtained in each sample for evaluating particle rejection/engulfment during the nucleation stage and the growth stage of the solidification process. The list of wedge castings is shown in Table 3.2.

Table 3.2 Particulate & Matrix of the Wedge Castings

PRMMCs/Alloy	Fabrication	Matrix	Particles
Al-4.5wt.%Cu	MSR	/	/
TiB ₂ /Al-4.5wt.%Cu		Al-4.5wt.%Cu	TiB ₂
Al ₃ Ti/Al-4.5wt.%Cu		Al-4.5wt.%Cu	TiB ₂ /Al ₃ Ti

3.2.2 Samples Analysis

3.2.2.1 Grinding and Polishing Processes

The coupon was ground using SiC sandpaper in sequence using 180, 240, 400, 600 and 1000 grit, respectively. Then the 2 micron diamond compound has been used to polish grinded sample. Finally, the dust and impurities on the surface of the polished sample was washed with an alcohol solution in an ultrasonic cleaner for 240 seconds.

3.2.2.2 Microstructure Analysis

The microstructure of the metallographic specimens was analyzed by using an optical microscope (OM) and a scanning electron microscope (SEM, s4800), and the average dendrite spacing at different cooling rates of the samples was randomly picked and manually measured using ImageJ software.

3.3 Fabrication of Stirring Process of TiB₂/Al with the Assistance of Ultrasound Vibration

3.3.1 Raw Materials and Experimental Process

In the preparation stage, the two salts of TiB₂ powder (30–50 nm) and the K₂ZrF₆ (1–50 μm) salt are mixed using a HEBM equipment at a mixing ratio of 0.2. The rotating speed was set to 1000 rpm for 6 hours. In order to prevent powder oxidation due to overheating, the device is stopped for 10 minutes every 20 minutes working for powder cooling. After ball milling treatment, the produced powder mixture was pressed into a cylindrical coupon (Ø10mm x 20mm at 30 MPa prepared) using a cold pressing machine.

150 g of commercial purity Al (99.9 pct.) was melted using electrical resistance furnace, the temperature was set at 900°C. A pressed preform containing different mass fractions of TiB₂ nanoparticles was added to the molten Al liquid in the experiment. Argon gas was introduced into the crucible to prevent oxidation, and a graphite bar was used to press the preform into the Al liquid. Then the mechanical stirring and ultrasound vibration were alternately performed. The Nb radiator was used as the tip of the ultrasound, and the preform is pressed by Ultrasound radiator into the melt at a depth of about 3cm for a total of 15 minutes, and the vibration was changed every 5 minutes for stirring. The setup of experiment as shown in Figure 3.2 (Wang, Jiang, Wang, Ma, & Zhao, 2004; Liu, Han, & Li, 2011).

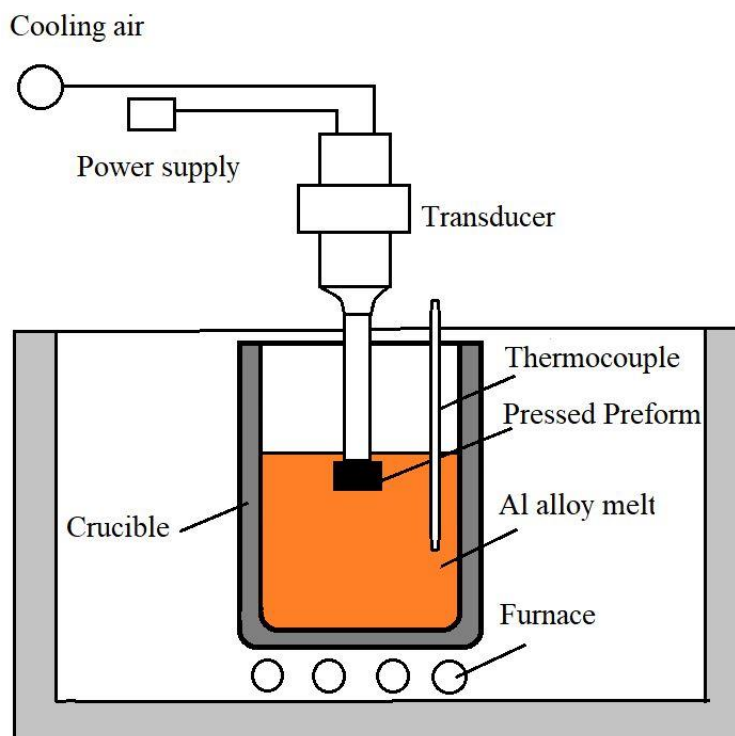


Figure 3.2 Schematic Diagram of Ultrasonic Vibration Assisted Method.

Wait until no longer reacts in the melt, removing the reaction residue from the melt surface, then the Al-TiB₂ composite melt was poured into a cylindrical mold (Ø155-mm).

3.3.2 Forging

The cast ingot were then forged to reduce porosity and to break the grain boundaries of the ingots. The major parameters of the forging process is given in Table 3.3.

Table 3.3 Main Parameters of Continuous Forging Equipment

Equipment	Model	Forging quality	Strike energy	Forging frequency
Pneumatic hammer	C41-750B	750kg	19KJ	105 min ⁻¹

The forging parameters are illustrated in Table 3.4. In order to investigate the influence of the forging process on particle distribution and the resultant mechanical properties of composites,

four types of forging treatment with three volume fractions of TiB_2 particles in MMCs were studied.

Table 3.4 Continuous Forging Process Parameters

Steps	Heating process	Craft
1	Warm up with furnace for 1h to 460°C Insulation 3h	Length $40 \times$ width $22 \times$ height 64
2	The initial forging temperature is about 450°C	Length $38 \times$ width $24 \times$ height 40,
3	Final forging temperature is higher than 350°C	Length $25 \times$ width $25 \times$ height 60
Alternate forging more than 30 times in XYZ order; 40%/60%/80% reduction.		

The forging process is divided into three stages: First, the as-cast TiB_2 reinforced MMCs sample is heated to 460°C in a furnace and held for 3 hours. After that, the sample was forged starting at a temperature of at least 450°C or more for 30 times in each direction of the XYZ coordinate axis. Before, the temperature of the sample was reduced to 350°C . Finally, the sample was cooled to room temperature. The total amount of deformation for the forge process was designed at 40%, 60%, and 80%, respectively.

Composite samples contained three TiB_2 volume fractions corresponding to TiB_2 volume fractions of 1%, 3%, and 5%, respectively. The types of composite and the deformation amount of each material are given in Table 3.5.

Table 3.5 Samples Fabricated Under Different Experimental Parameters

Matrix	Volume fraction	Original	Forging treatment		
			40% reduction	60% reduction	80% reduction
Al	1%	O-1	F40-1	F60-1	F80-1
Al	3%	O-3	F40-3	F60-3	F80-3
Al	5%	O-5	F40-5	F60-5	F80-5

3.3.3 Sample Analysis

3.3.3.1 Grinding and Polishing Process

The coupon was ground using SiC sandpaper in sequence using 180, 240, 400, 600 and 1000 grit, respectively. Then the 2 micron diamond compound has been used to polish grinded metallographic sample. Last, the dust and impurities on the surface of the polished sample was washed with an alcohol solution in an ultrasonic cleaner for 300 seconds.

3.3.3.2 Tensile Strength Test

After the forging process, small tensile test samples were cut from the composite sample bulk, and the surfaces of the tensile test pieces were sanded and cleaned. The sampling method and specifications of the tensile specimens are shown in Figure 3.3.

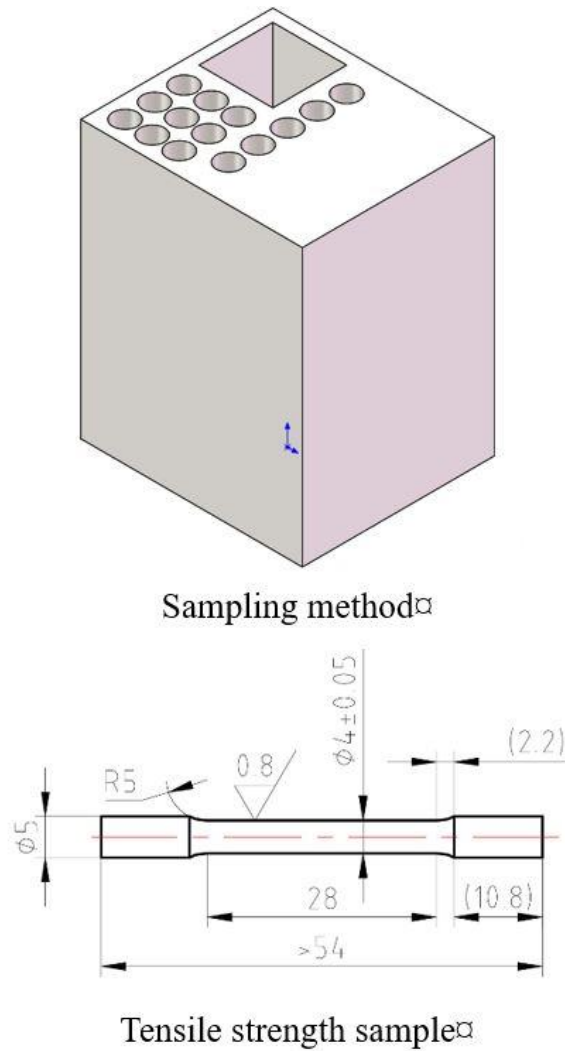


Figure 3.3 Schematic Diagram of Tensile Strength Sample and Sampling Method.

According to different experimental parameters, eight tensile samples were taken for each set of experimental parameters for tensile strength testing, with the average value taken as the experimental result.

3.3.3.3 Hardness Test

The samples with different parameters were tested by the Rockwell hardness method, and each sample was collected at five positions, with the average value used as the hardness data.

3.3.3.4 Microstructure Analysis

The microstructure of the metallographic sample was examined an optical microscope (OM) and a scanning electron microscope (SEM, s4800).

CHAPTER 4. RESULTS

4.1 Outline

The experimental results and discussion are presented in this chapter. For MSR experiments, which were designed to examine theory on particle pushing, the growth rates of the grains at different cooling rates was calculated. The distribution of particles in the Al-4.5wt.%Cu matrix was observed and is compared to the predictive results by surface free energy model. The author of this thesis attempts to analyze the limitations of the classic predictive model and revisit the physics behind the experimental observed phenomenon. Finally, by taking into account the fluid flow that always exists in the gap between the particle and the solid-liquid interface, a new equilibrium model was established in order to analyze the behavioral patterns of the particles during solidification.

In the stirring method for the synthesis of TiB_2/Al composites, the optimization of preparation method was studied. The author improved the classic stirring process to overcome the difficulties of PRMMNCs preparation. In the reinforcement pretreatment stage, the preparation and reprocessing stages of the as-cast composite material, the high energy ball milling technique, HIU technique, and forging processes were introduced to improve the wettability, distribution uniformity of particles, and to reduce agglomeration of the nano- TiB_2 particles in pure Al.

Samples of nano- TiB_2/Al -MMCs produced using our new apparel were characterized. The distribution of reinforcing particles in the matrix and the mechanical properties of the composites were examined. At the end of this chapter, the authors suggest improvements on how to reduce the agglomeration of nano-reinforced particles in the metal matrix.

4.2 Evaluation Experiment

4.2.1 Wedge-shaped Casting

A wedge-shaped casting used for this research is shown in Figure 4.1. After the casting was released from the mold, it were cut in the middle, grinded and polished. Microstructure features, including SDAS, particle size and its distribution were characterized at locations shown in Figure. 4.1. An OM was adopt to exam the SDAS and particle distribution conditions in the Al-4.5wt.%Cu matrix.

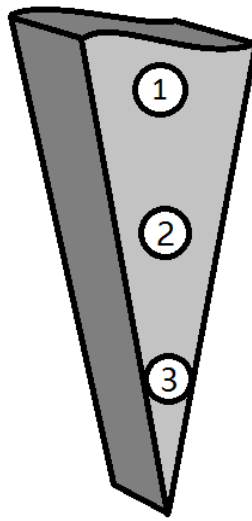


Figure 4.1 Sketch of a Wedge-shaped Casting Used in Experiment.

As shown in Figure 4.1, positions 1, 2, and 3 on each coupon represent three different cooling rates. Due to the special shape of the mold, the rate of solidification in the coupon decreased from the bottom to the top in the vertical direction. When the molten metal was poured into the mold, the liquid that first contacted the bottom would solidify rapidly, and as the mold filling was completed, the region near the position 1 was the last to solidify. The samples for inspection are cut from the three numbered positions corresponding to the different local cooling rates of the wedge castings. The cooling rate around position 1 on the sample is the slowest. In contrast, the solidification rate around position 3 on the sample is the fastest.

For the convenience of comparison, three sets of samples were prepared. The corresponding parameters and numbers of each group in the experiment are shown in Table 4.1.

Table 4.1 Coupon Used in the Research

PRMMCs/Alloy	Reinforcement	Matrix	Position	Label
Al-4.5wt.%Cu	/	/	1	P-1
			2	P-2
			3	P-3
TiB ₂ /Al-4.5wt.%Cu	TiB ₂	Al-4.5wt.%Cu	1	B-1
			2	B-2
			3	B-3
Al ₃ Ti/Al-4.5wt.%Cu	Al ₃ Ti/TiB ₂	Al-4.5wt.%Cu	1	AB-1
			2	AB-2
			3	AB-3

4.2.2 TiB₂/Al₃Ti Particles

Let us consider the relation between the pushing problem and nucleation. TiB₂ and Al₃Ti were chosen as the composite reinforcing particles used in this study because they are classic grain refiners in the aluminum alloy (Lee, & Chen, 2002). Based on this, it is stated that during the solidification process of aluminum alloy, the two particles can be functioned as nucleation sites. During the process of nucleation and growth of the grains, the contact angle of the TiB₂ and Al₃Ti particles in the particle-solid-liquid system is less than 90°, which the mechanism can be depicted in Figure 4.2 (Fleming, 1995).

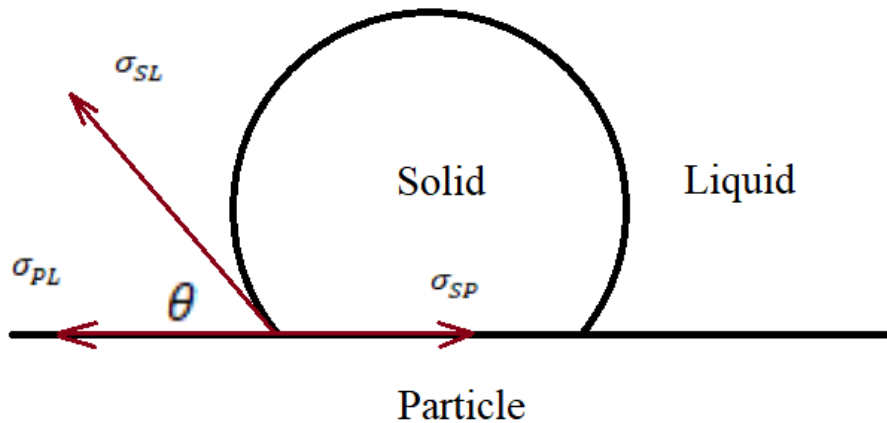


Figure 4.2 Diagram for Analysis of Nucleation Process

According to the equilibrium condition of the surface free energy, it can be clearly seen from the figure that a horizontal force balance yields the equilibrium condition as following Equation 4.1:

$$\sigma_{SP} = \sigma_{SL} \cos \theta + \sigma_{PL} \quad \text{Eq. 4.1}$$

$$\text{when } 0^\circ < \theta < 90^\circ, 0 < \cos \theta < 1$$

$$\therefore \sigma_{SP} < \sigma_{PL} + \sigma_{SL} \quad \text{Eq. 4.2}$$

Compare Equation 4.2 with the engulf condition: $\sigma_{SP} < \sigma_{PL} + \sigma_{SL}$. It can be judged that the TiB_2 and Al_3Ti particles having a contact angle of less than 90° satisfy the nucleation conditions. Therefore, from the thermodynamic criterion, the two particles can be engulfed by moving freezing front in the solidification process of the molten Aluminum.

4.2.3 Al-4.5wt.%Cu Alloy

The Al-4.5wt.%Cu alloy was chosen because the eutectic Al/ Al_2Cu structure can outlines the secondary dendrites, therefore the experimental data of SDAS for the Al-4.5wt.%Cu alloy can be measured accurately from metallographic pictures taken by an SEM and OM. The microstructure of sample P-3 is illustrated in Figure 4.3. By measuring the average SDAS of the Al-4.5wt.%Cu sample, the local solidification time and the corresponding cooling rate was estimated. In addition, the other two PRMMCs with the Al-4.5wt.%Cu alloy poured at the same conditions should have identical cooling conditions at least of the same order of magnitude since the latent heat of these three samples is identical.

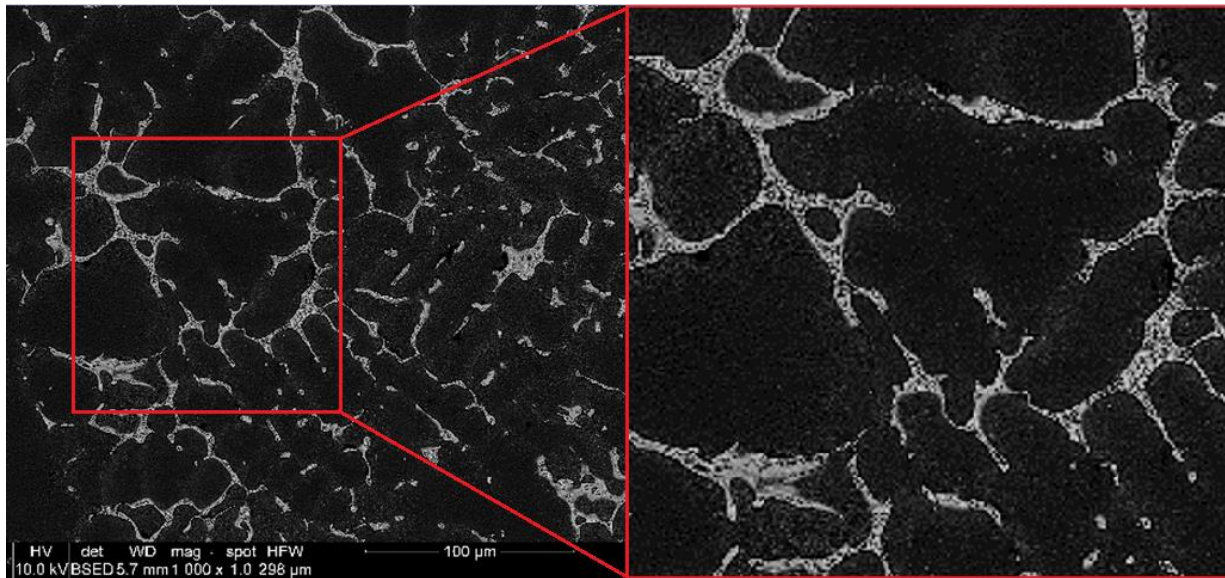


Figure 4.3 SEM Image of Al-4.5wt.%Cu Alloy

As Figure 4.3 illustrates, the bright part on the image is the eutectic Al/Al₂Cu structure that outlines the secondary dendrites. 20 SDAS values were randomly picked and measured in the observation area for the P-1, P-2, and P-3 sample. Then, the average SDAS was calculated, as shown in Table 4.2.

Table 4.2 SDAS of Al-4.5wt.%Cu

SDAS at each position (μm)		
P-1	P-2	P-3
176.2	112.1	48.1
190.3	90.1	57.1
177.1	128.4	80.0
184.1	116.3	65.0
182.2	107.2	53.3
176.2	112.1	52.3
160.3	87.3	59.3
179.2	67.1	60.2
184.3	101.2	46.5
181.2	119.1	52.2
191.6	98.9	44.5
186.3	89.1	68.2
189.4	119.6	61.3
192.4	129.0	53.3
208.4	128.4	67.4
186.1	90.8	45.3
178.9	100.5	40.2
184.2	111.9	53.9
180.8	84.0	69.2
192.2	94.4	45.1

4.2.4 TiB₂/Al-4.5wt.%Cu Alloy

Fig. 4.4 shows microstructure taken by SEM in sample A-3. It shows that TiB₂/Al-4.5wt.%Cu matrix composite was successfully synthesized. The TiB₂ particles were formed from the K₂TiF₆ and KBF₄ salts reaction which is segregated in the inter-dendritic regions in the matrix.

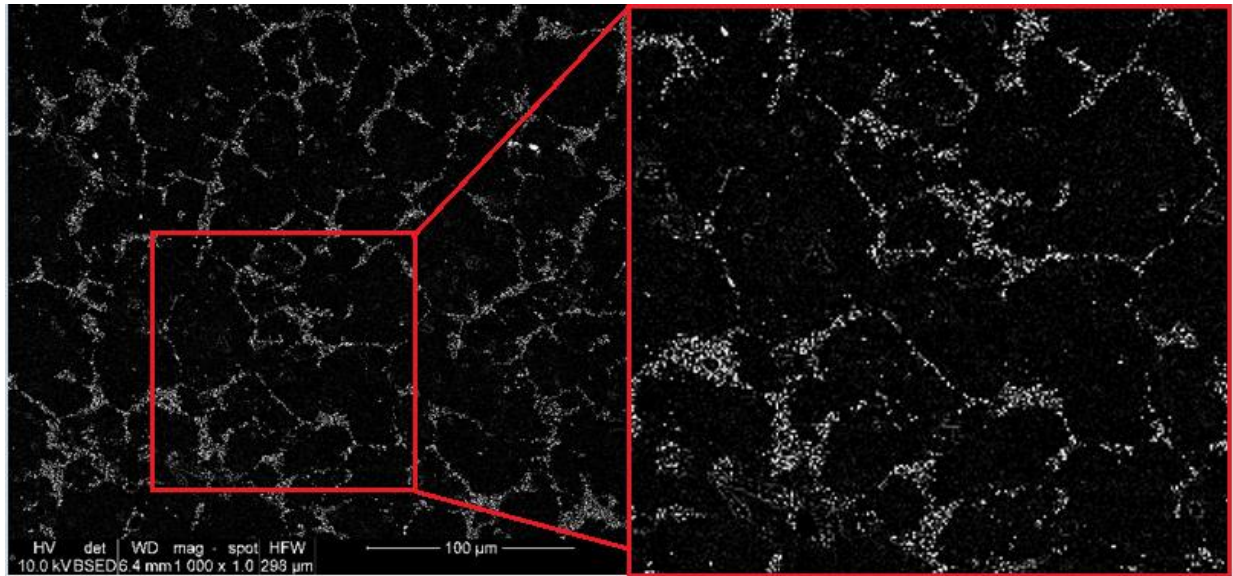


Figure 4.4 Distribution Condition of $\text{TiB}_2/\text{Al-4.5wt.\%Cu}$ Alloy of A-3

The diameter distribution of the TiB_2 particles measuring by ImageJ software that shown in Figure 4.5. The analysis result showed that the TiB_2 particles were in the micron range. The typical diameter of TiB_2 particles was smaller than $5\ \mu\text{m}$.

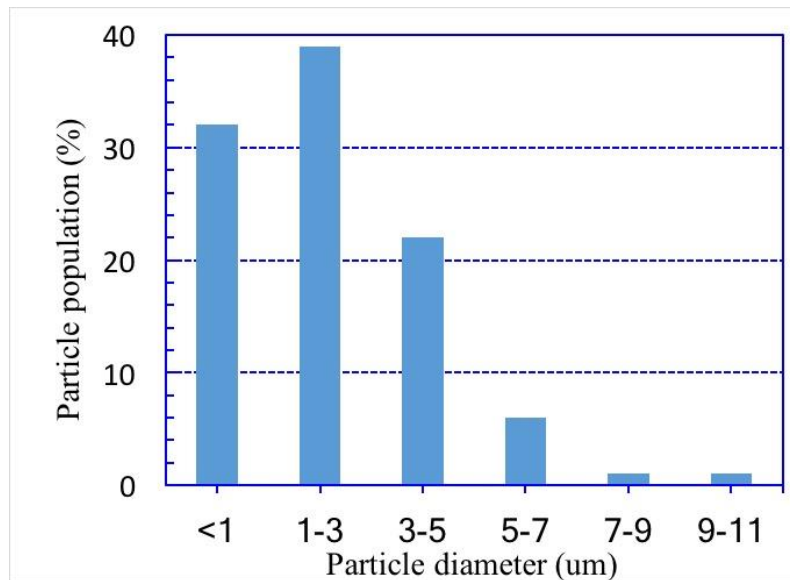


Figure 4.5 TiB_2 Particle Diameter Distribution in $\text{TiB}_2/\text{Al-4.5wt.\%Cu}$ Coupon

4.2.5 $\text{Al}_3\text{Ti}/\text{Al-4.5wt.\%Cu}$ alloy

A SEM image of the $\text{Al}_3\text{Ti}/\text{Al-4.5wt.\%Cu}$ alloy is illustrated in Figure 4.6

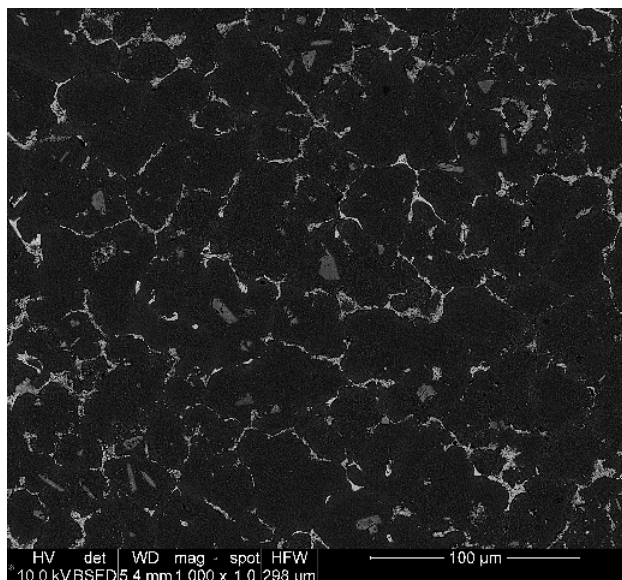


Figure 4.6 Particle Distribution in the $\text{Al}_3\text{Ti}/\text{Al-4.5wt.\%Cu}$ Alloy

SEM imaging shows that the Al_3Ti blocky particles could be found in the matrix. The diameter of the gray Al_3Ti particles was roughly $10\text{ }\mu\text{m}$, and they tended to randomly distributed in the Al-Cu matrix. Most Al_3Ti particles adopted a rod-like morphology, consistent with those typically observed for the microstructure of Al_3Ti particles in an Al matrix by in-situ preparation.

The resulting particle distribution, estimated using ImageJ software, is shown in Figure 4.7.

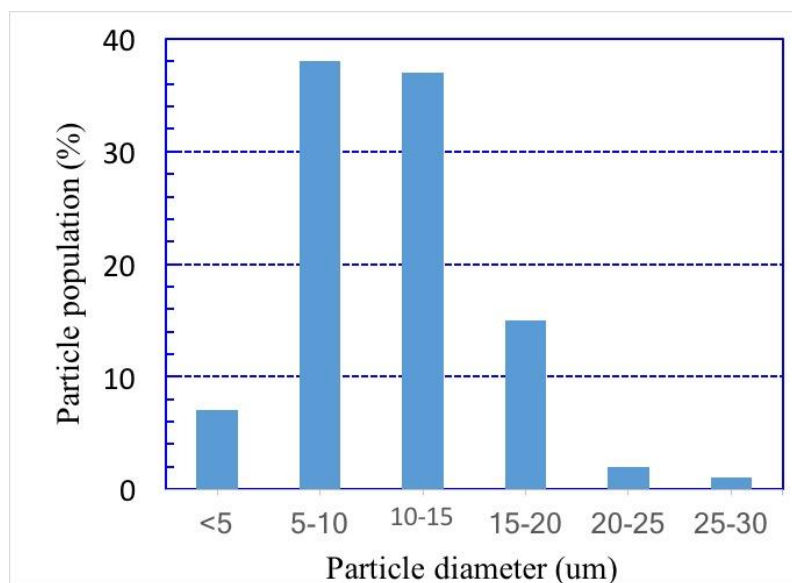


Figure 4.7 Particle Diameter Distribution in $\text{Al}_3\text{Ti}/\text{Al-4.5wt.\%Cu}$ Alloy

The range of Al_3Ti particles diameter was concentrated between 5 and 15 μm , and the largest particle size was about 30 μm .

4.2.6 Analysis and Aalculation

Metallographic images of the Al-4.5wt.%Cu alloy were taken by OM, as shown in Figure 4.8.

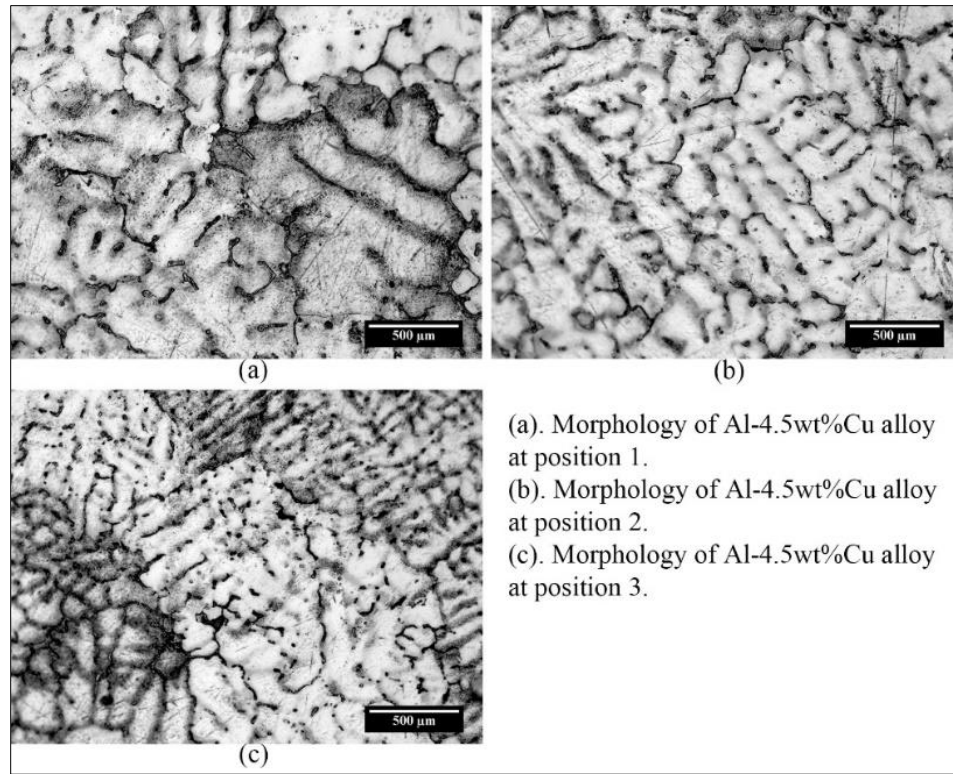


Figure 4.8 Morphology of Al-4.5wt.%Cu Alloy at Various Cooling Rates

As indicated in Figure 4.8, Figure a, b, and c correspond to the 1, 2, and 3 positions of a sample like the Al-4.5wt.%Cu alloy described in Figure 4.1. The spacing of dendrite arms from narrow to wide is clearly visible, corresponding to the different cooling rates, from fast to slow, respectively.

Table 4.3 presents the parameter and physical properties of Al-4.5wt.%Cu alloy used in calculation:

Table 4.3 Physical Properties of Al-4.5wt.%Cu Alloy and Calculation Parameters.

Property	Al-4.5wt.%Cu
Liquidus temperature, T_L	645°C
Solidus temperature, T_S	548°C

The SDAS of the Al-4.5wt.%Cu alloy in each position can be measured accurately. The local solidification time and the corresponding cooling rate can then be estimated using Eq. 4.3 and 4.4 (Flemings, 2006; Han, & Hunt, 1995; Wang, & Han, 2014).

$$d_2 = 9.83t_c^{0.38} \quad \text{Eq. 4.3}$$

$$q_s = (T_L - T_S)/t_c \quad \text{Eq. 4.4}$$

where t_c is the local solidification time, d_2 is the average SDAS, q_s is the average cooling rate, and T_L and T_S are the liquidus and the solidus temperatures, respectively. For the Al-4.5wt.%Cu alloy, $T_L = 645^\circ\text{C}$ and $T_S = 548^\circ\text{C}$. From Eq. 4.3 and Eq. 4.4, the average growth rate, v_D , of a secondary dendrite arm is estimated using the following: (Flemings, 2006):

$$v_D = d_2/t_c \quad \text{Eq. 4.5}$$

Data calculation using Eq. 4.3-4.5 are listed in Table. 4.3. The cooling conditions in the TiB₂/Al-4.5wt.%Cu and Al₃Ti/Al-4.5wt.%Cu alloy are identical to those in the Al-4.5wt.%Cu alloy, as they have the same latent heat. Therefore the average growth rates of three coupons at the same location are identical in that in the geometry Al-4.5wt%Cu coupon.

Table 4.4 Average Growth Rate in Al-4.5wt.%Cu with Different Cooling Conditions

Position	Avgas $d_2(\mu\text{m})$	$t_c(\text{s})$	$q_s(^{\circ}\text{C/s})$	$v_D(\mu\text{m/s})$
1	184.2	2235	0.044	0.082
2	110.3	580	0.167	0.190
3	56.1	97	1	0.578

According to Uhlmann's classical predictive model, the critical velocity V_C is a function of particle size (Uhlmann, 1964). According to Equation 2.22, the larger the average radius of the reinforcing particles (V_D), the smaller the corresponding V_C . The determine conditions for whether the particles are pushed out are as follows:

When $V_C > V_D$, particle should be pushed by solid-liquid interface.

When $V_C < V_D$, particle should be engulfed by solid-liquid interface.

The practical macroscopic distribution of the reinforcing particles in wedge-shaped casting can be observed by OM.

Figure 4.9 shows the particle distribution conditions in the $\text{TiB}_2/\text{Al-4.5wt.\%Cu}$ alloy at various cooling rates. Overall, the specimen showed equiaxed grains in all three positions, and the grain size of the structure differed depending on the cooling rate. The dark regions in images are the clusters of TiB_2 particles. During the growth stage of solidification, almost all of TiB_2 particles were rejected by the freezing front in different cooling conditions.

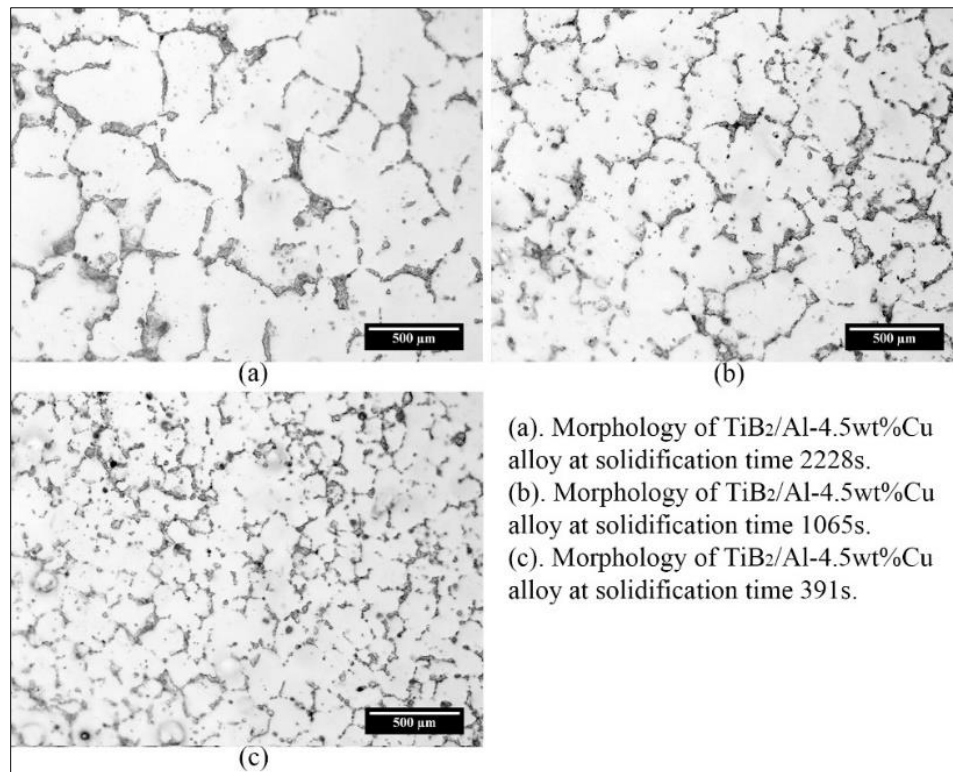


Figure 4.9 Morphology of $\text{TiB}_2/\text{Al-4.5wt.\%Cu}$ Alloy at Various Cooling Rates

The metallographic pictures of the $\text{Al}_3\text{Ti}/\text{Al-4.5wt.\%Cu}$ alloy at various cooling rates were taken from the OM, as shown in Figure 4.10. The large gray particles at the grain boundary are Al_3Ti , and the small dark particles are TiB_2 . Grain morphology was outlined by small TiB_2 particles. At

all cooling conditions, most of the particles were deposited at the grain boundaries except for a few Al_3Ti particles that appeared in the center of the grains.

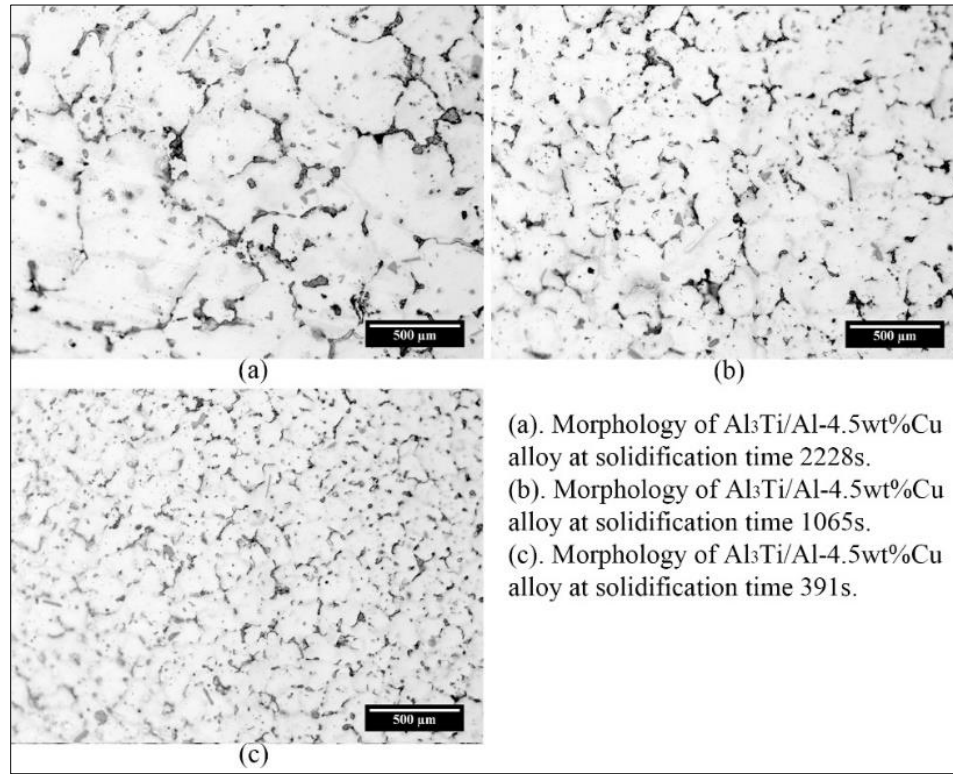


Figure 4.10 Morphology of $\text{Al}_3\text{Ti}/\text{Al-4.5wt\%Cu}$ Alloy at Various Cooling Rates

Following to the classic theory on particle pushing, the critical growth rate, v_c , under which a particle is pushed by a freezing front can be estimated by Eq. 2.22. The computational parameters are given by Table 4.5 (Oguchi, & Suzuki, 2007; Quaresma, Santos, & Garcia, 2000; Uhlmann, 1964).

Table 4.5 Physical Properties of Al-4.5wt.%Cu Alloy

Property	Note	Value
Boltzmann's constant	$k (J \cdot K^{-1})$	$1.38064852 \times 10^{-23}$
Diffusivity in the liquid region,	$D_L (m^2 \cdot s^{-1})$	3.5×10^{-9}
Latent heat	$L (J/kg)$	381900
Constant	n	2

The critical velocity for TiB_2 and Al_3Ti particles of various diameters in $\text{Al}_3\text{Ti}/\text{Al-4.5wt\%Cu}$ and $\text{TiB}_2/\text{Al-4.5wt\%Cu}$ coupons were estimated, and results are given in Table 4.6. The particle diameter ranges $0.5\mu\text{m}$ to $20\mu\text{m}$ and average growth rates during solidification ranges from

0.082 μm to 0.578 μm . The experimental results indicate that the most of TiB₂ and Al₃Ti particles that did not serve as nuclei were rejected by advancing under different cooling conditions. The critical growth rates for Al₃Ti particles were 0.19, 0.011, and 0.006 $\mu\text{m/s}$, corresponding to particle diameters of 10, 15, and 20 μm , respectively.

Table 4.6 Critical Growth Rates for Particles of Different Sizes

Particle type	TiB ₂				Al ₃ Ti		
Particle diameter (μm)	0.5	1	3	5	10	15	20
Critical velocity ($\mu\text{m/s}$) ($V_c = 2(n+1) \frac{La_0 v_0 D}{kTd^2}$)	94.68	23.64	2.63	0.95	0.19	0.011	0.006
Growth rate ($\mu\text{m/s}$)	0.082-0.578						
Predictive results Engulfed/pushed	P	P	P	P	E	E	E
Observe results	P	P	P	P	P	P	P

4.3 Results of MSR Experiment

4.3.1 Particle Pushing Analysis

It is assumed that all of the reinforcing particles are perfectly spherical in the system, and the nucleation process maintains a constant growth rate from the beginning to the end during solidification. According to the calculation results listed in Table 4.6, the critical velocity of the particles is inverse to the particle size as shown in Figure 4.11.

Three dashed lines are corresponding to three average growth rates for the wedge-shaped casting. According to Uhlmann's classical prediction model, as Figure 4.11 illustrated, the fastest growth rate of any coupon in the experiment was 0.578 $\mu\text{m/s}$, which exceeded the critical growth rate of those particles with diameters equal to or greater than 10 μm . Under this condition, the Al₃Ti particles should be engulfed by growing dendrites during solidification, according to the predictive model based on surface free energy.

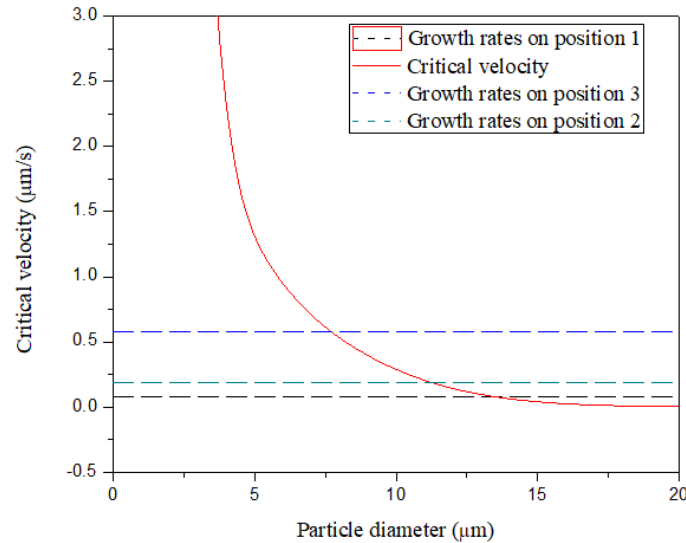


Figure 4.11 Critical Velocity versus Particle Diameter
in Wedge-shaped Casting for Al-4.5wt.%Cu Alloy

In the $\text{Al}_3\text{Ti}/\text{Al-4.5wt.\%Cu}$ alloy, the small number of large Al_3Ti particles as the nuclei of grains in the matrix can be found in the centers of grains. According to the classic theory, during solidification, reinforcing particles should be engulfed when the growth rate exceeds the critical growth rate. However, the result of the experiment is inconsistent with the prediction based on the thermodynamic model.

The movement of reinforced particles in a molten metal melt during solidification is affected by many factors. The observation results of the verification experiment are inconsistent with the prediction based on the surface free energy model, indicating that the classic particle pushing theory is not correct.

Solidification is a dynamic process; therefore, particle behavior can result from a variety of effects, such as fluid flow and dynamic changes in temperature. Using a simple model to predict the behavior of particles near the interface requires consideration of the effects of multiple factors. The realistic model for predicting particle pushing in an alloys should considerate solute diffusion and fluid flow in the liquid. The latter is always accompanied by solidification process

in the liquid, and the source of the fluid flow comes partly from volume changes and temperature changes during solidification.

Now, consider a particle is pushed by a planar solidification front in an alloy under steady-state conditions. The particle and the growing solid-liquid interface will have to maintain a dynamic equilibrium. Under such a condition, the liquid is flow into the gaps between the growing solids and the particles, as shown in Figure 4.12. The solute in the alloy diffuses against the physical fluid flow at a certain rates that are sufficient to prevent the buildup of solute in the gap between the particles and growing solids. This equilibrium of such a dynamic system result in particle pushing. (Sasikumar, Ramamohan, & Pai, 1989).

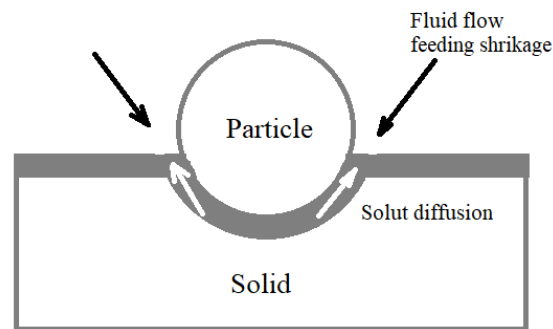


Figure 4.12 Equilibrium Between the Particle and Solids

4.3.2 Diffusion Convection Model

When the liquid phase keeps changing into a solid phase, fluid flow exists in the liquid during the practical solidification process (Han, & Hunt, 1996). Most of the current models are based on the balance of the surface free energy. However, the theory doesn't account for fluid flow in the gap between the particle and the growing solid thus cannot accurately predict whether the particles are pushed or engulfed by the solidifying front.

As mentioned earlier, when a particle is rejected by the interface, the particle and the freezing front remain in a dynamic equilibrium state. Therefore, it is possible to establish a diffusion-convection equilibrium equation between the solute diffusion and physical fluid flow.

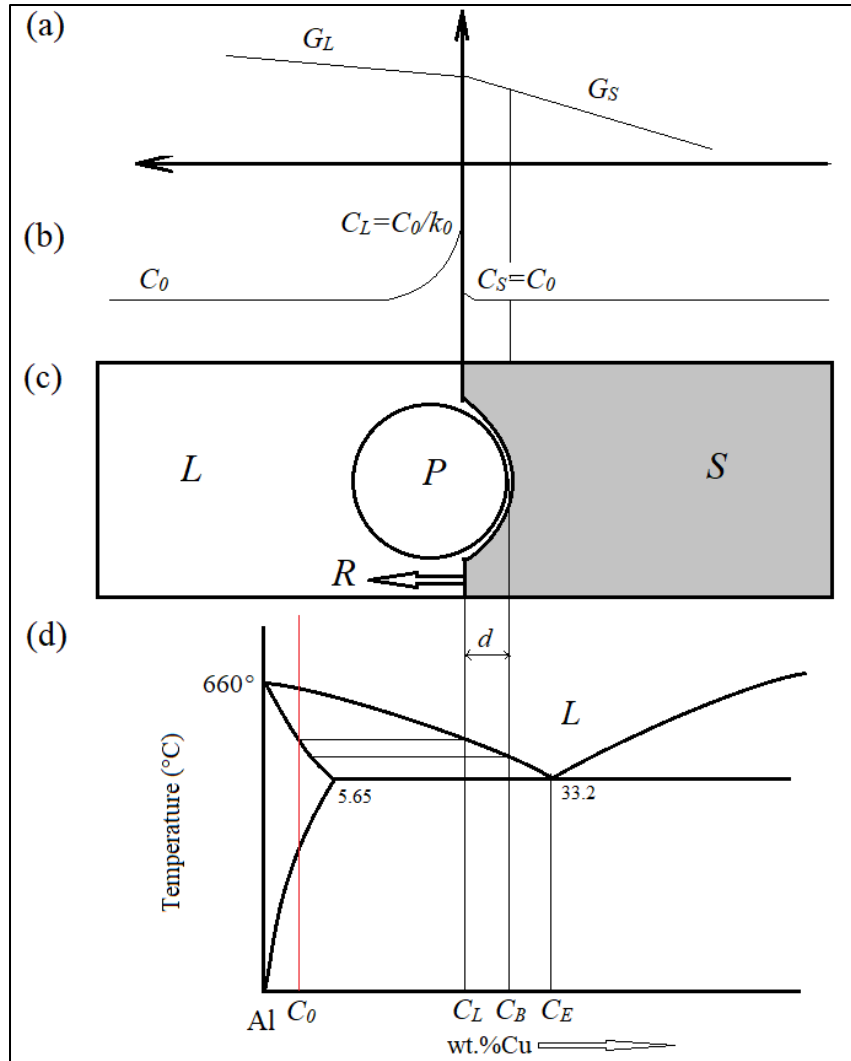


Figure 4.13 Sketch Diagram of Particle Pushing Process.

Assuming there is a perfect spherical particulate rest in the molten Al, and it is approached by a flat moving solid-liquid interface during solidification. The particle remains in rest in the melt until it contact with the moving interface. Figure 4.13 illustrated a steady state between the particle and the interface. In Figure 4.13(c), the interface growing toward to the liquid at a certain rate R . Van der Waals force between the particle and the solid-liquid interface is the driving force to push the particle away from the freezing front when the distance between the particle and the solid-liquid interface is close enough. There is a gap between the particle and the interface, where d in Figure 4.13 indicated the depth that the particle embedded the interface, which can be determined by Solid temperature gradients, G_S , illustrated in Figure 4.13(a). As

mentioned before, in steady-state, the solute of the liquid continuously diffuses outward from the bottom of the gap due to the concentration gradients. In the contrast, for the molten metal, the density of the liquid is less than that of the solid state, which causes volume shrinkage when the melt transfers to a solid. Therefore, when the freezing front comes into contact with the particle, the solution around the particle continues to solidify, which makes the solid–liquid interface form a pit in the inward direction at the position in contact with the particle depicted in Figure 4.13(c). The volume shrinkage caused the liquid flow into the gap to offset the solute diffusion, which satisfying the equilibrium condition of the diffusion-convection equation. Corresponding to the phase diagram of the Al-Cu binary alloy depicted in Figure 4.13(d), when the Al-4.5wt.%Cu alloy is solidified, The solute concentration of the liquid located in the interface and the bottom of gap are C_L and C_B respectively. Where C_0 and C_E correspond to the original concentration and the eutectic concentration of Al-4.5wt.%Cu alloy, respectively. In steady-state, $C_L = C_0/k_0$, where the partition coefficient of solute, k_0 , is smaller than one in an Al-Cu alloy system illustrated in Figure 4.13(b). To simplify the model, it is assumed that the concentration gradient in the solid phase is negligible.

As mentioned before, the bottom solute must continue to diffuse outward of the gap. Simultaneously, the liquid flows into the gap to offset the volume shrinkage. Assuming that the diffusion rate is insufficient to balance the fluid flow into the gap, the liquid phase in the gap transforms into a solid phase due to solute accumulation, then the particle is engulfed by the solid–liquid interface, which is illustrated in Figure 4.14.

Therefore, when particle pushing occurs, the steady-state is maintained between the particles and the advancing freezing front. The convection and diffusion are balanced. With an equilibrium equation, the volume shrinkage due to solidification in the gap will be a function of the growth rate. By substituting the diffusion-convection equation, the relationship between the growth rate and the particle diameter will be investigated. Hence a steady-state condition for particle pushing is obtained.

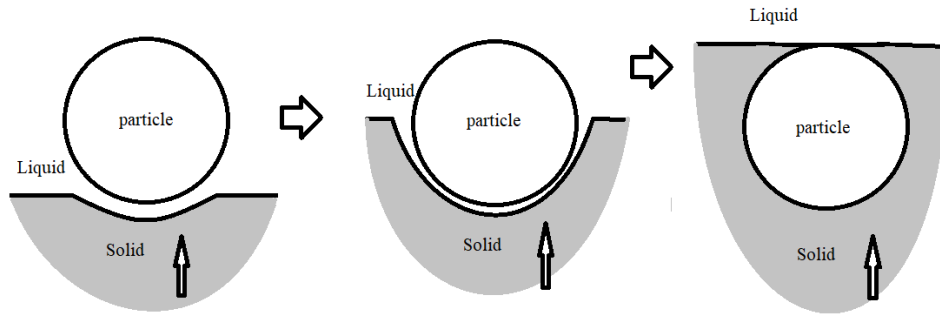


Figure 4.14 Schematic Illustration of Engulfment

4.3.3 TiB₂/Al-4.5wt.% Cu-MMCs in Diffusion Convection Model

The parameters required in the calculation process are list in the Table 4.7:

Table 4.7 Parameters Required in the Calculation

Property	Note	Value
Solute diffusivity	$D_L (m^2 \cdot s^{-1})$	3.5×10^{-9}
Solidus slope	m_L	-2.6
Partition coefficient	k_0	0.17
Colute composition	$C_0 (wt. \%)$	0.045
Temperature gradient	G_S	$50^\circ/\text{cm}$
Density of liquid phase	ρ_L	2610 kg/m^3
Density of solid phase	ρ_S	2450 kg/m^3

A general convection diffusion equation as shown in Eq. 4.6.

$$\frac{\partial c}{\partial t} = \nabla \cdot (D \nabla c) - \nabla \cdot (\vec{v} c) + A \quad \text{Eq. 4.6}$$

where c is the concentration of the solute, D is the diffusion coefficient, and \vec{v} is the velocity of the fluid flow $\vec{v} = f(\text{time, location})$. A commonly means “sources” or “sinks” of the quantity c .

∇ represents the gradient, $\nabla \cdot$ represents divergence, and ∇c represents the concentration gradient.

There are no sources or sinks in this case, and the velocity field describes an incompressible flow that has zero divergence. The formula then simplifies to the following:

$$\frac{\partial c}{\partial t} = D_L \nabla^2 c - \vec{v} \cdot \nabla c \quad \text{Eq. 4.7}$$

Assuming the diffusivity D is a constant, the net diffusion is proportional to the Laplacian (or second derivative) of the concentration.

When the particles and the interface maintain a steady state moving along the solidification direction, the diffusion flux per unit time in dynamic equilibrium with the liquid flow in the gap, then Eq. 4.6 is converted to the following:

$$D_L \nabla c - \vec{v} c = 0 \quad \text{Eq. 4.8}$$

According to Fick's second law, the first term on the left side of Eq. 4.8 should be the concentration gradient in the gap. Consider the limit conditions for maintaining steady-state, assuming the concentration of the solute at the gap bottom is C_E and the concentration at the solid-liquid interface is C_L , according to Fick's second law, by substituting C_L and C_E into the first term of Eq. 4.6, the equation can be converted to the following:

$$D_L \nabla c = D_L \frac{C_E - C_L}{a\theta} \quad \text{Eq. 4.9}$$

where a is the radius of the particle, and θ is a angle between the outlet of the gap and the bottom of the particle which illustrated in Figure 4.15

The second term on the left side of Eq. 4.8 indicates the fluid flow between the particle and the grain gap. Assuming a flat solidification front migrates toward a spherical particle, when the particle keeps being pushed out by the interface during the solidification process, the shape of the contact area between the particle and the solid-liquid interface is like a crown, as shown in Figure 4.15.

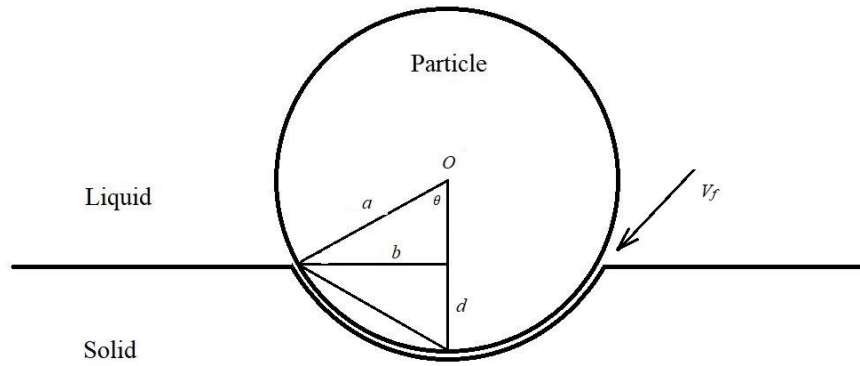


Figure 4.15 Schematic of Contact Area between Freezing Front and Particle.

When the liquid in the gap solidifies into a solid, the volume reduction occurs according to mass conservation. At a given growth rates, the shrinkage volume in the gap in steady-state is ΔV_S which could be expressed by Eq. 4.8 as follow:

$$\Delta V_S = S_C R \left(1 - \frac{\rho_S}{\rho_L}\right) \quad \text{Eq.4.10}$$

where S_C is the shadow area of the crown; R is the growth rates of the solid-liquid interface; ρ_S and ρ_L indicate the density of liquid and solid before and after solidification, respectively.

According to the crown area calculation equation, the area of the contact surface, S_C is given by Eq. 4.11

$$S_C = \pi b^2 \quad \text{Eq. 4.11}$$

where b is the radius of the gap outlet, d is the height of the crown, and θ is the angle between the bottom and the outlet of the gap as illustrated in Figure 4.15.

Therefore, the volume change during solid–liquid transition can be obtained as Eq. 4.12.

$$\Delta V_S = \pi b^2 R \left(1 - \frac{\rho_L}{\rho_S}\right) \quad \text{Eq. 4.12}$$

where $b = \sqrt{a^2 - (a - d)^2} = \sqrt{2ad - d^2}$

Substituting Eq. 4.12 and Eq. 4.9 into Eq. 4.8 respectively, Eq. 4.13 can be obtained as follow:

$$D_L \frac{C_E - C_L}{a\theta} = \pi b^2 R \left(1 - \frac{\rho_L}{\rho_S}\right) C_L \quad \text{Eq. 4.13}$$

where: $C_L = C_0/k_0$

The left side of Equation 4.13 is diffusion term, and the right side is the flow term. After simplification, to maintain the particle pushing, the diffusion of solute should be greater than or equal to the influx of liquid, therefore the Eq. 4.14 is obtained as follow:

$$\begin{aligned} D_L \frac{C_E - C_0/k_0}{a\theta} &\geq \pi b^2 R \left(1 - \frac{\rho_S}{\rho_L}\right) C_0/k_0 \\ \xrightarrow{\text{yields}} R &\leq \frac{\rho_L D_L (C_E - C_0/k_0)}{(\rho_L - \rho_S) a \theta \pi b^2 C_0/k_0} \\ \xrightarrow{\text{yields}} R &\leq \frac{\rho_L D_L (k_0 C_E - C_0)}{(\rho_L - \rho_S) a \theta \pi b^2} \end{aligned} \quad \text{Eq. 4.14}$$

By substituting $b = \sqrt{2ad - d^2}$ into Eq. 4.14, the Eq 4.15 is yield as follow:

$$R \leq \frac{\rho_L D_L (k_0 C_E - C_0)}{(\rho_L - \rho_S) a \theta \pi (2ad - d^2)} \quad \text{Eq. 4.15}$$

Eq. 4.15 is a general expression of diffusion-convection model, which indicated the critical velocity, R , is a function of the particle diameter, a , when the particle and the interface are in a steady state.

In order to maintain the steady state between the particles and the interface, the growth rate during solidification should be at least less than the maximum critical velocity corresponding to the different particle sizes in Eq. 4.15. However, θ variable in the equation is still undetermined. Depending on the value of θ , the equation will evolve into three different forms, corresponding to three different states of the particle and the interface illustrated in Figure 4.16.

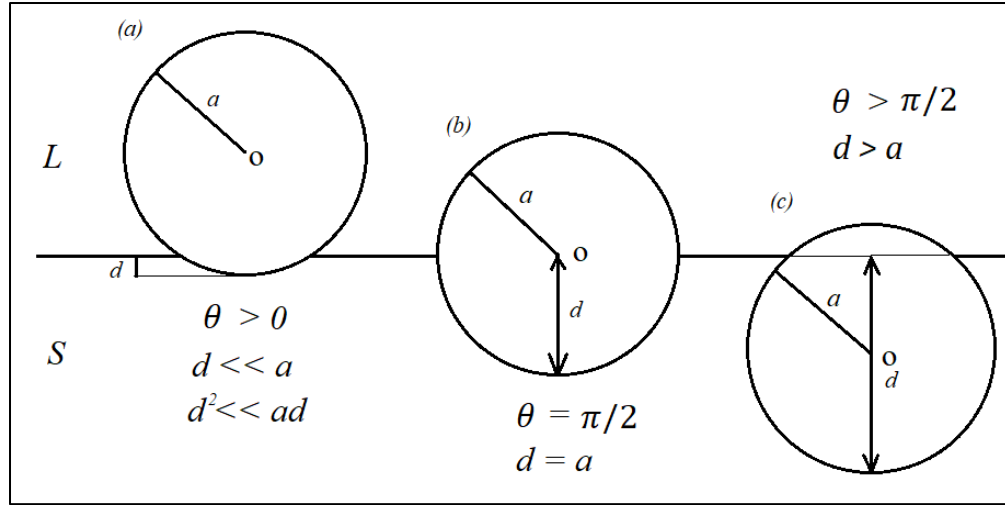


Figure 4.16 Three Possible State Between Particle and the Interface

First, according to Figure 4.16(a), considering $\theta > 0$ and $d \ll a$ therefore $d^2 \ll ad$. d can be determined by solid temperature gradients as Eq. 4.16:

$$d = -\frac{m_L(C_E - C_0/k_0)}{G_S} \quad \text{Eq. 4.16}$$

where m_L is solidus slope of solid temperature gradients listed in table 4.7.

by substituting Eq. 4.16 into Eq. 4.15, the Eq. 4.17 can be obtained as follow:

$$R \leq \frac{\rho_L D_L k_0 G_S}{(\rho_L - \rho_S) 2a^2 \theta \pi m_L C_0} \quad \text{Eq. 4.17}$$

By using Taylor expansion: when $\theta \rightarrow 0$; let $f(\theta) = \sin\theta$;

$$\sum_{k=0}^{\infty} \frac{f^{(k)}(0)}{k!} (x-0)^k = x + \frac{f'(x)}{1!} x + \frac{f''(x)}{2!} + \dots$$

$$\xrightarrow{\text{yields}} f(x) = f(0) - \frac{f'(0)}{1!} \theta + \frac{f''(0)}{2!} + \dots$$

$$\xrightarrow{\text{yields}} \sin \theta = 0 + \frac{\cos \theta}{1} \theta = \theta$$

$$\therefore \theta = \sin\theta = \frac{b}{a} = \frac{\sqrt{2ad-d^2}}{a} \approx \sqrt{\frac{2d}{a}} \quad \text{Eq. 4.18}$$

Then Eq. 4.17 can be converted into Eq. 4.19 as follow:

$$R \leq \frac{\rho_L D_L k_0 G_S}{(\rho_L - \rho_S) \sqrt{2ad} 2\pi m_L C_0} \quad \text{Eq. 4.19}$$

For the second condition, considering an extreme condition that $\theta = \frac{\pi}{2}$, and $a = d$. The Eq. 4.15 is converted into Eq. 4.19 as follow:

$$R \leq \frac{2\rho_L D_L k_0 G_S}{(\rho_L - \rho_S) a \pi^2 d^2 C_0} \quad \text{Eq. 4.20}$$

Finally, $\theta > 90^\circ$ is considered as illustrated in Figure 4.16. However, the particle will be engulfed by solid-liquid interface due to $a < d$. Therefore it is impossible to maintain steady-state between the particle and the interface.

Substituting the parameters of the Al-4.5wt.%Cu alloy listed in Table 4.8 into the Eq. 4.19 and Eq. 4.20, the critical growth rate based on diffusion-convection model under different size particles can be calculated as shown in Table 4.8:

Table 4.8 Critical Velocity Corresponding to Particle Size

Particle diameter (μm)	Critical velocity based on diffusion-convection model (μm/s)		Critical velocity based on classic predictive model (μm/s)	Average growth rate of wedged-shaped sample for Al-4.5wt.%Cu alloy
	$\theta = \frac{\pi}{2}$, and $a = d$	$\theta > 0$ and $d \ll a$		
0.5	0.3574x10 ⁻⁴	0.0223	80.10	0.082-0.578 μm/s
1	0.1782x10 ⁻⁴	0.0079	20.23	
3	0.0606x10 ⁻⁴	0.0015	3.55	
5	0.0361x10 ⁻⁴	0.0007	0.82	
10	0.0179x10 ⁻⁴	0.0002	0.21	
15	0.0119x10 ⁻⁴	0.0001	0.12	

As listed in table 4.8, after including the fluid flow caused by volume shrinkage, the diffusion-convection model can be used to calculate the critical velocity under two conditions. Compared with the results of the classic model, the critical velocity from the new model is several orders of magnitude smaller. Under the extreme condition of $\theta = \pi/2$, the critical velocity required to maintain particle pushing reaches the lowest value. The value of critical velocity ranges from 0.3574×10^{-4} to $0.0119 \times 10^{-4} \mu\text{m/s}$, corresponding to particle sizes from 0.5 to $15 \mu\text{m}$. With the condition $\rightarrow 0$, The critical velocity ranges from 0.0223 to $0.0001 \mu\text{m/s}$ corresponding to particle diameters from 0.5 to $15 \mu\text{m}$.

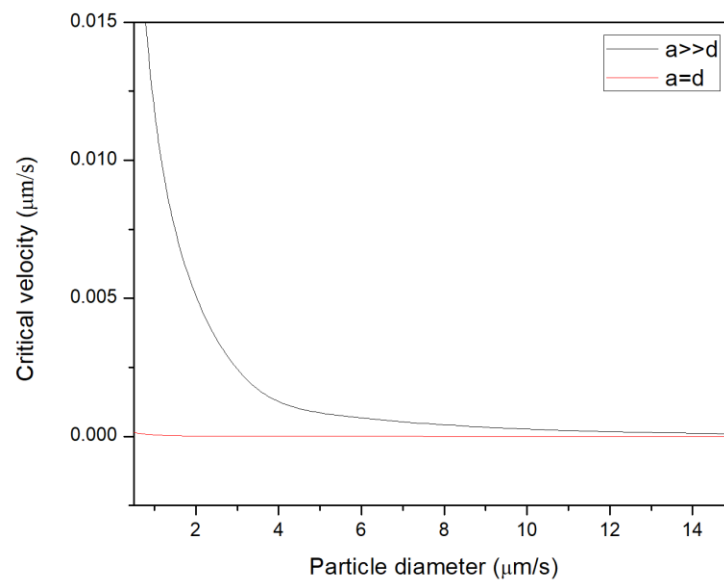


Figure 4.17 Critical Velocity versus Particle Diameter
Based on Diffusion-convection Model

Figure 4.17 illustrated the various critical velocity with different particle size. As the particle size increases, the critical velocity result from diffusion-convection model under two conditions is approach to 0.

Following the classical predictive model criterion, the particles will be engulfed by the freezing front when the growth rate is greater than the critical velocity. Following Table 4.8, the steady-state critical speed calculated from the diffusion-convection model is much smaller than the

growth rate, which is difficult to achieve in practical situations. However the observations indicate that almost all particles are pushed by the interface. This results suggested that it is difficult for classic prediction model to determine the particle pushing condition based on surface free energy criterion.

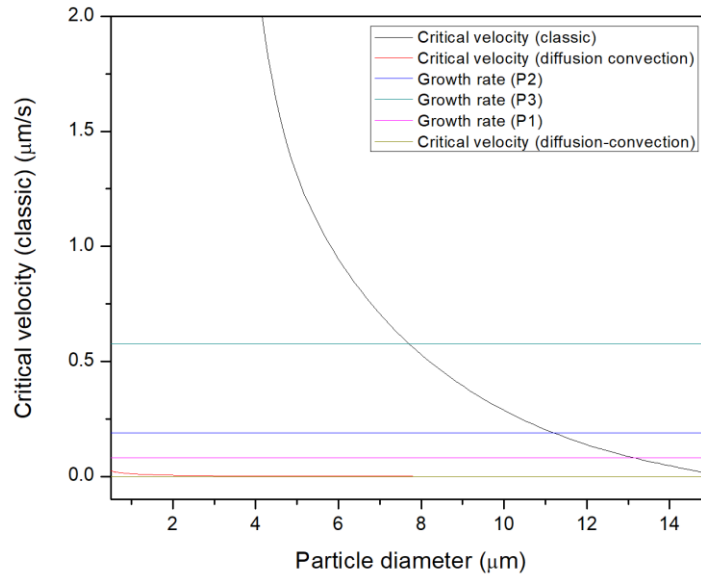


Figure 4.18 Critical Velocity Prediction Comparison

Figure 4.18 depicted the results comparison between the classic predictive model and the diffusion-convection model. The three average growth rate is larger than the critical velocity result from classic model when particle size larger than 8-14 μm . In the contrast, the diffusion-convection prediction under two conditions are both much smaller than the average growth rates at all particle diameter. This results further indicated that both TiB_2 and Al_3Ti particles should be engulfed by moving solid-liquid front at any particle size due to the kinetic and thermodynamic engulfment criteria based on surface free energy are met.

4.3.4 Temperature Gradients Effect

When the particle size is given, the critical velocity of the particles according to the diffusion-convection model is proportional to the temperature gradient. Since the temperature gradient is a fabrication process variable, the relationship between the temperature gradient and the critical velocity is worth to investigate, especially to industrial production area.

Table 4.9 Critical Velocity Corresponding to Different Temperature Gradient ($\theta = \frac{\pi}{2}$)

Temperature gradient (°C/cm)	Critical velocity based on diffusion-convection model($\mu\text{m/s}$)		
	$\theta = \frac{\pi}{2}, a = d$		
	Particle diameter (1 μm)	Particle diameter (5 μm)	Particle diameter (10 μm)
10	0.3573×10^{-5}	0.0715×10^{-5}	0.3573×10^{-6}
20	0.7147×10^{-5}	0.1429×10^{-5}	0.7147×10^{-6}
30	1.0721×10^{-5}	0.2144×10^{-5}	1.0721×10^{-6}
40	1.4294×10^{-5}	0.2859×10^{-5}	1.4294×10^{-6}
50	1.7867×10^{-5}	0.3574×10^{-5}	1.7867×10^{-6}
60	2.1441×10^{-5}	0.4288×10^{-5}	2.1441×10^{-6}

With $\theta = \frac{\pi}{2}$, it can be seen from Table 4.9 that the critical velocity increases as the increase of temperature gradient and inversely proportional to the particle size. This trend is consistent with classic predictive models.

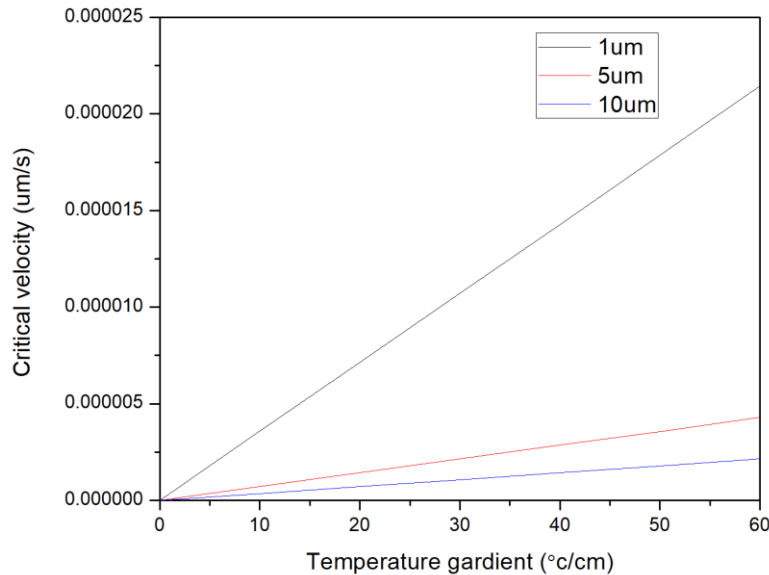
Figure 4.19 Critical Velocity versus Temperature Gradient ($\theta = \frac{\pi}{2}$)

Figure 4.19 illustrated that the critical velocity are linearly related to the temperature gradient when $\theta = \frac{\pi}{2}$. The largest slope occurs on the 1 μm diameter particle. As the particle size increases

to 5 μm and 10 μm , the corresponding critical velocity is relatively insignificant with changes in temperature gradient.

Table 4.10 Critical Velocity Corresponding to Different Temperature Gradient ($\theta \rightarrow 0$)

Temperature gradient ($^{\circ}\text{C}/\text{cm}$)	Critical velocity based on diffusion-convection model($\mu\text{m}/\text{s}$)		
	$\theta \rightarrow 0, a \gg d$		
	Particle diameter (1 μm)	Particle diameter (5 μm)	Particle diameter (10 μm)
10	0.0016	1.34×10^{-4}	0.50×10^{-4}
20	0.0032	2.67×10^{-4}	0.99×10^{-4}
30	0.0047	4.01×10^{-4}	1.50×10^{-4}
40	0.0063	5.35×10^{-4}	1.99×10^{-4}
50	0.0079	6.68×10^{-4}	2.49×10^{-4}
60	0.0095	8.02×10^{-4}	2.99×10^{-4}

Following Figure 4.10 expressed, with $\theta \rightarrow 0$, the tendency of critical velocity changes with temperature gradient is same as when $= \frac{\pi}{2}$. Figure 4.20 indicated the critical velocity of 1 μm

diameter particles is significantly higher than that of 5 μm and 10 μm diameter particles.

Theoretically, particle pushing is more difficult as the particle size shrinks.

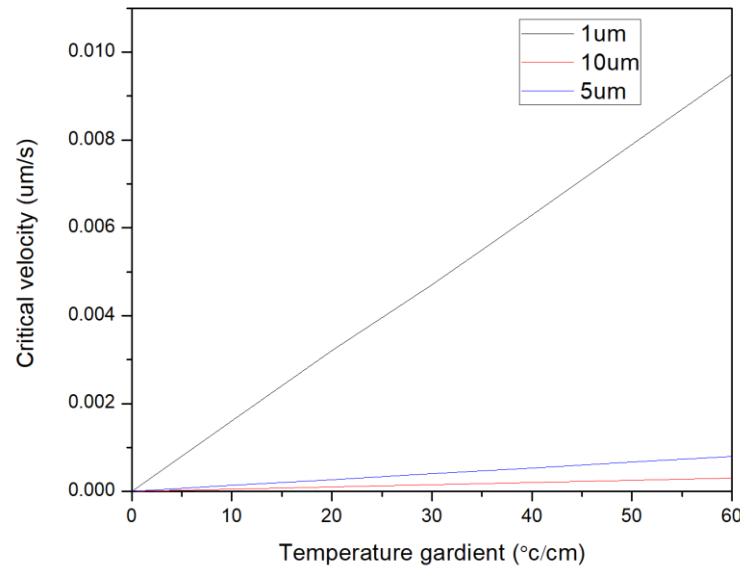


Figure 4.20 Critical Velocity versus Temperature Gradient ($\theta \rightarrow 0$)

With the establishment of the new diffusion-convection model, the unconsidered fluid flow factor in the classical model are also involved. However, the results indicate that the actual critical velocity at a given particle size is much smaller than that of the classical prediction model. It is fundamentally proved that the particle pushing criterion based on surface free energy is difficult to predict the behavior of tiny particles in the melt.

Solidification is a complex process in which liquid flow is always present in the melt during redistribution process, which may be caused by temperature various at different locations or disturbances. In addition, in the actual case, the particles are also affected by the relative position to the interface, and when the relative position of the particles to the growing secondary dendrite arm is not stable, the particles are hard to be caught by the solid-liquid interface.

4.4 Results of Stirring Experiment

4.4.1 Influence of High Energy Ball Milling on Nano-TiB₂ Particles

The wettability of nanoparticles is poor. Therefore, it is difficult to add nano-reinforcing particles directly to the molten Al melt using an external addition method. Therefore, this study introduced HEBM technology to uniformly mix nano-TiB₂ particles and K₂ZrF₆ salts to increase the wettability of the particles. The experiment used an HEBM with an unrivaled speed of 1000 rpm and a fan for cooling. In order to prevent oxidation caused by overheating, ball milling was stopped for 5 minutes per 15 minutes mixing. Fig. 4.15 are SEM images illustrating a comparison of the particle size with different mixing methods.

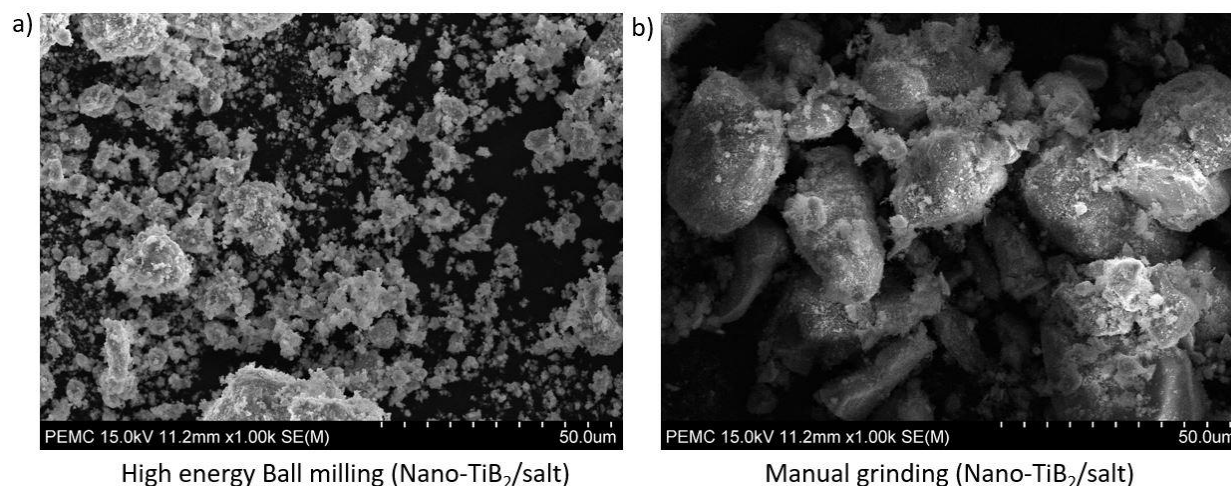


Figure 4.21 Comparison Diagram
Nano-TiB₂/salt with/without HEBM (1000x)

Figure 4.21a shows the mixing effect of TiB₂ particles and salt after 6 h of HEBM treatment, and Figure 5.15b shows the mixing effect of 6 h of manual grinding. Obviously, after HEBM treatment, the K₂ZrF₆ salt particles in the mixed powder are broken into small pieces. The average particle size is about 1–10 μm. In contrast, even after 6 h, the salt particles mixed by hand grinding remain relatively intact, no obvious cracking is observed, and the average particle diameter is about 40 μm.

Figure 4.22 illustrates the same mixed TiB₂/ K₂ZrF₆ powder, zoomed in 50,000x. The nano-TiB₂ particles can be clearly observed. Figure 4.16b shows the state of the TiB₂ particles after manual grinding. It can be seen that the nano-TiB₂ particles are still in agglomeration and are not well mixed with the salt. Most of the nano-TiB₂ particles have an irregular shape and are adsorbed on the surface of the large salt particles. Although the reinforcing particles are mixed with the salt particles after manual grinding, the wettability is obviously inferior to that produced with HEBM.

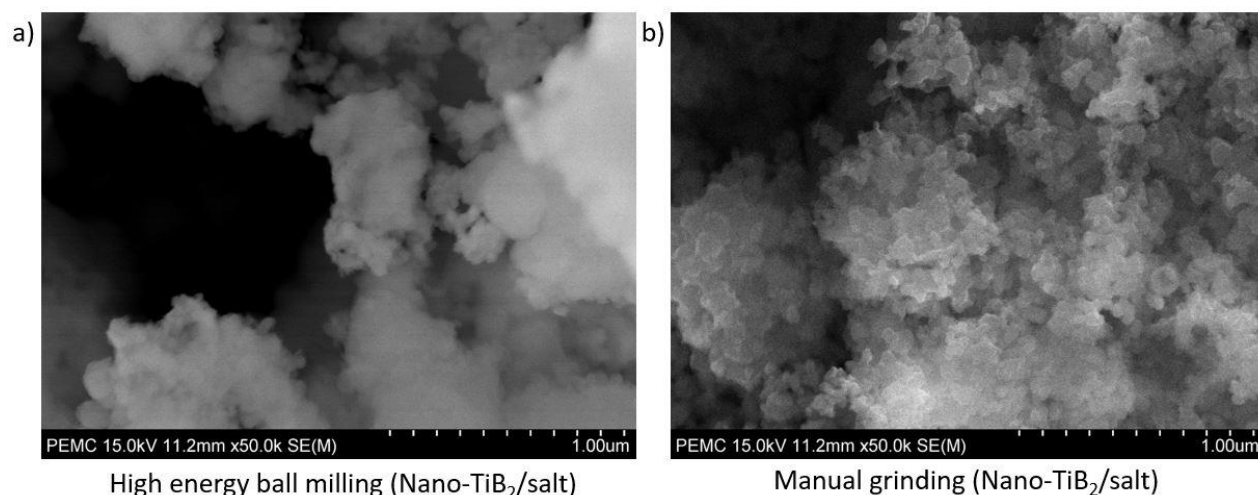


Figure 4.22 Comparison Diagram
Nano-TiB₂/K₂ZrF₆ with/without HEBM (50000x)

In contrast, although the nano-TiB₂ particles in Figure 4.22a show agglomeration, most of the nanoparticles are covered by a layer of floc. It is presumed that the K₂ZrF₆ salt particles with lower hardness collide with the nanoparticles during ball milling. Due to the high hardness of the TiB₂ particles, the salt particles gradually encapsulate the TiB₂ particles during the ball milling process to form the flocs to encapsulate the nanoparticles. This greatly enhances the wettability of the particles, making it easier for TiB₂ particles to be added to the molten Al liquid, reducing waste and improving production efficiency.

4.4.2 Original Sample Morphology Analysis

Figure 4.23 is a SEM photograph of the microstructure of the nano-TiB₂/Al-MMCs sample. Figure 4.23a shows TiB₂ particle distribution in the O-5 coupon prepared without using HIU. With only mechanical stirring, the TiB₂ particles in the matrix are unevenly distributed and large clusters of particle. An analysis using ImageJ software showed that the average equivalent diameter of TiB₂ particle clusters is about 300 μm . Figure 4.23b shows a SEM photograph of the microstructure of the nano-TiB₂/Al-MMCs sample (i.e., the sample assisted by HIU in the preparation process).

Although a slight agglomeration phenomenon of nano-TiB₂ particles still occurs, there are no large particle clusters in the matrix (i.e., the reinforcements are uniformly dispersed in the Al-

matrix). The fragmentation of bulk particle clusters is mainly attributed to the agitation dispersion produced by HIU in the melt. Typically, significant agglomeration is a result of small clusters loosely connected together. Under HIU agitation, the high-frequency shear forces in the melt can break up large agglomerations from the weak points of the joint. Therefore, after 10 minutes of HIU treatment during the fabrication process, the large cluster in the matrix substantially disappeared. It should be noted that it is difficult to separate individual nano-TiB₂ particles from agglomerations by the HIU technique. Most of the reinforced particles are still distributed in the matrix in the form of small clusters.

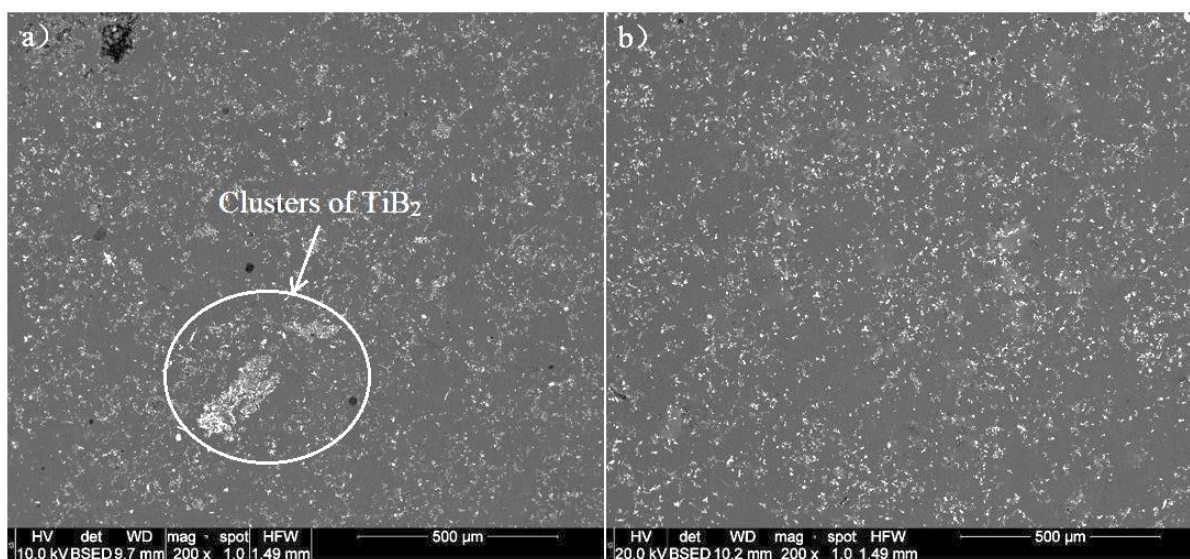


Figure 4.23 Microstructure of O-5 Sample.

(a) Nano-TiB₂/Al-MMCs without HIU, (b) Nano-TiB₂/Al with HIU

Although it has been reported that when HIU acts on a liquid, a capillary phenomenon is produced by the high-pressure effect due to cavitation, which causes the melt to easily penetrate into the gap of agglomerated particles to separate the individual particles. However, the effect of the high pressure is limited when the reinforcing particle is nanometer size.

The typical microstructure of the O-5 sample is presented in Figure 4.24. Overall, two types of reinforcements with different morphologies were found in the Al matrix: rod-like Al₃Zr reinforcements and nano-TiB₂ particles that were successfully added. The K₂ZrF₆ flux played a beneficial role in the wetting of TiB₂ nanoparticles with Al as the mixed TiB₂/K₂ZrF₆ was added

to the molten Al melt. The salt decomposed at around 600°C, releasing the Zr element through an exothermic chemical reaction, the equation for which is as follows:



According to reports, the reaction product of K_2ZrF_6 can effectively remove the oxide layer on TiB_2 particles and improve the wetting between the ceramic particles and the Al matrix. Figure 4.18b illustrates that the nano- TiB_2 particles existed in the Al matrix as clusters outlining the grain boundaries of the alloy. Quantitative analysis using ImageJ software showed average equivalent agglomeration radius of the clusters of particles was 8 μm .

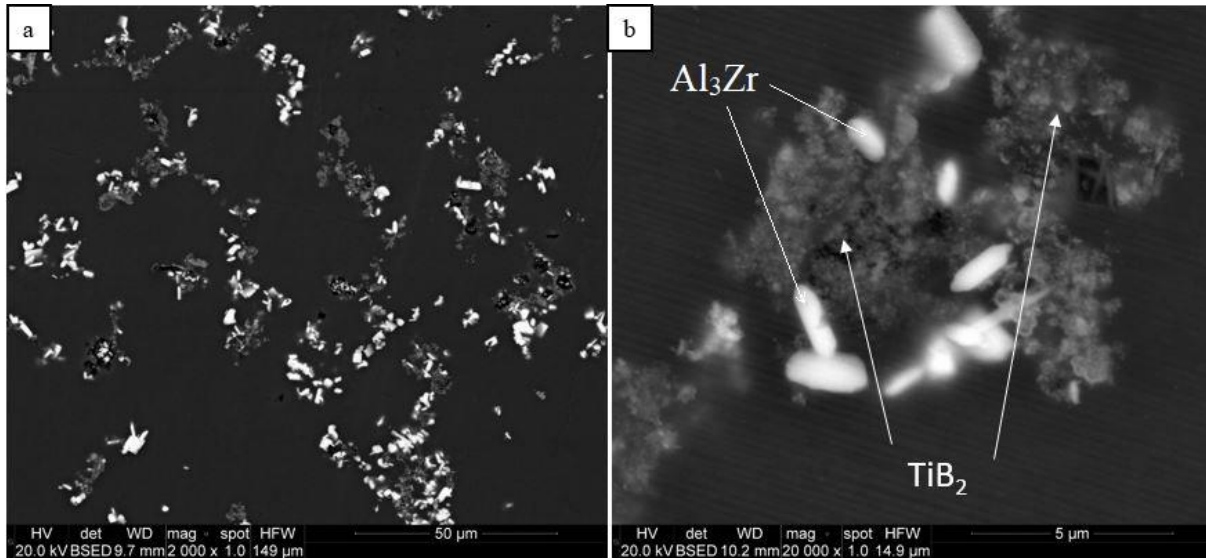


Figure 4.24 SEM Images of O-5 Sample

According to the results of the EDS analysis shown in Figure 4.24, the agglomerated particles and the long rod-shaped particles were TiB_2 and Al_3Zr , respectively. The average length of the Al_3Zr particles was found to be 2.3 μm by quantitative analysis using ImageJ.

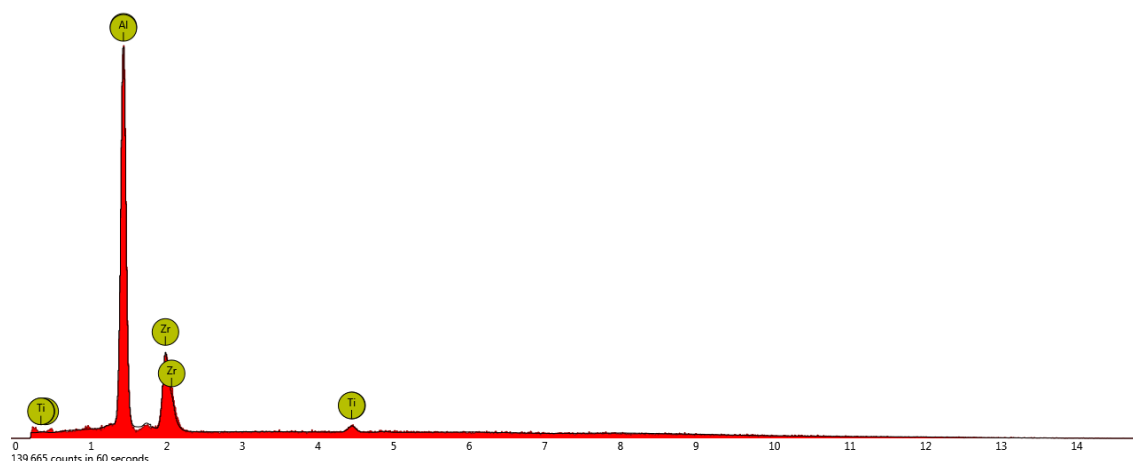


Figure 4.25 EDS Patterns of the Reinforcements in Original Sample

Most of the TiB_2 particles were smaller than $1\ \mu\text{m}$ (Figure 4.16b). The EDS examination indicated that the main phase of the rod-like reinforcement was Al_3Zr which illustrated in Figure 4.25.

4.4.3 Forging Treatment Analysis

The graphs a, b, c, and d in Figure 4.26 correspond to the four samples of O-5, F40-5, F60-5, and F80-5, respectively. First, Figure 4.20a corresponds to the sample without forging treatment. It can be clearly observed that the grains in the Al matrix are relatively intact, the boundaries are continuous, and a large number of reinforcing particles are deposited at the grain boundaries. The sample in Figure 4.26b is forged by a 40% deformation. Compared with the a-graph, there is no obvious difference in the microstructure of the composite. Most of the grains remain intact, but some are slightly deformed. The composite sample in Figure 4.26c has been forged by 60% deformation. The metallographic diagram shows that there are areas where the grain boundary of the grain is broken by forging treatment. Although the material structure shows some deformation, it remains isotropic. The structure of the sample in Figure 4.26d is significantly deformed. Under the large (80%) deformation, the grains are not intact, and most of the grains are crushed.

The microstructure of the composite determines the mechanical properties. As the percentage of forging deformation increases, the grains in the composite are gradually destroyed. Due to the boundary fracture, the nanoparticles that have been agglomerated are dispersed and squeezed.

This helps to improve the mechanical properties of the composite as well as its ductility and toughness.

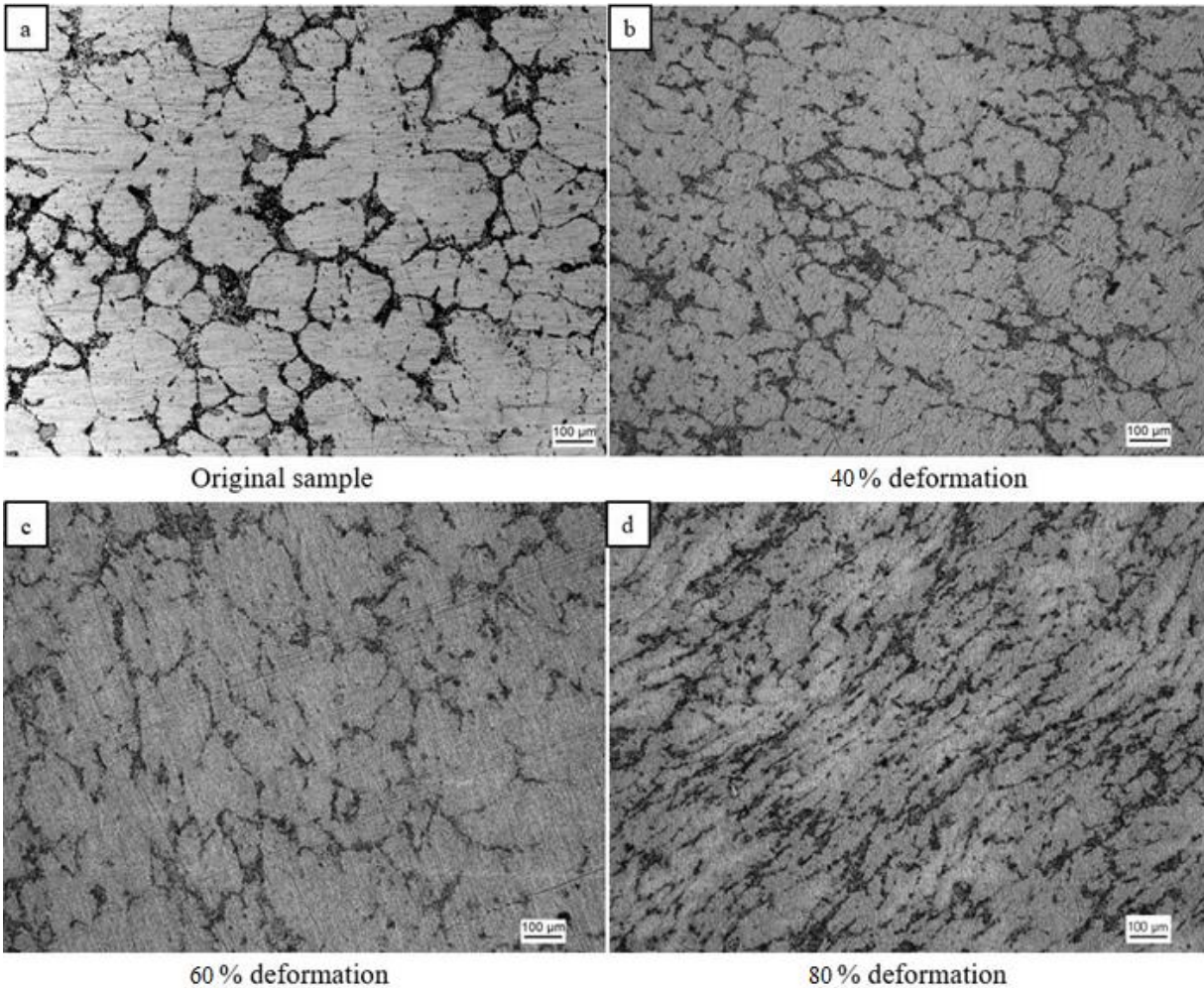


Figure 4.26 Metallographic Microstructure of Nano-5%.wt TiB₂/Al Composites after Various Forging Treatments.

4.4.4 Hardness Test

After the samples were polished and mounted, each positions on each sample was randomly selected to test the Vickers hardness. The test results are listed in Table 4.11. First, the average hardness of all the samples was much higher than that of pure Al, indicating that the TiB₂-reinforcing particles significantly improved the hardness of the Al matrix. Second, with the gradual increase of the TiB₂ volume fraction, the hardness of the composites showed an upward trend.

Table 4.11 Average Vickers Hardness of TiB₂/Al composites prepared in varies parameters.

Volume fraction of nano-TiB ₂	Forging treatment			
	No Forging	40% deformation	60% deformation	80% deformation
1%	35.2	34.8	36.1	37
3%	37.5	35.1	36.2	38.2
5%	38.2	37.1	35.4	39.2

The 5% TiB₂/Al composite had the highest Vickers hardness, which benefited from the TiB₂ particles being uniformly distributed inside the matrix. The doped particles simultaneously played the role of grain refiner. As the volume fraction of the nano-TiB₂ particles increased, the crystal structure of the composite material became denser and the hardness increased. Finally, the introduction of continuous forging treatment technology significantly changed the hardness of the materials. Regardless of the TiB₂ content of the composite material, its hardness changed with the change of forging treatment deformation. The hardness of the composite material decreased during the process from no forging to 40% deformation. Combined with the metallographic analysis described above, the internal cell of the material was gradually destroyed due to deformation, resulting in decreased hardness. When the deformation variable reached 80%, obvious plastic deformation occurred in the matrix of the composite material, and the material structure became denser in a specific direction, which is the reason that composite material hardness increased at 60% deformation.

4.4.5 Tensile Strength Test

After the sample was cut, eight tensile strength test specimens were taken for each set of parameters, and the experimental results. The average tensile strength values of the eight specimens, are shown in Table 4.12.

Table 4.12 Average Tensile strength of TiB₂/Al Composites

Volume fraction of nano-TiB ₂	Forging treatment			
	No Forging	40% deformation	60% deformation	80% deformation
1%	96.02 MPa	97.09 MPa	91.44 MPa	98.10 MPa
3%	96.11 MPa	97.01 MPa	95.09 MPa	99.23MPa
5%	98.10 MPa	100.12 MPa	96.05 MPa	102.23MPa

It can be seen from the experimental results that the tensile strength of the nano-TiB₂ particle-reinforced Al-MMC with no forging and a volume fraction of 1% was 96.02 MPa, and the highest was 102.23 MPa under different preparation parameters.

The maximum tensile strength of the three sets of samples with 1%, 3%, and 5% volume fractions of nano-TiB₂ appeared at 80% deformation by forging treatment, while the lowest value occurred when the deformation was 60%. It can be seen from the microstructure diagram above that the grain boundary damage inside the composite was the most serious at 60% deformation, which was the main reason for decreased tensile strength of the composite. As the amount of forging deformation increased to 80%, the tensile strength of the sample increased. According to the metallographic microstructure, 80% deformation caused obvious structural deformation inside the composite, which made some of the nanoparticles disperse, and the dispersion was more uniform. On the other hand, the grain boundary did not undergo large-scale fracture under 80% deformation, but did become more compacted by extrusion. This structural feature also improved the tensile strength.

4.4.6 Elongation test

Five elongation test specimens were taken for each set of parameters. And the experimental results, the average elongation values of the five coupons, are listed in Table 4.13.

It can be seen from the results that the elongation of the nano-TiB₂ particle-reinforced Al-MMC with no forging and a volume fraction of 1% was 5.55%, and the highest was 25.88% under different preparation parameters.

Table 4.13 Average elongation of TiB₂/Al composites prepared using various parameters

Volume fraction of nano-TiB ₂	Elongation % (stretching/original length)			
	No Forging	40% deformation	60% deformation	80% deformation
1%	5.55	12.44	17.85	21.52
3%	7.79	13.12	19.10	23.31
5%	8.03	15.31	19.85	25.88

The plastic deformation caused by external force has a significant effect on the elongation of the sample. This is mainly due to the fact that the forging treatment break up oxides and clusters of

nano-particles to a certain extent, and By using various amount of plastic deformation during the forging process, the distribution of the nano-particles in the matrix can be further improved, resulting in an increase in the mechanical properties of the material.

CHAPTER 5. SUMMARY, CONCLUSIONS, AND RECOMMENDATIONS

5.1 Main Conclusions

Optimizing the microstructure of particle-reinforced Al-MMCs is the key to improving the mechanical properties of composite materials. In this research, the theoretical verification experiment and the process optimization experiment were designed to study the behavior of the reinforcing particles in aluminum matrix composites.

1. Firstly, $\text{TiB}_2/\text{Al-4.5wt.\%Cu}$ composites were successfully prepared by in-situ MSR. Samples of different solidification speeds were obtained using wedge-shaped grinding tools. According to the prediction model based on surface free energy developed by Uhlmann et al. (1964), the critical velocities of various sizes of TiB_2 - and Al_3Ti -reinforced particles during solidification were calculated under different cooling rates. In Uhlmann's model, when the local growth rate is greater than the critical velocity, the particles should be engulfed by the advancing solid-liquid interface. The results of the verification experiment suggested that, apart from a small number of particles that served as nuclei for the dendrites, most of the Al_3Ti and TiB_2 particles were rejected by the freezing front and accumulated in the area of the grain boundary.

The experimental results suggested that the fastest growth rate of the coupons in the experiment was $0.243 \mu\text{m/s}$, which exceeded the critical growth rate of those particles with diameters equal to or greater than $10 \mu\text{m}$. The observation results were inconsistent with the model prediction results, indicating that the classic prediction model based on surface free energy has limitations.

Classic models for particle pushing usually considers force balance on a particle adjacent to the growing solid-liquid interface. However, solidification is complex process. For small reinforcing particles, especially nanoparticles, the fluid flow in the melt has a great influence on the behavior of these particles. Yet most forecasting models did not take the fluid flow into consideration.

For molten metal, the process phase transition from liquid to solid is accompanied by volumetric shrinkage. The author believes that the liquid will be drawn into the gap between the solid and the particle, while the solute will diffuse against the physical fluid flow at the certain rate which is sufficient to prevent the accumulation of solute between the particles and solids.

By substituting diffusion and mass flow into the diffusion convection equation, the authors established a balance model between diffusion based on concentration gradients and fluid flow raise from volume shrinkage as follow:

$$R \leq \frac{\rho_L D_L k_0 G_S}{(\rho_L - \rho_S) \sqrt{2} a d^2 \pi m_L C_0}, \text{ when } \theta \rightarrow 0;$$

and

$$R \leq \frac{2 \rho_L D_L k_0 G_S}{(\rho_L - \rho_S) a \pi^2 d^2 C_0}, \text{ when } \theta = \frac{\pi}{2}.$$

These two equations correspond to two extreme steady-state conditions between the particle and the solid-liquid interface. The critical velocity of particle pushing based on the diffusion-convection model taking into account the fluid flow is calculated. The results indicate that the particle diameter is inversely proportional to the critical velocity, and the actual critical velocity is several orders of magnitude lower than the critical velocity calculated by the classical prediction model. The TiB₂ and Al₃Ti particles satisfying the nucleation conditions with diameters ranges from 0.5μm to 15μm should be engulfed by moving freezing front during the redistribution process. However, observations confirmed that all particles were pushed by the interface. This actually proves that the classic particle pushing thermodynamic criterion based on surface free energy equilibrium cannot effectively predict the behavior of particles during solidification.

The relationship between the temperature gradients and critical velocity has been investigated. Based on diffusion-convection model, the results indicated that the critical velocity is linearly proportional to the temperature gradient. As the particle diameter size decreases, the critical speed gradually increases.

2. Optimization of Preparation Parameters of TiB_2/Al composites. The preparations of nano- TiB_2/Al with ultrasound and high energy ball milling assistance were studied. The experimental results clearly showed that the experimental parameters, such as the volume fraction of the reinforcement particles and the percentage of forging deformation, influence the synthesis of TiB_2/Al composites. The use of high energy ball milling promotes the mixing of nano-sized particles with the salt particles by a layer of salt coating on the clusters of the nano-particles. The coated salt then is melted when the mixture is added into the molten aluminum. The melted salt reacts with oxides to clean the surfaces of nano particles, making these particles easy in adding into the melt. The use of high intensity ultrasonic vibration in molten aluminum breaks the clusters of nanoparticles and disperses these particles more uniformly in the molten metal.

3. A new post-treatment method, forging process, was introduced in the processing of Ti_2B particulate reinforced aluminum matrix composites. Plastic deformation caused in the samples during the forging process tends to break up oxides and clusters of nano-particles further. By using various amount of plastic deformation during the forging process, the distribution of nanoparticles can be further improved, and the resultant mechanical properties, especially ductility, are enhanced. This opens up new opportunities for the preparation of nano-particle reinforced Al-based composites.

5.2 Outlook

This paper re-evaluates the classic particle pushing models based on surface free energy considerations, points out the limitations in the classic model, and establishes a new equilibrium model based on fluid flow and diffusion on particle pushing by a growing solid-liquid interface. It should be noted that the solidification process is complicated. During the practical solidification process, the growth rate of the crystals is dynamic, and the fluid flow between the particles and the interface is also unstable. Besides, flow in the liquid phase is hard to describe with analytical models. Often 3D numerical simulation is required to describe fluid flow during solidification. In the study, the diffusion convection model can only describe the relationship between the variables in the equilibrium state when the particles are pushed out by a freezing front under ideal conditions. There is still much room for improvement in practical applications.

In addition, this paper proposes that because of the existence of fluid flow during solidification, the reinforcing particles must be pushed to the grain boundaries by the growing solid-liquid interface, leading to particle segregation there. This is especially true for nano-sized particles such as TiB_2 , the segregation phenomenon cannot be avoided during the solidification process because of particle pushing. Therefore, in order to improve the mechanical properties of composite materials, a secondary processing technology, such as forging process, can be used as to improve the microstructure and the resultant mechanical properties. This is an important research direction for improving the performance of nanoparticle-reinforced metal matrix composites. In the future, it would be beneficial to introduce a post-processing device with a controllable larger deformation amount, and try to further destroy the agglomerated nanoparticles by external force while maintaining the material integrity. This has great research prospects.

REFERENCES

- Akbari, M. K., Baharvandi, H. R., & Shirvanimoghaddam, K. (2015). Tensile and fracture behavior of nano/micro TiB₂ particle reinforced casting A356 aluminum alloy composites. *Materials & Design* (1980-2015), 66, 150-161.
- Abbasipour, B., Niroumand, B., & Vaghefi, S. M. (2010). Compocasting of A356-CNT composite. *Transactions of Nonferrous Metals Society of China*, 20(9), 1561-1566.
- Aghajanian, M. K., Macmillan, N. H., Kennedy, C. R., Luszcz, S. J., & Roy, R. (1989). Properties and microstructures of Lanxide® Al₂O₃-Al ceramic composite materials. *Journal of materials Science*, 24(2), 658-670.
- Anandkumar, R., Almeida, A., & Vilar, R. (2011). Wear behavior of Al-12Si/TiB₂ coatings produced by laser cladding. *Surface and Coatings Technology*, 205(13-14), 3824-3832.
- Banerji, A., Rohatgi, P. K., & Reif, W. (1984). Role of wettability in the preparation of metal-matrix composites. a review). *Metall Tech*, 38, 656-661.
- Christy, T. V., Murugan, N., & Kumar, S. (2010). A comparative study on the microstructures and mechanical properties of Al 6061 alloy and the MMC Al 6061/TiB₂/12p. *Journal of Minerals and Materials Characterization and Engineering*, 9(01), 57.
- Chapelon, J. Y., Cathignol, D., Gelet, A., & Blanc, E. (1997). U.S. Patent No. 5,601,526. Washington, DC: U.S. Patent and Trademark Office.
- Chernov, N. I., Eyink, G. L., Lebowitz, J. L., & Sinai, Y. G. (1993). Derivation of Ohm's law in a deterministic mechanical model. *Physical review letters*, 70(15), 2209.
- Casati, R., & Vedani, M. (2014). Metal matrix composites reinforced by nano-particles—a review. *Metals*, 4(1), 65-83.
- Cui, C., Shen, Y., Meng, F., & Kang, S. (2000). Review on fabrication methods of in situ metal matrix composites. *Cailiao Kexue Yu Jishu*(Journal of Materials Science & Technology)(China)(USA), 16, 619-626.
- Eskin, G. I. (1995). Cavitation mechanism of ultrasonic melt degassing. *Ultrasonics Sonochemistry*, 2(2), S137-S141.
- Eskin, G. I. (1998). *Ultrasonic treatment of light alloy melts*. CRC Press.
- Eskandari, H., Taheri, R., & Khodabakhshi, F. (2016). Friction-stir processing of an AA8026-TiB₂-Al₂O₃ hybrid nanocomposite: Microstructural developments and mechanical properties. *Materials Science and Engineering: A*, 660, 84-96.

- El-Mahallawy, MA Taha, AEW Jarfors, H.Fredriksson, On the reaction between aluminium, K_2TiF_6 and KBF_4 , *J.Alloys and Compounds*, 292 (1999) 221–229.
- Feng, C. F., & Froyen, L. (2000). Microstructures of in situ Al/TiB₂ MMCs prepared by a casting route. *Journal of materials science*, 35(4), 837-850.
- Flemings, M. C. (2006). Solidification processing. *Materials Science and Technology*.
- Guo, Q., Ghadiri, R., Weigel, T., Aumann, A., Gurevich, E. L., Esen, C., ... & Ostendorf, A. (2014). Comparison of in situ and ex situ methods for synthesis of two-photon polymerization polymer nanocomposites. *Polymers*, 6(7), 2037-2050.
- Gao, Q., Wu, S., Lü, S., Xiong, X., Du, R., & An, P. (2017). Effects of ultrasonic vibration treatment on particles distribution of TiB₂ particles reinforced aluminum composites. *Materials Science and Engineering: A*, 680, 437-443.
- Gopalakrishnan, S., & Murugan, N. (2012). Production and wear characterisation of AA 6061 matrix titanium carbide particulate reinforced composite by enhanced stir casting method. *Composites Part B: Engineering*, 43(2), 302-308.
- He, F., Han, Q., & Jackson, M. J. (2008). Nanoparticulate reinforced metal matrix nanocomposites—a review. *International Journal of Nanoparticles*, 1(4), 301-309.
- Han, Q., & Hunt, J. D. (1995). Particle pushing: critical flow rate required to put particles into motion. *Journal of crystal growth*, 152(3), 221-227.
- Hanada, K., Khor, K. A., Tan, M. J., Murakoshi, Y., Negishi, H., & Sano, T. (1997). Aluminium-lithium/SiCp composites produced by mechanically milled powders. *Journal of Materials Processing Technology*, 67(1-3), 8-12.
- Huashun, Y., Hongmei, C., Liming, S., & Guanghui, M. (2006). Preparation of Al-Al₃Ti in-situ composites by direct reaction method. *Rare Metals*, 25(1), 32-36.
- Hemanth, J. (2009). Development and property evaluation of aluminum alloy reinforced with nano-ZrO₂ metal matrix composites (NMMCs). *Materials Science and Engineering: A*, 507(1-2), 110-113.
- Horvitz, D., & Gotman, I. (2002). Pressure-assisted SHS synthesis of MgAl₂O₄-TiAl in situ composites with interpenetrating networks. *Acta materialia*, 50(8), 1961-1971.
- Hu, Q., Luo, P., & Yan, Y. (2007). Influence of an electric field on combustion synthesis process and microstructures of TiC-Al₂O₃-Al composites. *Journal of alloys and compounds*, 439(1-2), 132-136.
- Ibrahim, I. A., Mohamed, F. A., & Lavernia, E. J. (1991). Particulate reinforced metal matrix composites—a review. *Journal of materials science*, 26(5), 1137-1156.
- J.V. Wood, P. Davis, and J.L.F. Kellie: *Mater. Sci. Technol.*, 1993, vol. 9, pp. 833-37.

- Kumar, S., Chakraborty, M., Sarma, V. S., & Murty, B. S. (2008). Tensile and wear behavior of in-situ Al-7Si/TiB₂ particulate composites. *Wear*, 265(1-2), 134-142.
- Koczak, M. J., & Premkumar, M. K. (1993). Emerging technologies for the in-situ production of MMCs. *Jom*, 45(1), 44-48.
- Kang, Y. C., & Chan, S. L. I. (2004). Tensile properties of nanometric Al₂O₃ particulate-reinforced aluminum matrix composites. *Materials chemistry and physics*, 85(2-3), 438-443.
- Li, J. W., Momono, T., Ying, F. U., Zheng, J. I. A., & Tayu, Y. (2007). Effect of ultrasonic stirring on temperature distribution and grain refinement in Al-1.65% Si alloy melt. *Transactions of Nonferrous Metals Society of China*, 17(4), 691-697.
- Li, J. W., & Pu, Y. (2015). Application of ultrasonic treating to degassing of commercially pure copper melt: A preliminary investigation. *Materials Letters*, 161, 60-63.
- Lee, C. T., & Chen, S. W. (2002). Quantities of grains of aluminum and those of TiB₂ and Al₃Ti particles added in the grain-refining processes. *Materials Science and Engineering: A*, 325(1-2), 242-248.
- Lei, Y. C., Zhang, Z., Nie, J. J., & Chen, X. Z. (2008). Effect of Ti-Al on microstructures and mechanical properties of plasma arc in-situ welded joint of SiCp/Al MMCs. *Transactions of Nonferrous Metals Society of China*, 18(4), 809-813.
- Lanping, H. H. C. K. H., & Qiang, L. H. Z. (2004). Effects of Ultrasonic Treatment for Al Melt on the Properties and Microstructure of Al Alloy [J]. *Special Casting & Nonferrous Alloys*, 4, 005.
- Liang, Y. F., Zhou, J. E., & Dong, S. Q. (2010). Microstructure and tensile properties of in situ TiCp/Al-4.5 wt.% Cu composites obtained by direct reaction synthesis. *Materials Science and Engineering: A*, 527(29-30), 7955-7960.
- Liu, Z., Han, Q., & Li, J. (2012). A developed method for producing in situ TiC/Al composites by using quick preheating treatment and ultrasonic vibration. *Composites Part B: Engineering*, 43(5), 2429-2433.
- Liu, G., Li, J., & Chen, K. (2013). Combustion synthesis of refractory and hard materials: a review. *International Journal of Refractory Metals and Hard Materials*, 39, 90-102.
- Lakshmi, S., Lu, L., & Gupta, M. (1998). In-situ preparation of TiB₂ reinforced Al based composites. *Journal of materials processing technology*, 73(1-3), 160-166.
- Ma, T., Yamaura, H., Koss, D. A., & Voigt, R. C. (2003). Dry sliding wear behavior of cast SiC-reinforced Al MMCs. *Materials Science and Engineering: A*, 360(1-2), 116-125.

- Moldovan, P., Butu, M., Popescu, G., Buzatu, M., Usurelu, E., Soare, V., & Mitrica, D. (2010). Thermodynamics of interactions in Al-K₂TiF₆-KBF₄ system. *Revista de Chimie*, 61(9), 828-832.
- Merzhanov, A. G. (1995). History and recent developments in SHS. *Ceramics international*, 21(5), 371-379.
- Merzhanov, A. G. (1990). Self-propagating high-temperature synthesis: twenty years of search and findings. *Combustion and plasma synthesis of high-temperature materials*, 1-53.
- Mahallawy, N., Taha, M. A., Jarfors, A. E., & Fredriksson, H. (1999). On the reaction between aluminium, K₂TiF₆ and KBF₄. *Journal of alloys and compounds*, 292(1-2), 221-229.
- Mishra, S. K., Das, S. K., & Sherbacov, V. (2007). Fabrication of Al₂O₃-ZrB₂ in situ composite by SHS dynamic compaction: a novel approach. *Composites Science and Technology*, 67(11-12), 2447-2453.
- Nabawy, A. M., & Chen, X. G. (2015). Fabrication of Al-TiB₂ nanocomposites by flux-assisted melt stirring. *Metallurgical and Materials Transactions B*, 46(4), 1596-1602.
- Noltingk, B. E., & Neppiras, E. A. (1950). Cavitation produced by ultrasonics. *Proceedings of the Physical Society. Section B*, 63(9), 674.
- Narimani, M., Lotfi, B., & Sadeghian, Z. (2016). Investigating the microstructure and mechanical properties of Al-TiB₂ composite fabricated by Friction Stir Processing (FSP). *Materials Science and Engineering: A*, 673, 436-442.
- Neppiras, E. A. (1984). Acoustic cavitation series: part one: Acoustic cavitation: an introduction. *Ultrasonics*, 22(1), 25-28.
- Omenyi, S. N., & Neumann, A. W. (1976). Thermodynamic aspects of particle engulfment by solidifying melts. *Journal of Applied Physics*, 47(9), 3956-3962.
- Popoola, A. P., Pityana, S., & Ogunmuyiwa, E. (2011). Microstructure and wear behaviour of Al/TiB₂ metal matrix composite. In *Advanced Materials Research* (Vol. 227, pp. 23-26). Trans Tech Publications.
- Ramirez, A., Qian, M., Davis, B., Wilks, T., & StJohn, D. H. (2008). Potency of high-intensity ultrasonic treatment for grain refinement of magnesium alloys. *Scripta Materialia*, 59(1), 19-22.
- Reddy, B. S. B., Das, K., & Das, S. (2007). A review on the synthesis of in situ aluminum based composites by thermal, mechanical and mechanical-thermal activation of chemical reactions. *Journal of Materials Science*, 42(22), 9366-9378.
- Shah, S. A. A. (2016). Micro-mechanics modelling of smart materials (Doctoral dissertation, Sheffield Hallam University (United Kingdom)).

- Suryanarayana, C. (2001). Mechanical alloying and milling. *Progress in materials science*, 46(1-2), 1-184.
- Shangguan, D., Ahuja, S., & Stefanescu, D. M. (1992). An analytical model for the interaction between an insoluble particle and an advancing solid/liquid interface. *Metallurgical Transactions A*, 23(2), 669-680.
- Stefanescu, D. M., Dhindaw, B. K., Kacar, S. A., & Moitra, A. (1988). Behavior of ceramic particles at the solid-liquid metal interface in metal matrix composites. *Metallurgical Transactions A*, 19(11), 2847-2855.
- Sasikumar, R., Ramamohan, T. R., & Pai, B. C. (1989). Critical velocities for particle pushing by moving solidification fronts. *Acta Metallurgica*, 37(7), 2085-2091.
- Suresh, S., Moorthi, N. S. V., Vettivel, S. C., & Selvakumar, N. (2014). Mechanical behavior and wear prediction of stir cast Al–TiB₂ composites using response surface methodology. *Materials & Design*, 59, 383-396.
- Spoor, P. S., Maynard, J. D., Pan, M. J., Green, D. J., Hellmann, J. R., & Tanaka, T. (1997). Elastic constants and crystal anisotropy of titanium diboride. *Applied physics letters*, 70(15), 1959-1961.
- Tjong, S. C., & Ma, Z. Y. (2000). Microstructural and mechanical characteristics of in situ metal matrix composites. *Materials Science and Engineering: R: Reports*, 29(3-4), 49-113.
- Tjong, S. C., & Wang, G. (2004). Synthesis and Low Cycle Fatigue Behavior of In-situ Al-based Composite Reinforced with Submicron TiB₂ and TiC Particulates. *Advanced Engineering Materials*, 6(12), 964-968.
- Tjong, S. C., Tam, K. F., & Wu, S. Q. (2003). Thermal cycling characteristics of in-situ Al-based composites prepared by reactive hot pressing. *Composites science and technology*, 63(1), 89-97.
- Tee, K. L., Lu, L., & Lai, M. O. (1999). Synthesis of in situ Al–TiB₂ composites using stir cast route. *Composite Structures*, 47(1-4), 589-593.
- Uhlmann, D. R., Chalmers, B., & Jackson, K. A. (1964). Interaction between particles and a solid-liquid interface. *Journal of Applied Physics*, 35(10), 2986-2993.
- Wang, J., Li, P., Chen, C., & Xue, J. (2012). An In-Situ Technique for Preparing Al–TiB₂ and Al–Al₃Ti Composites. In *Light Metals 2012* (pp. 285-289). Springer, Cham.
- Wang, M., & Han, Q. Y. (2014). Particle pushing during solidification of metals and alloys. In *Materials Science Forum* (Vol. 783, pp. 1513-1517). Trans Tech Publications.
- Wang, H. Y., Jiang, Q. C., Wang, Y., Ma, B. X., & Zhao, F. (2004). Fabrication of TiB₂ particulate reinforced magnesium matrix composites by powder metallurgy. *Materials letters*, 58(27-28), 3509-3513.

- Wan, H., Pan, J., & Yang, D. (1995). In-Situ Aluminum Matrix Composite Prepared by Ultrasonic Vibration. Proceedings of ICCM-10, Whistler, BC Canada, 161-167.
- Xu, H., Meek, T. T., & Han, Q. (2007). Effects of ultrasonic field and vacuum on degassing of molten aluminum alloy. *Materials Letters*, 61(4-5), 1246-1250.
- Xu, H., Jian, X., Meek, T. T., & Han, Q. (2004). Degassing of molten aluminum A356 alloy using ultrasonic vibration. *Materials letters*, 58(29), 3669-3673.
- Yu, P., Mei, Z., & Tjong, S. C. (2005). Structure, thermal and mechanical properties of in-situ Al-based metal matrix composite reinforced with Al_2O_3 and TiC submicron particles. *Materials Chemistry and Physics*, 93(1), 109-116.
- Yeh, C. L., & Wang, H. J. (2009). Effects of sample stoichiometry of thermite-based SHS reactions on formation of Nb–Al intermetallics. *Journal of Alloys and Compounds*, 485(1-2), 280-284.
- Yang, Y., Lan, J., & Li, X. (2004). Study on bulk aluminum matrix nano-composite fabricated by ultrasonic dispersion of nano-sized SiC particles in molten aluminum alloy. *Materials Science and Engineering: A*, 380(1-2), 378-383.
- Youssef, Y. M., Dashwood, R. J., & Lee, P. D. (2005). Effect of clustering on particle pushing and solidification behaviour in TiB₂ reinforced aluminium PMMCs. *Composites Part A: Applied Science and Manufacturing*, 36(6), 747-763.
- Yi, X. S., Du, S., & Zhang, L. *Composite Materials Engineering*, Volume 2.
- Zhao, Y. T., Cheng, X. N., Dai, Q. X., Cai, L., & Sun, G. X. (2003). Crystal morphology and growth mechanism of reinforcements synthesized by direct melt reaction in the system Al–Zr–O. *Materials Science and Engineering: A*, 360(1-2), 315-318.
- Zhang, L., & Wang, Z. (2008). Thermal investigation of fabricating porous NiTi SMA by SHS. *Experimental Thermal and Fluid Science*, 32(6), 1255-1263.
- Zhang, D. L. (2004). Processing of advanced materials using high-energy mechanical milling. *Progress in Materials Science*, 49(3-4), 537-560.